



ScuDo
Scuola di Dottorato - Doctoral School
WHAT YOU ARE, TAKES YOU FAR



Doctoral Dissertation

Doctoral Program in Energy Engineering (32th cycle)

Design of innovative solutions for high-pressure fuel injection systems, optimization of measuring techniques for injected flow-rate and modeling of 1D flows

By

Tantan Zhang

Supervisors:

Prof. Alessandro Ferrari

Doctoral Examination Committee:

Prof. Zhijun Wu, Referee, Tongji University

Prof. Gianmarco Bianchi, Referee, Università di Bologna

Prof. Lucio Postriotti, Referee, Università degli Studi di Perugia

Prof. Antonio Garcia Martinez, Referee, Università di Valencia

Prof. Michele Manno, Referee, Università degli Studi di Roma "Tor Vergata"

Politecnico di Torino

2020

Declaration

I hereby declare that, the contents and organization of this dissertation constitute my own original work and does not compromise in any way the rights of third parties, including those relating to the security of personal data.

Tantan Zhang
2020

* This dissertation is presented in partial fulfillment of the requirements for **Ph.D. degree** in the Graduate School of Politecnico di Torino (ScuDo).

Abstract

In order to mitigate the engine emissions as well as the manufacture costs, the common rail injection system, which is generally fed with diesel, have been diffused and applied to all types of road cars. Over the years, more and more injection shots over one engine cycle and types of irregular injection rates have been realized by means of such a device. Meanwhile, some complex designs of layouts and of control strategies have been developed to achieve certain specific functions. Whereas, further improvements in this system, in the related flowmeters as well as in the mathematical models can be still applicable.

The current study is focused on the experimental and mathematical analyses of the injection rate flowmeters and of the injection systems. Structural optimizations have been applied to both instruments, and an innovative control strategy for the injection system has been developed and experimentally investigated. Finally, the polytropic process has been adopted to analytically and numerically interpret the classic viscous adiabatic flow analytical model in a constant cross section duct.

The injection rate of a common rail injector has been evaluated by means of both Bosch and Zeuch method-based flowmeters. A slight decline of the slope in the rate rising phase, an anomalous tail at the end of an injection event and a delay in the entire injected flow-rate trace have been found in the result obtained through Bosch method. A 1D numerical model of the hydraulic circuit, pertaining to the flowmeter that applies Bosch method, has been developed. The cause and effect relationship between the design and the measured flow-rate has been then investigated, and the design keys of the Bosch method-based flowmeters have been provided.

With respect to the injection system layout, in order to simplify the installation and to reduce the production cost, the Common-Feeding (CF) system has been designed and has been manufactured for a light-duty commercial vehicle diesel engine. In the CF instrument, a delivery chamber of approximately

10 cm³ is integrated at the outlet of the high-pressure pump, and the other side is connected to the injectors with the tubes. The experimental tests in terms of single and double injections have been performed at the hydraulic rig to compare the performance of the prototypal CF instrument with that of the standard common rail system equipped with different rail volumes. The testing results prove that the general performance of the CR systems, even though the rails feature different volumes, and that of the CF system are analogous. The primary difference, which is a change of the slope, occurs at the rising phase of the injection rate. Moreover, the cycle-to-cycle dispersion of the injected mass ascends to certain degree, as the accumulator (the rail or the delivery chamber at the pump outlet) size reduces. In addition, the variation in the free wave frequency after the injection event can be ascribed to the modification of the accumulator shape.

As far as the rate-shaping strategies are concerned, an injection system equipped with solenoid injectors have been experimentally tested. The cycle-to-cycle dispersion in the injected mass evidently rises in the regime of closely-coupled injections. Meanwhile, the overall injected mass increases sharply as the dwell time reduces. Whereas, when the dwell time is further reduced within the injection fusion range, the cycle-to-cycle dispersion again improves, and such a phenomenon confirms that it is applicable to apply the continuous rate-shaping strategy to solenoid injectors. A 1D numerical model of the hydraulic circuit of the injection system with solenoid injectors has been developed and validated. The parametric analyses on the injector setups, such as the mechanical, the electromagnetic and the hydraulic parameters, have been carried out to examine their influences on the rate-shaping injection patterns. In addition, two state-of-the-art solenoid injectors, featuring different hydraulic layouts, have been tested and compared in terms of closely-coupled injections, and the results provided by the numerical model have been verified.

Besides, an innovative closed-loop control strategy of injected mass has been developed. The pressure time histories measured at the rail-to-injector tube have been captured to calculate the instantaneous mass flow-rate entering the injector through two different methods. The first method uses the mean instantaneous frequency of the pressure trace to obtain the key time instants of injector dynamics. The hydraulic performance data experimentally acquired have been then employed to correlate those timings with the injected mass.

The second method directly applies the physical laws of fluid dynamics. The derived flow-rate has been afterwards integrated, and has been correlated well with the injected mass. A prototypal hardware, based on the second calculation method, has been realized in order to control the injected mass in a closed-loop. Such a system is capable to significantly improve the accuracy of the injected mass within different thermal regimes. In addition, under steady states, as a mean injected mass of 45 mg per engine cycle is applied, the error of the effective injected mass was below 1 mg for single injections and is within 2 mg for pilot-main injections. The dynamic response to the transients of either a step or a ramp in the rail pressure and in the injected mass was as well improved significantly.

Finally, as regards the viscous adiabatic flow model, by eliminating the steady flow energy equation and by following a polytropic process, the compressible flow in constant-area ducts with friction has been analytically expressed. Under the identical boundary conditions, the comparison between flow properties pertaining to the new method and those of the classic analysis have been as well performed. The results show that following the polytropic method, although flow properties are capable to lead to the analogous values at both the extremities of the pipe as the classic method results for not choked cases, they follow different routes. In addition, in order to improve the accuracy of the computed flow properties obtained through the polytropic method, a practical numerical method has been introduced. The polytropic exponents obtained piece by piece along the duct following the classic analysis has been thus applied to the corresponding nodes of the code, and the final numerical results by following the polytropic method are approximately identical to those of the classic method.

Keywords: common rail, flowmeter, Bosch method, Zeuch method, Common-Feeding, injector setup, rate-shaping, closed-loop, Fanno flow, polytropic.

Acknowledgements

This thesis was carried out at DENERG of Politecnico di Torino, in Turin, from 2016 to 2020.

I wish to express my sincere appreciation to my advisor, Prof. Ferrari Alessandro, for all his talented guidance. Without his persistent help, the goal of those projects would not have been realized.

I want to express my gratitude to my PhD colleagues, Vento Oscar and Jin Zhiru, who have always given me a hand to perform the experimental tests, and have provided me ideas to optimize the solutions.

I would like to acknowledge the support and great love of my wife, Zeng Manyu. She kept me going on and this work would not have been possible without her supports.

Contents

List of Figures	ix
List of Tables	xiv
Nomenclature	xv
1 Introduction	1
1.1 Fuel injection rate flowmeters	2
1.2 Optimization of injection systems	3
1.3 Closed-loop control strategy	5
1.4 Compressible flow in constant area ducts	8
1.5 Contributions and outline	9
2 Benchmark of the flowmeters	12
2.1 Experimental setup	12
2.2 Zeuch and Bosch methods	14
2.3 Numerical model	17
2.3.1 1D pipe-flow model	18
2.3.2 Chamber, restriction and Helmholtz resonator	20
2.3.3 Numerical algorithm	22
2.4 Results and discussion	23
3 Injection system optimization	33
3.1 Experimental setup	33
3.2 Common-Feeding system	35
3.3 Injector setup	47
3.3.1 Closely-coupled multiple injections	47
3.3.2 <i>IFT</i> determination criteria	49

3.3.3	Cycle-to-cycle dispersion analysis	54
3.3.4	Numerical model	57
3.3.5	Methodology applied in the parametric tests	60
3.3.6	Results of the parametric tests	62
3.3.7	Benchmark between injectors with Minirail and without it	69
4	Closed-loop control strategy of injected mass	74
4.1	Experimental setup	74
4.2	TFA based technique	76
4.2.1	Time-frequency analysis	76
4.2.2	Injector characteristics	77
4.2.3	TFA sensor	79
4.2.4	Results	80
4.3	Physical equation based techniques	84
4.3.1	Control strategy and prototypal hardware	84
4.3.2	Results for single injections	88
4.3.3	Results for pilot-main injections	94
5	Fanno flow approximated in polytropic process	97
5.1	Analytical relations for polytropic flows	97
5.2	Comparison between the polytropic and the classic Fanno flows	100
5.3	Numerical model	105
5.4	Numerical model results	108
6	Conclusions	111
	References	115

List of Figures

2.1	EVI schematic.	13
2.2	EVI device internal feature.	13
2.3	HDA schematic.	14
2.4	Pressure wave front in the measuring tube with different reference frames.	16
2.5	Schematic of the EVI hydraulic model.	17
2.6	Experimental and numerical pressure of the EVI instrument.	23
2.7	HDA and EVI experimental mass flow-rates.	24
2.8	The input and the output mass flow-rates and the internal pressure of the chamber C_1 (model results).	25
2.9	pressure upstream and downstream of the damper R_1 (model results).	26
2.10	$p_{do,R1}$ for different installation conditions of the damper R_1 (model results).	26
2.11	p_1 for different C_1 volumes (model results).	27
2.12	p_2 for different C_2 volumes (model results).	27
2.13	Mass flow-rates upstream of chamber C_2 in the presence and in the absence of the convergent pipe (model results).	28
2.14	Time histories of the pressures at different sections of the convergent pipe L_1 (model results).	28
2.15	Estimated EVI injection rate and the mass flow-rate entering the junction C_3 (model results).	29
2.16	Pressure time history in C_3 and C_4 (model results).	29
2.17	Predicted EVI mass flow-rate, mass flow-rate leaving C_3 and mass flow-rate downstream of C_3 (model results).	30

2.18	Pressure waves along the tube loop downstream of the Helmholtz resonator (model results).	30
2.19	Time distribution of G_{EVI} for different C_1 volumes and HDA injection rate ($p_{nom} = 800$ bar, $ET = 1000$ μ s).	31
3.1	KMM flowmeter layout.	34
3.2	The schematic of the high-pressure circuit of the CR and the CF systems.	35
3.3	The high-pressure pump integrated with the accumulator.	36
3.4	Comparison on the G_{inj} and the $p_{inj,in}$ between the CR systems with different rail volumes.	37
3.5	Comparison on the G_{inj} and the $p_{inj,in}$ between the CR and the CF systems.	39
3.6	Comparison on the M_{inj} between the CR ($V_{rail} = 12.9$ cm ³ and 2.1 cm ³) and the CF (without gauged orifices) systems.	40
3.7	Comparison on the $M_{st,leak}$ and the $T_{inj,in}$ between the CR systems with varied V_{rail}	41
3.8	Comparison on the $M_{dyn,leak}$ between the CR systems with varied V_{rail}	42
3.9	Comparison on the σ between the CR systems with different V_{rail}	42
3.10	Definitions of NOD and NCD	43
3.11	NOD of the CR systems with different V_{rail}	43
3.12	NCD of the CR systems with different V_{rail}	44
3.13	Comparison on the G_{inj} and the $p_{inj,in}$ between the CR systems with different V_{rail} for pilot-main injections.	45
3.14	Comparison on the V_{inj} between the CR systems for pilot-main injections ($p_{nom} = 1000$ bar).	45
3.15	Comparison on the V_{inj} fluctuations with DT between the CF systems for pilot-main injections ($p_{nom} = 1000bar$).	46
3.16	Double injections realized by means of solenoid injectors.	48
3.17	Injection flow-rates under different DT s captured by EVI.	50
3.18	Injected masses under different DT s (IFT_1 determination).	51
3.19	Injection flow-rates under different DT s (IFT_2 determination).	52
3.20	The IFT s based on the 2nd criterion.	52
3.21	Injection flow-rates under different DT s (IFT_3 determination).	53
3.22	Analysis of the differences between IFT_1 , IFT_2 and IFT_3	54

3.23	Cycle-to-cycle dispersion in M_{cum} for double injections.	54
3.24	Injected mass depending on DT for double injections.	55
3.25	Cycle-to-cycle dispersion in injection rates.	56
3.26	Schematic of the numerical model of the CR system.	58
3.27	Injected mass flow-rates and injector inlet transients model validation tests under different operating conditions.	59
3.28	Overall injected mass model validation tests under different operating conditions.	60
3.29	M_{cum} as a function of DT ($p_{nom} = 1600$ bar, $M_{main} = 20$ mg), $M_{after} = 2.5$ mg.	61
3.30	Investigated solenoid injector (CRI 2.18 injector).	63
3.31	DT sweeps for different values of d_{cp}	64
3.32	DT sweeps in the main-after injections for different values of d_{ne} ($p_{nom} = 1600$ bar, $M_{main} = 20$ mg, $M_{after} = 2.5$ mg).	65
3.33	DT sweeps for different values of d_A	65
3.34	DT sweeps for different values of d_Z	66
3.35	DT sweeps for different values of L_{gap}	67
3.36	DT sweeps for different values of I_{max}	67
3.37	DT sweeps in the pilot-main injections for different values of α ($p_{nom} = 1000$ bar, $M_{pil} = 2.5$ mg, $M_{main} = 20$ mg).	68
3.38	DT sweeps in the pilot-main injections for different values of V_{dc} ($p_{nom} = 1000$ bar, $M_{pil} = 2.5$ mg, $M_{main} = 20$ mg).	68
3.39	DT sweeps in the pilot-main injections for different values of V_{cc} ($p_{nom} = 1000$ bar, $M_{pil} = 2.5$ mg, $M_{main} = 20$ mg).	68
3.40	CRI 2.18 solenoid injector.	69
3.41	CRI 2.20 solenoid injector.	70
3.42	DT sweeps in the pilot-main injections for the systems of CRI 2.18 and of CRI 2.20.	71
3.43	Cycle-to-cycle dispersions in the pilot-main injections for the systems of CRI 2.18 and of CRI 2.20.	71
4.1	The experimental layout of the injection system for testing TFA based method.	75
4.2	The experimental layout of the injection system for testing physical equation based methods.	75
4.3	Injector characteristics $ET - M_{inj}$ for different p_{nom} and T_{tank}	77

4.4	Influences of the fuel temperature on the injected mass flow-rate.	78
4.5	$ITL - M_{inj}$ for different p_{nom} and T_{tank} .	78
4.6	G_{inj} , p_{inj} and the current pertaining to $p_{nom} = 1200$ bar and $ET = 600 \mu\text{s}$.	79
4.7	G_{inj} , p_{inj} and the normalized MIF ($p_{nom} = 1000$ bar and $ET = 800 \mu\text{s}$).	81
4.8	G_{inj} , p_{inj} and the normalized MIF ($p_{nom} = 1700$ bar and $ET = 450 \mu\text{s}$).	81
4.9	G_{inj} , p_{inj} and the normalized MIF ($p_{nom} = 600$ bar and $ET = 750 \mu\text{s}$).	82
4.10	Accuracy of the estimated injected mass.	83
4.11	Injection system prototypal hardware.	84
4.12	Time histories of the mass flow-rates at the injector inlet.	86
4.13	Correlation between the $M_{inj,in}$ and the M_{inj} .	87
4.14	M_{inj} performance related to different control strategies ($T_{tank} = 40 \text{ }^\circ\text{C}$).	88
4.15	M_{inj} performance related to different control strategies ($T_{tank} = 68 \text{ }^\circ\text{C}$).	88
4.16	Comparison of the ΔM_{inj} performance for different p_{nom} and T_{tank} values.	89
4.17	Performance of the estimated M_{inj} when the closed-loop strategy is activated ($p_{nom} = 1600$ bar, $T_{tank} = 68 \text{ }^\circ\text{C}$ and $M_{inj,ref} = 40$ mg).	90
4.18	Coefficient of variation in the M_{inj} for different p_{nom} and T_{tank} values.	92
4.19	Dynamic response to steps in p_{nom} and $M_{inj,ref}$ values.	93
4.20	Dynamic response to ramps in p_{nom} and $M_{inj,ref}$ values.	94
4.21	Pilot-main injected mass as a function of p_{nom} and DT with the standard system.	94
4.22	DT sweeps.	95
5.1	The comparison between the polytropic and the classic flows ($p_0 = 1$ bar, $T_0 = 400$ K, $p_{out} = 0.6$ bar, $L_{max,Fanno} = 80$ m)	102
5.2	The comparison between the polytropic and the classic flows ($p_0 = 1$ bar, $T_0 = 400$ K, $p_{out} = 0.3$ bar, $L_{max,Fanno} = 40$ m)	103
5.3	The comparison between the polytropic and the classic flows ($p_0 = 5.57$ bar, $T_0 = 900$ K, $u_{in} = 1000$ m/s, $L_{max,Fanno} = 35$ m)	105

5.4	The comparison between the polytropic and the classic flows ($p_0 = 5.57$ bar, $T_0 = 1000$ K, $u_{in} = 1000$ m/s, $L_{max,Fanno} = 60.15$ m)	105
5.5	The comparison between the numerical results and the Fanno flows under subsonic conditions.	109
5.6	The comparison between the numerical results and the Fanno flows under subsonic conditions.	110
5.7	The polytropic exponent along the pipe (Point 1: $p_0 = 1$ bar, $T_0 = 400$ K, $p_{out} = 0.6$ bar, $L_{max,Fanno} = 80$ m; Point 2: $p_0 =$ 1 bar, $T_0 = 400$ K, $p_{out} = 0.3$ bar, $L_{max,Fanno} = 40$ m; Point 3: $p_0 = 5.57$ bar, $T_0 = 900$ K, $u_{in} = 1000$ m/s, $L_{max,Fanno} =$ 35 m; Point 4: $p_0 = 5.57$ bar, $T_0 = 1000$ K, $u_{in} = 1000$ m/s, $L_{max,Fanno} = 60.15$ m).	110

List of Tables

3.1	Working condtions and the parameters analyzed	63
4.1	Injected mass measured at the hydraulic test rig with the lookup table calibrated at the dynamometer cell.	92

Nomenclature

Roman Symbols

H	source vector
w	characteristic variable vector
C	Jacobian matrix
CF	Common-Feeding
CN	combustion noise
CR	common rail
C	chamber
ECU	electronic control unit
FFT	fast Fourier transform
FMV	fuel metering valve
L	pipe
NCS	Needle Closing Sensor
NO_x	nitrogen oxides
PCCI	premixed charge compression ignition
PCV	pressure control valve
R	restrictor
STFT	short time Fourier transform

TFA	time-frequency analysis
A	area
C	flow coefficient, heat capacity
c	sound speed
D	diameter
DC	duty cycle
DT	dwell time
E	energy
EAR	equivalent area ratio
EOI	end of injection
ET	energizing time
f	friction factor
G	mass flow-rate
g	signal function
H	source variable
h	window function
I	current
IFT	injection fusion threshold
ITL	injection temporal length
J	impulse
K	geometrical term
L	length
l	length of pipe

M	mass
m	polytropic exponent
Ma	Mach number
MIF	mean instantaneous frequency
N	number of injector solenoid windings, number of samples
NCD	nozzle closure delay
NOD	nozzle opening delay
P	energy density
p	pressure
Q	volumetric flow-rate
R	reluctance, elasticity constant of the perfect gas
Re	Reynolds number
s	entropy
SOI	start of injection
t	time
u	flow velocity
V	volume
w	characteristic variable
x	space coordinate

Greek Symbols

α	needle valve cone angle
γ	isentropic exponent
μ	dynamic viscosity

μ_0	magnetic constant
ν	kinematic viscosity, frequency
ρ	density
Σ	cross section of the magnetic circuit
σ	coefficient of variation
τ	shear stress, time reference
ε	pipe roughness size, error

Mathematical Symbols

0D	zero-dimensional
1D	one-dimensional
3D	three-dimensional

Subscripts and superscripts

0	reference, stagnation
*	at the duct location where flow is choked
<i>A</i>	hole A
<i>acc</i>	accumulator
<i>after</i>	after injection
<i>C</i>	chamber
<i>cc</i>	control chamber
<i>cp</i>	control piston
<i>cr</i>	critical
<i>cum</i>	cumulated
<i>dc</i>	delivery chamber

<i>do</i>	downstream
<i>dyn</i>	dynamic
<i>est</i>	estimated
<i>f</i>	final
<i>fil</i>	filtered
<i>gap</i>	air gap between magnet and armature
<i>i</i>	computational node number, initial
<i>in</i>	inlet
<i>inj</i>	injector, injected
<i>m</i>	electromagnetic
<i>main</i>	main injection
<i>n</i>	time instant
<i>ne</i>	needle external
<i>nom</i>	nominal
<i>or</i>	orifice
<i>out</i>	outlet
<i>p</i>	at constant pressure
<i>pil</i>	pilot injection
<i>R</i>	restrictor
<i>ref</i>	reference
<i>s</i>	following isentropic process
<i>sat</i>	saturated
<i>st</i>	steady state

un unsteady

v at constant volume

w wall

Z hole Z

Chapter 1

Introduction

The world has witnessed the global energy demand and consumption at the industrial field. Particularly, road vehicles powered by means of internal combustion engine are among major consumers [1].

In recent decades, automotive engine researchers are compelled to work both in the fuel field and in the engine design field in order to accomplish with the increasingly rigorous emission standards [2]. As regards the first topic, different fuel blends are examined under various engine working conditions to realize more economic and cleaner solutions [3]. As far as the latter theme is concerned, most efforts are focused on the combustion modes [4], on the after-treatment instruments [5], as well as on the injection systems [6].

Fuel injection systems are the devices, which introduce small doses of required fuel into the combustion chambers. Within recent years, particular researches and developments in injection systems [7][8] have been carried out.

Common rail (CR) injection systems, firstly and successfully applied at the end of 20th century, has passed some generations. Nowadays, modern CR injection systems are capable to provide accurate fuel metering, injection timing, control of the injection rate and high capability to manage multiple injections and injection rate-shaping [9].

In terms of common rail injection systems in lab activities, numerous studies have been carried out. Whereas, it remains possible to optimize certain aspects, including flowmeters to evaluate the injection rate, the mechanic hydraulic structure of the system and the related control strategies.

1.1 Fuel injection rate flowmeters

For the purpose of measuring the fuel injected mass and the injected flow-rate time histories, based on different working principles, varieties of flowmeters have been developed. Flowmeters are generally among those four types: Coriolis, gear-type, positive-displacement and pressure-increase principle based [10]. Nevertheless, in order to accurately characterize the injection properties, only the pressure-increase principle-based flowmeters are suitable, although the devices following other theories are likewise employed in industry.

Following the pressure-increase principle, the first variety of devices is Zeuch method-based, which has been diffused in the last few years. The Mexus flowmeter, produced by Loccioni, and the HDA flowmeter from Moehwald Bosch follow this approach. Those instruments feature a constant volume chamber, filled with the testing oil. The increase of the inside chamber oil pressure, caused by injections introduced by an injector, is measured by means of a piezoresistive sensor. Other information such as the oil compressibility is directly obtained by means of algebraic manipulations with the medium sound speed, which is characterized in real time. Therefore, the state equation is no more necessary for such devices [11][12]. Whereas, since the resonance phenomena may occur in the measuring chamber, the obtained pressure signal is required to be filtered [13]. Moreover, possible reverse flows, from the chamber to the nozzle of the injector, have been discovered at the instants right after the start of the energizing currents of injections. Therefore, the perception of the effective nozzle opening delay can be misled [14]. Finally, shock-like waves, which may be reflected in a complicated way in the chamber, can be generated due to the high-pressure injection. Thus, low-frequency components would be formed and are likely to remain in the final injection rate signal, since that cannot be eliminated by a low-pass filter [15].

The second subcategory of the devices pertaining to the pressure-increase type is based on Bosch method [16]. EVI flowmeter from IAV follows this approach. With this method, the fluid flow properties are determined, as the flow goes through a constant area long tube. The pressure waves generated by the sudden flow-rates of injections are caught by means of a piezoelectric pressure sensor. The 1D velocity of the oil can be found after certain manipulations by following the hydraulic pulse theory [16]. The final calculated flow-rate signal is enough smooth. Thus, no low-pass filter is necessary to be applied. However,

weak points of this methods still remain. A numerical integration is required when computing the injection rate [17]. Therefore, the errors generated, due to the transducer or the design of the instrument, can be as well accumulated.

Moreover, instability in the injection rate signal has been observed after the end of the injections [13] [18]. This effect not only prevents an accuracy detection of the effective end of injections, but also worsens the evaluation of the injected quantity, particularly in multiple injection patterns.

Lastly, another distortion of the signal has been found: during a large injection, the EVI output injection rate tends to increase although the experimentally measured injection pressure decreases [19].

Generally Zeuch method is nowadays considered as the one, which is capable to realize a more accurate result [13][14], although the reasons for the inaccuracy in the Bosch method are not clarified in the literature.

1.2 Optimization of injection systems

The common-rail (CR) fuel injection systems for diesel engines have been investigated for decades [20]. CR injection systems, capable to control the injection timing under high pressures (up to 2500 bar), are globally employed as a key instrument for the next step evolution of diesel engines [21][22]. Meanwhile, the state-of-the-art CR systems give the possibilities of regulating all variables of injections with high accuracy and robustness under all engine working conditions [23].

Over the recent years, contributions have been made to CR system structures in different aspects. Firstly, a great deal of the attentions has been paid to the fuel spray and the flow-rate pattern [24], while in terms of the framework of the system, in order to establish ultra-high nominal pressure and to maintain low static leakages, which improves the system energy consumption, the pressure balanced pilot valve has been adopted in the injectors [25]. Thanks to this balanced valve, the injector dynamic response is as well enhanced. Similarly, as a Minirail is integrated into an injector inner hydraulic circuit, fuel atomization can be improved, and the injector inner leakage can be reduced [26]. The control-plate, employed to restrict the fuel flow through the pilot valve, is another innovative component installed in the injector control chamber [27].

In addition, some efforts have been put forward to optimize the structure of the entire system [28]. Among those researches, the Common-Feeding (CF) system, integrating the accumulator into the high-pressure pump, is among the optimization methods to reduce the manufacturing costs and to be simply mounted onto a diesel engine, due to the absence of the rail [29][30].

As far as the injection patterns are concerned, a series of rate-shaping profiles have been proposed and tested [31][32]. As the fuel is injected by means of a set of consecutive small injections, the strategy is referred to as digital rate-shaping [33]. When such a technique is applied, after a fuel front jet has been injected into the cylinder as the first shot, the subsequent shots tend to generate eddies, and include an additional air content in the liquid droplets or in the vapour phase around the jet. Therefore, it enables an enhanced control of the heat release grow [34], and the potential of a reduction in fuel consumption has been shown [32].

Another innovative injection schedule is continuous rate-shaping [35]. Analogous to the impact of closely-coupled pilot-main injection schedules [33], boot-like, ramp-like and wedge-like injections, which mainly decrease the injected flow-rate of the main injection initial phase, reduce the autoignition delay in the premixed phase between the fuel and the air [36]. In consequence, the heat release rate is restrained [37], and the combustion noise (CN) declines [38]. Meanwhile, a lower flame temperature mitigates the NO_x emissions [39]. On the other hand, an after injection with a dwell time (DT) of only a few crank angle degrees has been found to be beneficial for the reduction of soot emissions [40].

In general, rate-shaping strategies have only been applied to a direct acting piezoelectric injector [36], which lifts the needle by charging a piezo-stack mounted along the needle axis [41].

On the other hand, it is widely believed that state-of-the-art solenoid indirect acting injection systems are only capable to realize regular multiple injection patterns [42]. As the DT between two energizing currents, whose function is to activate injection events, is below a certain threshold, an injection fusion takes place, and the fuel metering accuracy evidently reduces [14]. Efforts have been put forward as well to exploit indirect acting systems' potentiality in digital and continuous rate-shaping strategies [35][27]. When multiple injections with quite short DT s are applied to this system, the injected mass of the subsequent shots

can be evidently affected by the changes in the injector inside fuel pressure evolution [43]. Furthermore, it has been preliminarily demonstrated that within the injection fusion threshold (*IFS*), as the *ET*s of the two shots are unchanged, a *DT* range in which the cycle-to-cycle dispersion of the fuel injected quantity is small could exist [35]. Whereas, the rate-shaping strategies linked *DT* area, which can be exploited and can be applied to the production engines, are small, due to a constrain of the maximum acceptable cycle-to-cycle variation of engine performance. Even though numerous researches related to the innovative strategies have been carried out [44][45][46], design keys in the injector setup for improving the rate-shaping injection patterns are not available in the literature.

1.3 Closed-loop control strategy

High levels of NO_x and soot engine out emissions are the well-known challenges under conventional diesel engine operations [47]. In order to achieve the targets of high efficiency, of reduced CN and of extremely low emissions, innovative combustion modes have been under research for years [48].

As a result, premixed charge compression ignition (PCCI) is frequently applied to modern diesel combustion strategies. As this mode is adopted, the fuel can be fully or partially premixed in advance of the combustion phase, and the multipoint auto-ignition of a lean mixture induces a low temperature combustion within the cylinder [49][50]. The lower temperature of the combustion is capable to reduce heat losses [49]. Meanwhile, if the sufficient long time is provided for the charge mixing, NO_x and soot formation can be as well mitigated [51][52].

As far as the diagnosis techniques are concerned, in-cylinder pressure measurement and analysis play an important role[53][54]. By analyzing a properly processed pressure signal, vital characteristics of the combustion process can be identified. Such researches include the detection and the control of the start of combustion [55], heat release rate [56] as well as knock and misfire phenomena [57][58]. Meanwhile, by dealing with same signal, empirical models have been established to determine the ignition delay [59] and the barycenter of combustion [60].

Over recent years, time-frequency analysis (TFA), which is a powerful tool to analyze non-stationary signals [61], has been employed to detect and to

diagnose machinery faults [62][63]. Such an advanced technology has also been introduced to investigate vibration, combustion and knock in diesel engines by evaluating the vibration signals in these engines [64][65]. Among those methods, short time Fourier transform (STFT) is applied to characterize signals in the time-frequency domain for plenty cases. For instance, it has been used to estimate the combustion characteristics parameters like combustion peak pressure and peak pressure rising rate through the vibration signal [66]. Another research, in which analysis of the in-cylinder pressure resonance is used to predict the trapped mass, has been carried out in [67][68]. The detection of vibration sources in mechanical systems and of the main events occurred in a fuel injection apparatus have been developed as well [69][70].

Nowadays modern CR systems are generally equipped by diesel engines [71]. Among those, the more diffused CR systems possess solenoid pilot valves, with which the injection performance is indirectly controlled. In such a system, the injected fuel quantity is determined by both the nominal rail pressure (p_{nom}) and the duration (ET) of the electrical current signal, which keeps the pilot valve open [72]. The p_{nom} and the ET values are both stored in the electronic control unit (ECU) calibration maps, which are calibrated through a set of experimental tests [34]. Although feedbacks of the p_{nom} and of the injection timings are received by the ECU, the injected mass remains to be controlled in the open-loop type. Moreover, the needle valve dynamics and the pressure fluctuations, triggered by the opening and closure events of the injector nozzles, possibly disturb the multiple injection performance [35]. Meanwhile, in order to enable the specific combustion modes, complex injection strategies present high requirements to injection systems, and even one series of the latest generation indirect acting injectors are characterized by some hydraulic instability, as the DT is reduced below a certain threshold [35]. Therefore, the satisfactory accuracy of the injected mass of each shot turns to be a challenge. In addition, the engine thermal regime can evidently affect the effective injected mass, even though p_{nom} and ET are preset [73].

Numerous studies have been carried out to develop a robust closed-loop control strategy of the injected fuel quantities in a diesel injection system [74]. On the basis of two empirical physical equations, a fuel delivery sensing technique has been proposed for diesel injection systems [75]. The first equation correlates the fuel volumetric flow-rate to the needle lift, which is captured by

means of a displacement sensor integrated in the injector, while the second equation derives the fuel properties from the thermal regime. Similarly, another method is proposed for estimating the injected mass through a simple engine diagnostic model, which can be integrated into the ECU [76]. In this method, the effective injected mass is determined by considering the difference of the oxygen fractions between the inlet and the outlet of the cylinder. Both the ratios are acquired by means of lambda sensors. While another model estimated exhaust manifold oxygen fraction, used to evaluate the target injected mass, is derived from the model by timely knowing the combustion mode and the oxygen fraction at the intake pipe. Those two ratios at the outlet are compared and the difference between the target and the authentic injected mass can be obtained. Whereas, in this technique, the exhaust gas recirculation of the engine is considered null, and a sophisticated calibration and the accurate measurement of the gas properties along the ducts are required. In the third technique, a hot wire anemometer, with Ti/Pt metallization on a low temperature co-fired ceramic substrate, is integrated inside the injector nozzle. The injected fuel quantity is thus evaluated by means of the maximum deviation of a balanced Wheatstone bridge [77].

Meanwhile, some main injection apparatus suppliers have as well produced the injectors capable to compensate the errors in the injections. A piezoelectric pressure sensor, mounted in the pilot stage of the i-Art injector from DENSO [78], provides the pressure time history of the control chamber. A series of key time instants, such as the start of injection (*SOI*), the maximum injected flow-rate timing and the end of injection (*EOI*) are captured [27], and applied to an empirical model [79]. The injected mass is thus derived. Needle Closing Sensor (NCS), designed by Bosch, is similar to the i-Art system [34]. In this system, a force transducer is applied to measure the force in the control chamber due to the fuel pressure. The vital instants are recorded to predict the injector needle lift. The effective injected mass is in turn evaluated by means of a correlation with the needle lift trace as an input. In addition, "Switch" technology of Delphi includes the needle into the electric circuit [80]. If the needle arrives at the upper stroke-end or reaches the needle seat, the circuit is closed in two distinguishable ways. Since the voltage of one location within the circuit is monitored, the real time needle movements can be identified, and again a model

that links the needle lift and the injected fuel quantity is applied to obtain the final results.

All above introduced control strategies generally focus on either a correlation between the needle lift trace and the injected quantity or a combustion model. Meanwhile, the techniques, proposed by the suppliers, are compensation strategies, rather than a genuine closed-loop control of the injected mass. Those techniques possibly improve certain operating conditions while worsening the others. Therefore, the difficulties remain to realize an accurate control of the injected mass that can be applied to the entire engine working range.

1.4 Compressible flow in constant area ducts

In order to improve the estimation of the instantaneous flow-rates supplied by common rail systems, it is possible to adopt theoretical 1D compressible flow models. Within this topic, Fanno model and Rayleigh model have been developed for decades. Those two models hold either under the assumption of viscous adiabatic flow, or for the hypothesis of inviscid diabatic flow [81]. The models are derived from the conservation equations of mass, of momentum and of energy [82] and viscous adiabatic flow model allows the closed form prediction of the steady-state flow characteristics at any location along the duct, as long as the boundary conditions, the Mach number and the frictions factor there are known [83]. On the other hand, even under steady state, viscous diabatic flow, which is a more general case, can only be solved numerically.

Fanno flow model is generally applied to the design and analysis of nozzles coupled with ducts. Under this calculation method, the diverging or converging area in a nozzle is modelled with isentropic flow, while the constant area section of the pipe follows the Fanno's approach. In order to simplify the analysis, the fluid in the model is regarded as a perfect gas (although possibly a liquid), and the friction is modelled as a shear stress on the gas from the duct walls [84].

In the design and diagnostics of industrial equipments, the matters of compressible flows within pipes and other configurations are often encountered by the engineers [85]. The layout and analysis of process gas distribution systems, the sizing and qualification of safety devices such as pressure relief valves and rupture disks, and the modeling of accident consequences and release rates in the chemical and nuclear industries all require the 1D compressible flow

calculation, within which the friction loss should be considered [86]. In addition, the recent important applications of Fanno flow concern the micro-scale fluid flow channels in electronics [87], the heat pumps [88], reactors, heat exchangers [89], aerospace engineering, ejectors [90] and so on.

Besides the numerous applications, other works investigate the problems of the compressible flow evolution in pipes with constant area from a more theoretical point of view. Due to the effects induced by the compressibility, the friction is no more constant and cannot be accurately estimated by the canonical fluid dynamic correlations (e.g. Colebrook-White and Blasius), since these are developed through experimental data of incompressible flows. It has been elaborated that the compressibility tends to flatten the velocity profile and the velocity gradient at the wall is thus changed [91][92]. Such flattening of the profile as well influences the dynamic pressure and temperature, which should be taken into consideration to realize an accurate estimation of the flow properties. An accurate compressible correlation for the friction coefficient should include both the Reynolds number and the Mach number, when it is not possible to assume the flow is incompressible. The correlations for the friction coefficient or K_i factor in Fanno flow have been developed for both turbulent flows [93] and laminar flows [92]. Moreover, in order to consider the viscous losses in fittings other than straight pipes, a resistance coefficient or K_i factor is determined for each fitting, and the global system K factor is calculated by summing all the frictional losses of the straight pipes and of the fittings ($K = fL/D + \sum K_i$). In consequence, the global K factor stands for the head lost of the fluid during the flow through the entire system [94].

1.5 Contributions and outline

In this thesis, the benchmark tests have been performed between two types of the injection rate flowmeters. A new Common-Feeding injection system for light duty commercial vehicle has been developed, and the influence of injector setup on digital and continuous injection rate-shaping performance has been investigated. Furthermore, different innovative closed-loop control strategies of injected mass have been established. Finally, in the field of fluid dynamics, compressible flows in constant area ducts with friction have been approximated in polytropic processes.

In Chap. 2, the injected flow-rate of a common-rail solenoid injector has been tested with both Zeuch and Bosch method-based devices. A one-dimensional numerical model of EVI flowmeter has been developed, in order to investigate the cause and effect relationship between the device design and the obtained injection rate signal. The specific attention has been paid to the alteration of the injected-flow rate signal through Bosch method-based devices, and optimization methods have been provided to improve the performance of Bosch method-based instruments. The content of this chapter is based on the work of [95].

In Chap. 3, with respect to the topic of Common-Feeding system, an innovative prototype has been designed and manufactured in order to be applied to a light duty commercial diesel engine produced for the Asia market. The experiments have been performed on both the CR and the CF systems in terms of single injections and pilot-main injections. The time distributions of the oil pressure within the hydraulic circuit and of the injection rate, the injector static and dynamic leakages, the nozzle opening and closure delays (*NOD* and *NCD*) as well as the injected quantity cycle-to-cycle dispersions have been acquired and analyzed. As regards the optimization of the injection setup of solenoid injection systems for rate-shaping strategies, a numerical-experimental investigation on a state-of-the-art CR system has been performed at the hydraulic test rig. With the help of the numerical model, which contains mechanical, electrical and hydraulic setups of the injection system, parametric analyses have been done to investigate the cause and effect relationship between the design and the possibilities to realize certain types of rate-shaping strategies. The key parameters have been highlighted to provide an optimization guideline to the suppliers. Finally, two state-of-the-art injectors, one equipped with an integrated Minirail (CRI 2.20) and the other without it (CRI 2.18) have been examined and compared, in order to apply and to verify the numerical test results. The content of this chapter is based on the work of [96] and [97].

In Chap. 4, by analyzing the instantaneous fuel pressure within the rail-to-injector pipe, two new methods for estimation of the injected mass have been presented. One applies the TFA methodology, while the other is based on Euler equations. A prototypical hardware has been realized with respect to the second method. Experimental tests on both single and pilot-main injections have been performed at the hydraulic rig. The comparisons of injection mass

accuracy between the system equipped with the innovative control strategy and the state-of-the-art systems have been performed. The content of this chapter is partially based on the work of [98] and [99].

In Chap. 5, a new accurate calculation method for characterizing adiabatic viscous compressible flow have been provided. A polytropic evolution is assumed to simulate the compressible flow in constant area ducts with friction. Constant polytropic exponents have been determined through the inlet and the outlet flow properties of the Fanno flow, and the comparisons have been made between the results derived from the classic method and from the new polytropic method. A numerical model, in which the polytropic index is calculated piece by piece from the fluid properties along the Fanno flow, has been established, and the results of the numerical model have been compared with those of the classic Fanno flow.

Chapter 2

Benchmark of the flowmeters

2.1 Experimental setup

The experimental campaign has been conducted on the Moehwald Bosch hydraulic bench installed at the ICE laboratory in Politecnico di Torino [44]. HDA, Mexus and EVI flowmeters are equipped on the bench. Moreover, the energizing current time history for the injector is measured by means of a current clamp.

A Bosch common rail system equipped with CRI 2.16 injector is employed to conduct all the experiments in this chapter. All the experimental tests have been performed with a fixed pump speed of 1000 rpm, corresponding to an engine speed of 2000 rpm for the investigated common rail system. Since this parameter does not influence the performance either of the flowmeter or of the injection system, the conclusions can be generalized to any other engine speeds.

The bench and injection system are fed with the ISO 4113 oil, which is commonly applied to simulate the diesel fuel in laboratories. The scheme of the Bosch method-based device, EVI, is reported in Fig. 2.1, and the detailed features of the tip adapter are shown in Fig. 2.2. The tested injector is installed on the tip adapter (cf. item 1 in Fig. 2.1 and item 4 in Fig. 2.2). As the injector is well mounted, the nozzle tip arrives at the chamber, created by the spacer (cf. item 2 in Fig. 2.2), which is between the injector adapter (cf. item 3 in Fig. 2.2) and the fitting device (cf. item 4 in Fig. 2.2). A damper, which is not shown in Fig. 2.2, is mounted downstream of the injector nozzle, in order to protect the temperature and pressure transducers (cf. item 5 and item 6 in Fig. 2.2). Two drilled holes into the measuring pipe on the fitting device are

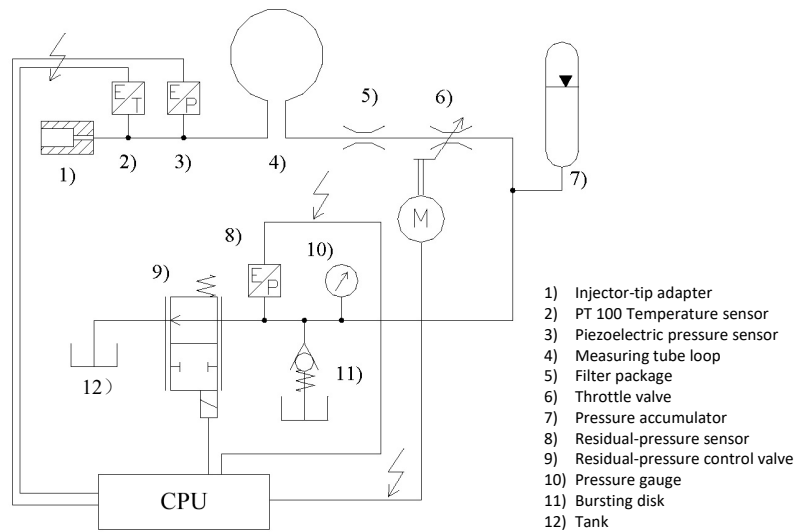


Figure 2.1: EVI schematic.

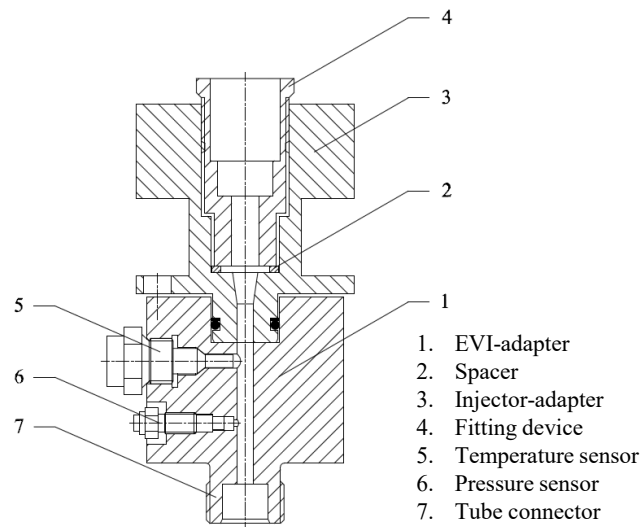


Figure 2.2: EVI device internal feature.

used to fit those two transducers, and two chambers are left in the hydraulic measuring circuit as the sensors are installed. The adapter, with the help of a connector (cf. item 7 in Fig. 2.2), is connected to a pipe featuring a length of 11 m. A throttle valve (cf. item 6 in Fig. 2.1) driven by a step motor, another pressure transducer (cf. item 8 in Fig. 2.1) and a residual-pressure control valve (cf. item 9 in Fig. 2.1), which is capable to expel the extra fuel into the tank (cf. item 12 in Fig. 2.1), are mounted at the other extremity of the 11

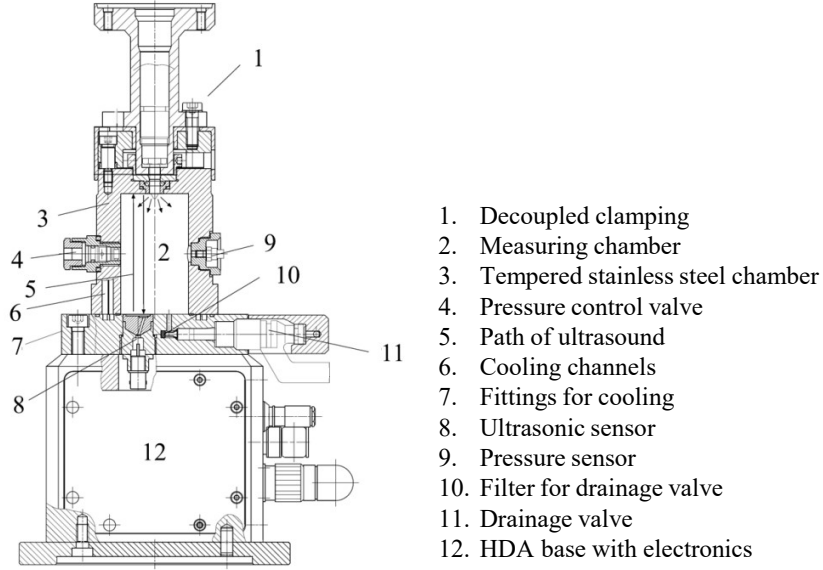


Figure 2.3: HDA schematic.

meters long pipe. As the devices are functioning, the residual fuel pressure along the measuring pipe is kept around 40 bar.

The HDA, whose layout is shown in Fig. 2.3, features a more compact structure. The clamping (cf. item 1 in Fig. 2.3), in which the injector is installed, is fixed at the top of the measuring chamber (cf. item 2 in Fig. 2.3). A pressure control valve (cf. item 4 in Fig. 2.3), an ultrasonic sensor (cf. item 8 in Fig. 2.3) and a drainage valve (cf. item 11 in Fig. 2.3) are mounted within the chamber, inside which the pressure is controlled as well around 40 bar. Meanwhile, the cooling channels (cf. item 6 in Fig. 2.3), surrounding the chamber, are designed to keep the chamber inside temperature at an adjustable value ($\approx 40\text{ }^{\circ}\text{C}$).

2.2 Zeuch and Bosch methods

In the Zeuch method-based instrument, which is HDA (cf. Fig. 2.3), the injected flow-rate is calculated through the equation [11]

$$G_{HDA} = V \frac{d\rho}{dt} = \frac{V}{c^2} \cdot \frac{dp}{dt} \quad (2.1)$$

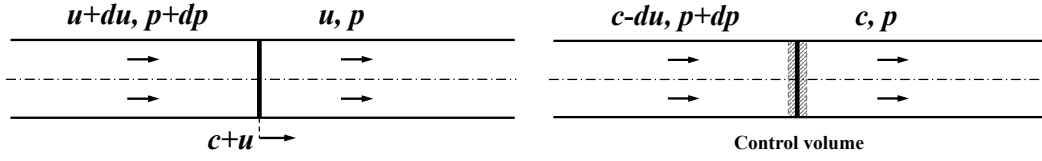
where G_{HDA} , V , ρ , c and p respectively are the mass flow-rate pertaining to the injection in the HDA measuring chamber, the fixed volume of the chamber, the fluid density, the sound speed and the fluid pressure captured by means of the pressure transducer (cf. item 9 in Fig. 2.3) inside of the chamber. c in Eq. (2.1) is evaluated by means of an ultrasonic sensor (cf. item 8 in Fig. 2.3) each time as the injection is performed. It follows that it is able to keep the accuracy of c with a change in the fluid temperature or even with cavitation occurred in the chamber.

On the contrary, the Bosch method-based EVI device evaluates the injection rate upstream of the 11 m long pipe, which starts at item 1 and ends at item 9 in Fig. 2.1. The mass flow-rate writes

$$G_{EVI} = A \cdot \rho \cdot u \quad (2.2)$$

where A is the pipe flow area and u is the 1D flow velocity around the pressure transducer (cf. item 3 in Fig. 2.1). Since the flow area is fixed, and the density is determined by knowing the temperature through item 2 in Fig. 2.1 and the pressure through item 8 in Fig. 2.1, G_{EVI} is a function of only u . The tube is initially filled with pressure test oil. The injection led pressure wave along the tube is monitored by means of item 3 in Fig. 2.1. This pressure wave travels with a speed equal to $u + c$ (cf. Fig. 2.4a). The velocity and the pressure upstream the wave front are respectively $u + du$ and $p + dp$, and the corresponding values downstream of the wave front remain u and p . As a moving reference frame is considered, the reference speed can be unified with that of the pressure wave front. Under such circumstances, the flow velocity leaving the wave front turns to be $c - du$, and the one enters the front is c . Mass conservation and momentum balance equations are applied to the infinitesimal volume in Fig. 2.4b, which contains the wave front, and those equations write

$$\begin{cases} A \cdot \rho \cdot c = A \cdot (\rho + d\rho) \cdot (c - du) \\ A \cdot \rho \cdot c^2 = A \cdot (\rho + d\rho) \cdot (c - du)^2 + A \cdot dp \end{cases} \quad (2.3)$$



(a) Fixed frame of reference

(b) Moving frame of reference

Figure 2.4: Pressure wave front in the measuring tube with different reference frames.

The density perturbation can be found after manipulations in the mass conservation equation in Eq. (2.3), and it writes

$$d\rho = \rho \frac{du}{c} \quad (2.4)$$

Meanwhile, the pressure increment, obtained from the momentum balance equation in Eq. (2.3), is

$$dp = 2\rho c du - c^2 d\rho \quad (2.5)$$

Combining Eq. (2.4) and (2.5) and knowing the definition of the speed of sound ($dp = c^2 d\rho$), the change in u can be expressed as

$$du = \frac{dp}{\rho c} \quad (2.6)$$

Substituting an integration of Eq. (2.6) over a fixed time length into Eq. (2.2), the mass flow-rate along the tube can be determined,

$$G_{EVI}(t) = \frac{A}{c} \int_0^t dp \quad (2.7)$$

The sound speed is not measured directly in this instrument, whereas it is determined by means of a state equation as a function of the captured pressure and the measured temperature values inside the measuring tube, which differs from the device that applies Zeuch method. As a consequence, the inaccuracy in the mass flow-rate resulted from the estimated sound speed can be significant.

Therefore, an optimization of the EVI flowmeter can be an additional installed transducer, with which the sound speed of the fluid along the pipe is measured.

2.3 Numerical model

The hydraulic model of the EVI, whose schematic is reported in Fig. 2.5, has been developed in MATLAB environment. The code contains 0D chamber elements, connected by means of either 1D pipes or restrictions.

In Fig. 2.5, the injected mass flow-rate time history obtained by means of the HDA under the same working conditions is employed as the boundary condition at the chamber C_1 , which is the clearance volume delimited by the spacer (cf. item 2 in Fig. 2.2), the injector adapter (cf. item 3 in Fig. 2.2) and the fitting device (cf. item 4 in Fig. 2.2).

The damper is considered as a concentrated resistance R_1 , and a conical 1D pipes L_1 is placed downstream of the damper. The measuring pipe (cf. L_2 in Fig. 2.5), placed after the conical pipe, possibly introduces a time delay between the injection events and the pressure variation detected by means of the pressure sensor, which is located at the C_4 in Fig. 2.5. In order to reduce this time difference and to leave enough long distance to obtain a fully developed flow (any two- or three-dimensional effect should finish at the mounting points of the transducers along the pipe L_2), both the pressure and the temperature sensors are installed at a certain distance downstream of the conical pipe. Among those, the temperature sensor is mounted in one chamber, modelled as C_2 in Fig. 2.5. Lastly, C_3 simulates the junction that links a 1D duct to the

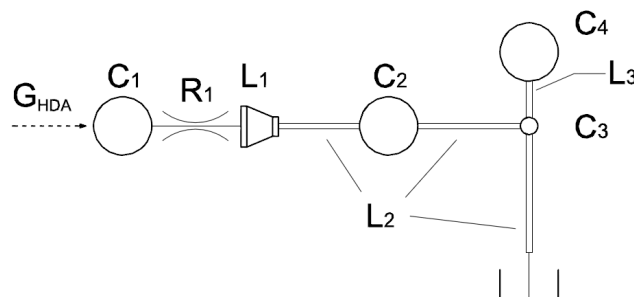


Figure 2.5: Schematic of the EVI hydraulic model.

chamber C_4 and the measuring pipe L_2 . Furthermore, combining chamber C_4 and pipe L_3 , a Helmholtz resonator model is formed.

The duct L_2 goes out of C_3 and arrives at an oil tank. This piece of pipe L_2 contains a tube loop of approximately 11 m (cf. the part of the pipeline between items 3 and 9 in Fig. 2.1), which is designed to avoid the pressure waves, reflected at the throttle valve (cf. item 6 in Fig. 2.1), reaching the pressure sensor during the measurement of the fuel injection.

The throttle valve and the residual pressure control system (cf. items 7-9 in Fig. 2.1) are not modelled in Fig. 2.5, since the reflected pressure waves arrive at C_3 later than the end of the simulation. Therefore, this part is simplified into a tank (cf. Fig. 2.5) with a constant pressure kept at 40 bar.

In the following sections, the submodels and the numerical algorithm are respectively described.

2.3.1 1D pipe-flow model

The fluid dynamics along the pipe L_1 and L_2 is governed by the generalized Euler partial differential equations of mass conservation and momentum balance as following

$$\frac{\partial}{\partial t} \begin{bmatrix} \rho \\ \rho u \end{bmatrix} + \frac{\partial}{\partial x} \begin{bmatrix} \rho u \\ \rho u^2 + p \end{bmatrix} = \begin{bmatrix} -\frac{\rho u}{A} \cdot \frac{dA}{dx} \\ -\frac{4\tau_w}{D} \end{bmatrix} \quad (2.8)$$

where t is the time and x is the space coordinate along the duct axis; ρ , u , p are respectively the average cross-sectional density, velocity and pressure of the test oil; D and A are the internal diameter and the flow area of the duct; τ_w is the wall friction shear stress. The thermal dynamic process is assumed as isothermal, and the temperature value captured by means of temperature sensor in the EVI device is applied to the model. Thus, the energy equation has been discarded, and the fluid state equation is reduced to $\rho = \rho(p)$. The fitting data on the dependence of the temperature and the density for ISO 4113 oil are available in [100].

According to the decoupling method described in [101], Eq. (2.8) can be rearranged as

$$\frac{\partial \mathbf{w}}{\partial t} + [\mathbf{C}] \frac{\partial \mathbf{w}}{\partial x} = \mathbf{H} \quad (2.9)$$

where $[\mathbf{C}]$ is the diagonalized Jacobian matrix of the system, written as

$$[\mathbf{C}] = \begin{bmatrix} u+c & 0 \\ 0 & u-c \end{bmatrix} \quad (2.10)$$

\mathbf{w} is the characteristic variables as following

$$\delta\mathbf{w} = \begin{bmatrix} \delta w_1 \\ \delta w_2 \end{bmatrix} = \begin{bmatrix} \delta p + \rho c \delta u \\ \delta p - \rho c \delta u \end{bmatrix} \quad (2.11)$$

and \mathbf{H} is the source term

$$\mathbf{H} = \begin{bmatrix} H_1 \\ H_2 \end{bmatrix} = \begin{bmatrix} \frac{4c\tau_w}{D} + (u-c) \cdot c \cdot \frac{\rho u}{A} \cdot \frac{dA}{dx} \\ -\frac{4c\tau_w}{D} - (u+c) \cdot c \cdot \frac{\rho u}{A} \cdot \frac{dA}{dx} \end{bmatrix} \quad (2.12)$$

The Darcy-Weisbach equation is employed to determine the steady state component of the wall friction expressed as

$$\tau_{st,w} = \frac{1}{8} f \rho |u| u \quad (2.13)$$

in which f is the friction factor and can be written as a function of the Reynolds number ($Re = Du/\nu$ with ν representing the fluid kinematic viscosity) and of the ratio of the pipe roughness size (ε) to D [102]

$$\frac{1}{f} = \left(\frac{Re}{64}\right)^\alpha \cdot (1.8 \log \frac{Re}{6.8})^{2(1-\alpha)\beta} \cdot (2 \log \frac{3.7D}{\varepsilon})^{2(1-\alpha)(1-\beta)} \quad (2.14)$$

where the exponents α and β are the functions of Re , D and ε , reported as

$$\begin{cases} \alpha = \frac{1}{1 + (Re/2720)^9} \\ \beta = \frac{1}{1 + [Re/(160D/\varepsilon)]^2} \end{cases} \quad (2.15)$$

Eq. (2.14) is an explicit formula to express f , and is a good approximation of the Moody diagram at all flow regimes. A steady state friction model is thus obtained by combining Eq. (2.13)-(2.15).

As the impulsive working and high-frequency pressure waves are present in one hydraulic system, the unsteady friction ($\tau_{un,w}$) should be as well considered.

Therefore, the wall friction shear stress applied can be expressed as

$$\tau_w = \tau_{st,w} + \tau_{un,w} \quad (2.16)$$

The unsteady friction shear stress can be calculated as a time convolution integration according to [103]

$$\tau_{un,w} = \frac{4\rho\nu}{D} \int_{-\infty}^t \frac{\partial u}{\partial t}(\lambda) W(t-\lambda) d\lambda \quad (2.17)$$

where $W(t-\lambda) > 0$ is a known weighting function, which has its maximum value at $\lambda = t$ and reduces monotonically as $(t-\lambda) > 0$ increases. As proposed in [104], Eq. (2.17) can be approximated as

$$\begin{cases} \tau_{un,w} = \frac{4\rho\nu}{D} \sum_{k=1}^{10} z_k(t) \\ z_k(t) = M_k[u(t) - u(t-\Delta t)]e^{-\frac{N_k}{2}\Delta t^+} + z_k(t-\Delta t)e^{-N_k\Delta t^+} \end{cases} \quad (2.18)$$

In the formula Δt is the computational mesh time step, M_k and N_k are vectors of constant values available in [104], and $t^+ = 4\nu t/d^2$ is the dimensionless time. Meanwhile, Δt^+ corresponds to the identical dimensionless value for Δt .

2.3.2 Chamber, restriction and Helmholtz resonator

The mass conservation equation can be applied to the chambers C_j ($j=1-4$ in Fig. 2.5) and writes

$$G_{in,j} - G_{out,j} = \frac{d\rho_j}{dt} V_j \quad (2.19)$$

in which $G_{in,j}$ and $G_{out,j}$ represent the total mass flow-rates entering and leaving the chamber C_j . V_j and ρ_j respectively stand for the chamber volume and the inside fluid density.

As a chamber is linked to a duct inlet, the chamber pressure is applied as the stagnation pressure to this boundary node in the pipe. On the contrary, as the pipe outlet is connected to a chamber, the pressure at the boundary node of the duct should be equal to the chamber pressure. With respect to the pipe L_3 , $\partial u/\partial x = 0$ is applied as the incompressible flow, and the density is selected to approximate ρ_3 in chamber C_3 . The momentum balance equation is reduced

to

$$\frac{\partial u}{\partial t} - \frac{1}{\rho_3} \cdot \frac{\partial p}{\partial x} = -\frac{4\tau_w}{\rho_3 D_3} \quad (2.20)$$

Eq. (2.20) is then multiplied by $\rho_3 A_3$ ($A_3 = \pi D_3^2/4$), and integrated over the length l_3 of the pipe L_3 and dividing by the same length l_3 . The results write

$$\frac{dG_{L3}}{dt} + \frac{A_3}{l_3}(p_4 - p_3) = -\pi D_3 \bar{\tau}_w \quad (2.21)$$

where G_{L3} is equal to $G_{in,4}$, which is the space averaged fluid mass flow-rate along L_3 . Since L_3 is included by the Helmholtz resonator, no significant flow-rate can be found. Therefore, the flow is treated as pure laminar and the average friction factor \bar{f} is calculated as following

$$\bar{f} = \frac{64}{Re} = \frac{64\nu\rho_3 A_3}{G_{L3} D_3} \quad (2.22)$$

in which $\nu \approx \nu_3$, and the space-averaged wall shear stress along L_3 is thus modelled through Eq. (2.13) and writes

$$\bar{\tau}_w = \frac{\bar{f}}{8\rho_3 A_3^2} |G_{L3}| G_{L3} = \frac{32\nu_3}{\pi D_3^3} G_{L3} \quad (2.23)$$

Therefore, substituting Eq. (2.23) into Eq. (2.21), the latter equation is rewritten

$$\frac{l_3}{A_3} \cdot \frac{dG_{L3}}{dt} + \frac{128\nu_3 l_3}{\pi D_3^4} G_{L3} + (p_4 - p_3) = 0 \quad (2.24)$$

Knowing $c^2 = dp_j/d\rho_j$ under the isothermal assumption, Eq. (2.19) can be modified and is then combined with Eq. (2.24). The result is further differentiated with respect to time, and a second-order ordinary differential equation in regard to p_4 is finally obtained [105].

$$\frac{d^2 p_4}{dt^2} + \frac{8\pi\nu_3}{A_3} \cdot \frac{dp_4}{dt} + \frac{A_3 c^2}{V_4 l_3} p_4 = \frac{A_3 c^2 p_3}{V_4 l_3} \quad (2.25)$$

According to Torricelli's formula for a flow under quasi-steady condition, the mass flow-rate going through the damper R_1 can be derived

$$|G_{out,1}| = C \cdot A_R \sqrt{2\rho_1 |\Delta p|} \quad (2.26)$$

where $G_{out,1}$ and ρ_1 stand for the mass flow-rate leaving the chamber C_1 and the oil density in the same chamber. C , A_R and $|\Delta p|$ are respectively the flow coefficient, the flow area at the damper R_1 and the modulus of the pressure difference between the two sides of R_1 . Meanwhile, at each instant, the effective flow-rate direction points to the side featuring a lower fluid pressure, and the positive direction is from C_1 to L_1 (cf. Fig 2.5).

2.3.3 Numerical algorithm

Since the flow within the instrument is definitely subsonic, no shock can be formed, and all fluid states should be continuous and fluent. Therefore, a finite-difference upwind numerical scheme, which is not conservative, has been employed to discretize the hyperbolic partial differential equations reported in Eq. (2.9)-(2.12). The formula writes

$$\begin{cases} w_{1,i}^{n+1} = w_{1,i}^n - \frac{\Delta t}{\Delta x} (u_i^n + c_i^n) (w_{1,i}^n - w_{1,i-1}^n) + \Delta t \cdot H_{1,i}^n \\ w_{2,i}^{n+1} = w_{1,i}^n - \frac{\Delta t}{\Delta x} (u_i^n - c_i^n) (w_{1,i+1}^n - w_{1,i}^n) + \Delta t \cdot H_{2,i}^n \end{cases} \quad (2.27)$$

where $w_{r,i}^{n+1}$ represents the unknown characteristic variable ($r = 1$ or 2) at the space coordinate x_i and at the time instant t_{n+1} (the identical conventions hold as well for other variables). As Eq. (2.11) is applied afterwards, the variables p and u can be subsequently derived from w_1 and w_2 .

Since no significant change of the fluid velocity occurs in the model, the time step can be initially fixed. According to Von Neumann stability analysis [106], the numerical scheme is stable if the Courant-Friedrichs-Lewy condition is fulfilled [107]. Therefore, the maximum Courant number is controlled at the values close to 0.9, and it is varied with a change in the time instant during the simulation.

At the computational nodes where the pipe conjunctions are present, instead of Eq. (2.27), implicit upwind one-step schemes are applied. This treatment of the boundary conditions of the sub models guarantees a higher coupling of Eq. (2.27) with the chamber flow equations, and the numerical oscillation is thus reduced. In addition, the implicit scheme is solved by applying the Newton-Raphson method at each time step.

2.4 Results and discussion

The validation figures of the EVI model is reported in Fig. 2.6. The comparisons between the time history of the EVI experimental pressure and of the pressure (p_4) obtained from the numerical model are present in terms of nominal pressure (p_{nom}) in the rail and energizing time (ET) of the current to the injector. Treating a reference time as t_0 , $t - t_0$ is a relative time and is shown as the abscissa of the diagrams. The vertical axis is the fluid pressure amount differed from 4 MPa. The input HDA mass flow-rate is synchronized with the EVI experimental data by converging their electrical current signals along the time axis.

Generally, a satisfactory agreement between the numerical and the experimental data is present in Fig. 2.6 and occurs for other working points (not demonstrated for the reason of conciseness), although minor discrepancies can be observed in the tail of the injection rates in Fig. 2.6c, which can be due to the residue pressure waves triggered in previous engine cycles. Therefore, the numerical model is capable to catch the vital characteristics of the physical system with a desirable accuracy.

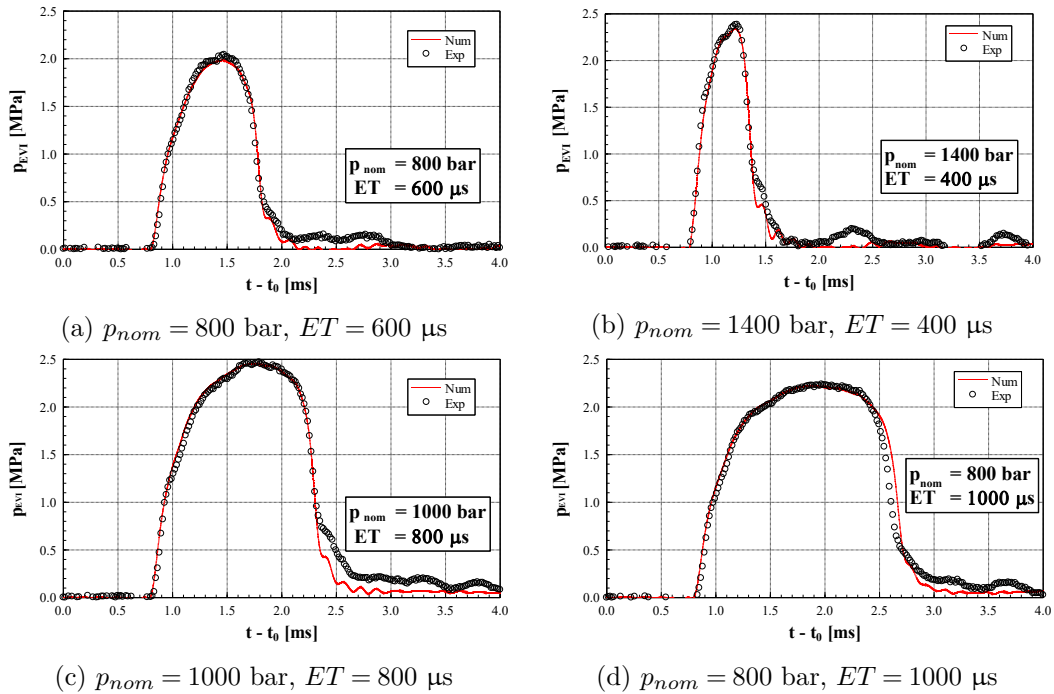


Figure 2.6: Experimental and numerical pressure of the EVI instrument.

Since the model produces a mass flow-rate signal that matches the experimental one of the EVI at the exact position of the pressure sensor in the Bosch setup, the assumption that the Zeuch method based flowmeter, that is, the HDA in the present case, provides the real injected mass flow-rate is validated. In other words, if the HDA mass flow-rate is provided as a boundary condition to the EVI model, the EVI flow-rate at the right location of its measurement is accurately predicted and this proves that the assigned boundary condition effectively is the real injected flow-rate.

Meanwhile, the experimental mass flow-rates of the EVI and of the HDA pertaining to the same working conditions of Fig. 2.6 are exhibited in Fig. 2.7. The ordinate reported is normalized into a ratio between the effective one and a reference one.

Some evident variation between the two curves can be observed in Fig. 2.7. The EVI flow-rates gives a time delay of around $50 \mu\text{s}$ to those of the HDA, worsening the detection of the *SOI*. A slight reduction of the flow-rate slope appears in the increasing phase of the EVI data. Moreover, although a finite-impulse-response (FIR) filter with a cut-off frequency of 6 kHz has been applied to the HDA signal, oscillations remain at the tops of the HDA

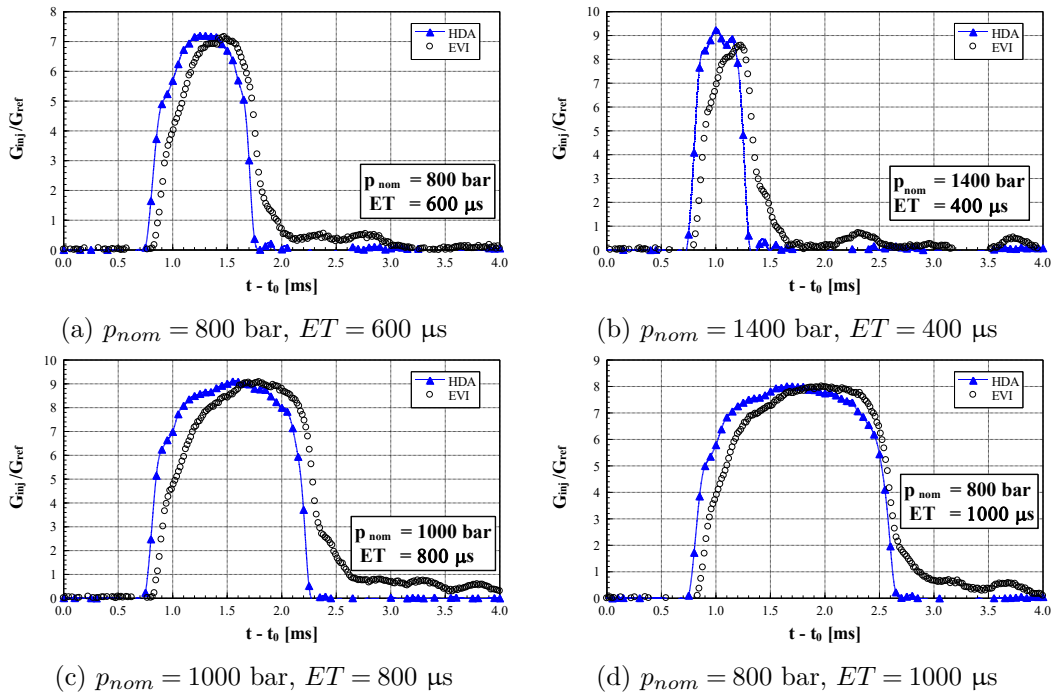


Figure 2.7: HDA and EVI experimental mass flow-rates.

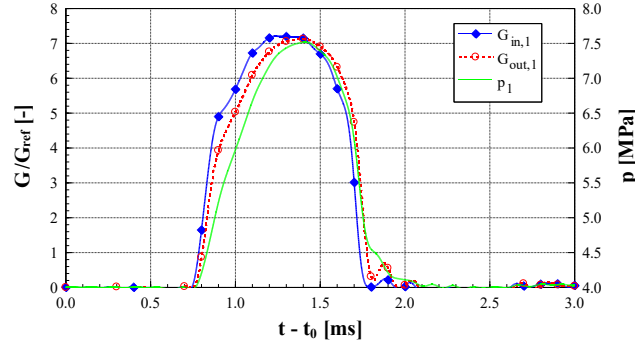


Figure 2.8: The input and the output mass flow-rates and the internal pressure of the chamber C_1 (model results).

flow-rates, while EVI flow-rate time history is fluent all time long. Above all, an abnormal tail is present at the end of each injection, which is evidently unphysical.

In short, both the reduction of the slope and the unphysical tail can be generalized as a “moving average effect”, which retards the dynamic response of the EVI device. In the meantime, the time delay of the flow-rate is another proof of this assumption.

The numerical tests reported in Figs. 2.8-2.18 are all performed under the working condition of $p_{nom} = 800$ bar and $ET = 600$ μ s. Whereas the results and the conclusions can be as well generalized to other conditions.

Fig. 2.8 reports the time histories of the numerical dimensionless EVI mass flow-rates ($G_{in,1}$ and $G_{out,1}$) entering and leaving the chamber C_1 (cf. Fig. 2.5), and of the C_1 inside pressure. Meanwhile, $G_{in,1}$ is also the HDA experimental data applied as the boundary condition of this model. It can be found that the increasing phases in both the flow-rates $G_{in,1}$ and $G_{out,1}$ at the start of the injection virtually take place at the same time instant. Whereas, pronounced differences between the same traces can be observed at the rest parts. In addition, a small tail starts to appear at the ends of both p_1 and $G_{out,1}$. This is due to that $G_{out,1}$ is determined by the pressure difference between the two sides of the restrictor R_1 . The pressure upstream and downstream of R_1 are p_1 and p_{L1} . Meanwhile, the pressure upstream (p_1) and the downstream ($p_{do,R1} = p_{L1}$) of the damper R_1 are reported in Fig. 2.9. A distinct difference between the two curves can be observed. Obviously, a delay between the flow-rate $G_{in,1}$

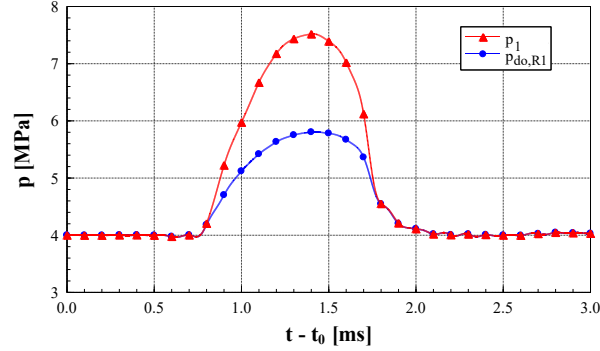


Figure 2.9: pressure upstream and downstream of the damper R_1 (model results).

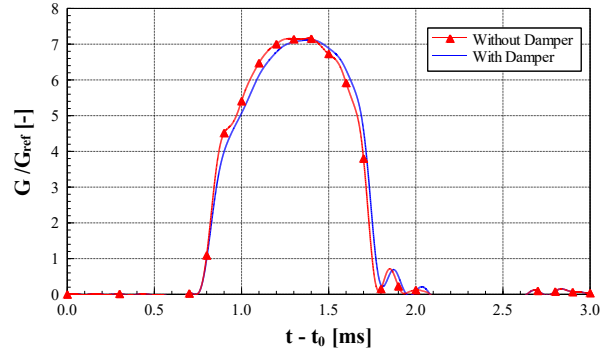


Figure 2.10: $p_{do,R1}$ for different installation conditions of the damper R_1 (model results).

and the pressure rise p_1 in the chamber exists due to the hydraulic capacitance of C_1 , and $G_{out,1}$ to some degree, keeps this delay through R_1 .

Fig. 2.10 exhibits the possible time history of $G_{out,1}$ if the damper R_1 is removed, and it is compared with itself when R_1 is present. It can be discovered that a slight moving average phenomenon arises with the presence of R_1 . It is in line with the phenomenon associated with an additional damping source that a smoothing and a small delay of the curve are demonstrated.

The parametric tests of the chamber inside pressures on the chamber volumes for C_1 and C_2 are reported in Figs. 2.11-2.12. The changes demonstrated in percentages are with respect to the baseline values. Generally, a reduction in the chamber size improves the dynamic response in the inside pressure, and vice versa, due to a slowdown effect caused by the hydraulic circuit inertia. Uniquely, with the chamber size of C_1 increased, an even more evident moving average effect can be observed. On the other hand, the oscillation found in p_1 pertaining to the -95% case is due to the analogous phenomenon in the

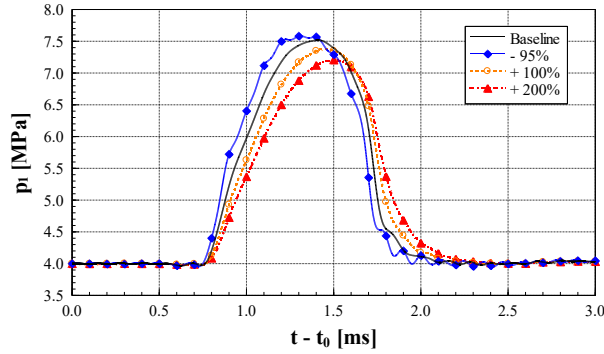


Figure 2.11: p_1 for different C_1 volumes (model results).

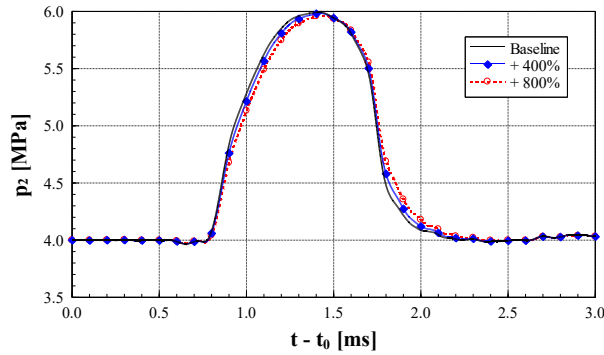


Figure 2.12: p_2 for different C_2 volumes (model results).

input mass flow-rate, which is acquired by means of the HDA. As regards to the chamber C_2 (cf. Figs. 2.12), since its original volume is small, no evident influence in p_2 can be found as the volume is modified.

As far as the convergent pipe L_1 's impact is concerned, similar to the investigating method with respect to the effect of the damper R_1 , L_1 has been replaced by a straight pipe featuring the same diameter of L_2 , and the comparison in the simulation results are reported in Fig. 2.13. No obvious differences can be found in the comparison between the mass flow-rate ($G_{in,2}$) pertaining to "Without Convergent Pipe" and to "With Convergent Pipe". Whereas, the peak value of the flow-rate $G_{in,2}$ in the modified model featuring only straight pipes is slightly smaller than the original one. This is a contrary phenomenon with respect to the moving average effect above mentioned.

Furthermore, Fig. 2.14 indicates that the pressure wave amplitude, utilized to evaluate the injection rate, rises as the flow area of the pipe L_1 decreases. Whereas, during the rising and reducing parts of the curves, the three curves

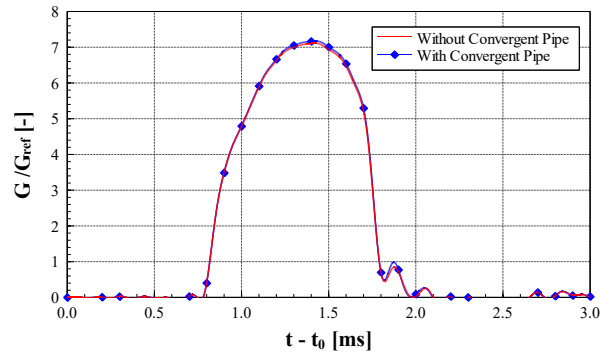


Figure 2.13: Mass flow-rates upstream of chamber C_2 in the presence and in the absence of the convergent pipe (model results).

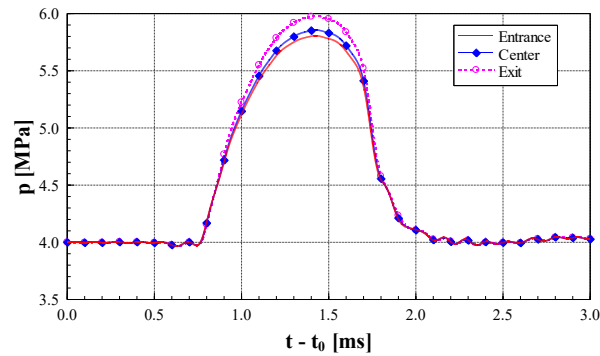


Figure 2.14: Time histories of the pressures at different sections of the convergent pipe L_1 (model results).

basically converge. This is another proof, in line with result of Fig. 2.13, that the convergent tube could counteract the phenomenon induced by both R_1 and R_1 . However, the difference, caused by the convergent tube, in the maximum value of the pressure signal is smaller than 15%, which is negligible compared with the pressure difference at the two sides of R_1 .

Fig. 2.15 demonstrates the time histories of the predicted EVI mass flow-rate G_{EVI} and of the mass flow-rate ($G_{in,3}$) that enters the junction C_3 . As well another evident moving average effect can be observed in G_{EVI} , since the prediction is on the basis of the pressure pattern (p_4) in C_4 . In short, the Helmholtz resonator, made up of C_3 , L_3 and C_4 , introduces a smoothening and a delay between the instrument output signal and the effective flow-rate passes by the key sensor.

In detail, in the Helmholtz resonator, the tube L_3 possesses a relatively large diameter. As a consequence, neither pronounced pressure differences nor

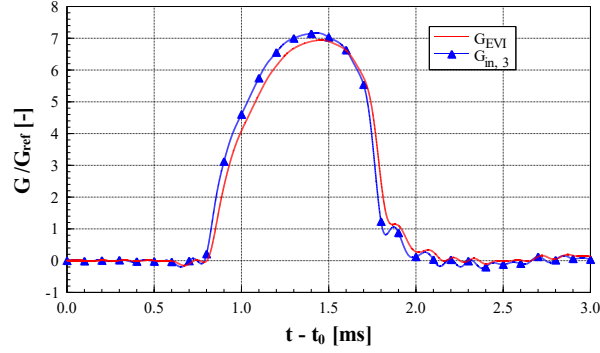


Figure 2.15: Estimated EVI injection rate and the mass flow-rate entering the junction C_3 (model results).

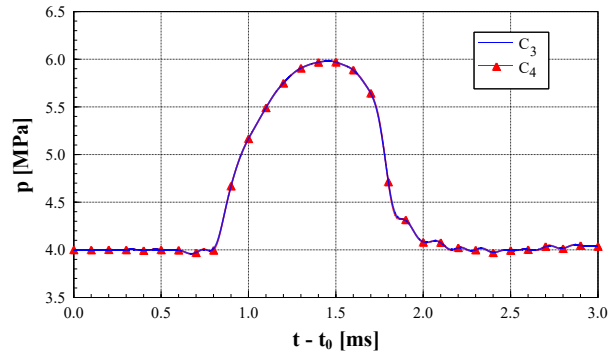


Figure 2.16: Pressure time history in C_3 and C_4 (model results).

high-frequency pressure oscillations can be found between the two chambers. Meanwhile, the pressures in C_3 and C_4 are generally unified (cf. 2.16). Therefore, it is the same effect as that two chambers are integrated into one volume, and the size of the new chamber is equal to the sum of V_3 and V_4 . In other words, the influence of Helmholtz resonator is not observed, but a result of appreciable inertia due to the hydraulic capacitance of the new chamber is distinct.

Fig. 2.17 reports the estimated EVI mass flow-rate G_{EVI} , the mass flow-rate $G_{out,3}$ that leaves the junction C_3 and the mass flow-rate G_{L2} , which is computed 30 mm downstream of C_3 . No evident difference is observed between those curves. The maximum value of G_{EVI} is around 3% smaller than that of the other curves due to the hydraulic inertia above elaborated. Meanwhile, a slight delay in G_{L2} is observed compared to $G_{out,3}$. This can be ascribed to the necessary time length, during which the pressure wave propagates. In short, the estimated injection rate G_{EVI} is capable to simulate the mass flow-rate

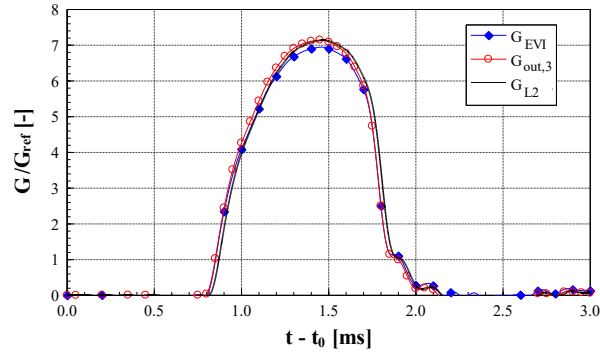


Figure 2.17: Predicted EVI mass flow-rate, mass flow-rate leaving C_3 and mass flow-rate downstream of C_3 (model results).

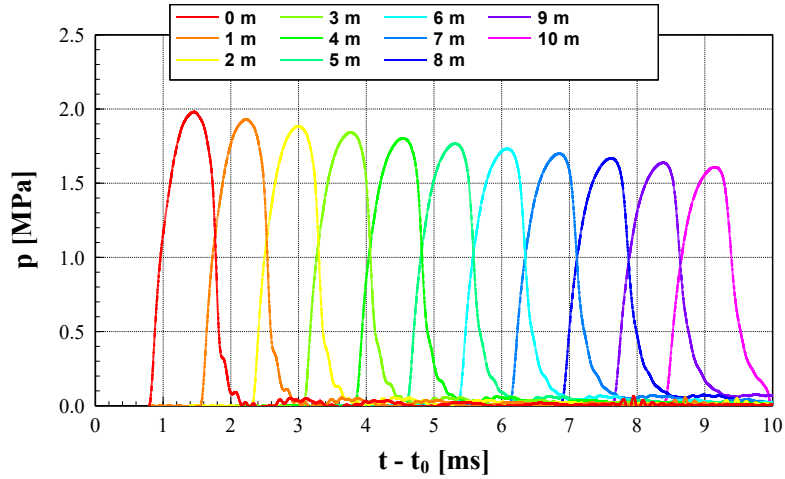


Figure 2.18: Pressure waves along the tube loop downstream of the Helmholtz resonator (model results).

along the tube L_2 downstream of C_3 , in line with the purpose of the instrument design.

With the help of the numerical model, the pressure time histories at different positions along the pipe L_2 downstream of the junction C_3 are shown in Fig. 2.18. The reported pressure signals have subtracted the static pressure of 40 bar initially set in the instrument. As can be found in Fig. 2.18, the pressure wave amplitude progressively reduces as the wave propagates along the duct. Especially, when the wave approaches the location of the residual pressure control valve (cf. item 9 in Fig. 2.1), the time delay of the wave even approximates 8 ms, and its maximum value reduces around 20%. The

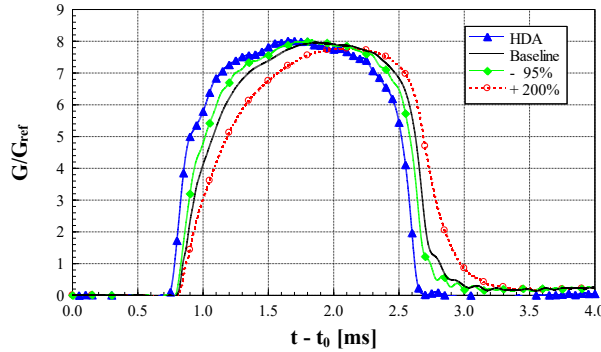


Figure 2.19: Time distribution of G_{EVI} for different C_1 volumes and HDA injection rate ($p_{nom} = 800$ bar, $ET = 1000$ μ s).

reasons are respectively the pressure wave transmission time and the viscous dissipation.

In consequence, if the pressure transducer, employed to catch the pressure wave triggered by the injection events, is far downstream of L_2 , unacceptable underestimation of the amplitude and huge delay would alter the output injection rate. In fact, p_{EVI} is measured at the transducer installed in C_4 , which is only approximately 4 cm downstream of the injector tip. Nonetheless, a short delay of 20 μ s, which should be considered when the nozzle opening delay (NOD) of an injector is accurately estimated, remains in the evaluated mass flow-rate.

Lastly, some results with respect to a large injection are reported in Fig. 2.19. The EVI predicted mass flow-rate (Baseline) is subjected to a delay and a moving average effect compared to the HDA output injection rate. As C_1 volume is reduced by 95%, the EVI signal tends to approach to the HDA evaluation. On the contrary, by enlarging the volume of C_1 by 200%, the smoothening originally occurring in the flow-rate rising part even extends to the stabilized injection phase. Particularly, the analogous phenomenon, seemed theoretically impossible, has been described in [19], when applying an EVI device: as a large injection is performed, the injection rate signal increases while the oil pressure in the high-pressure circuit reduces. Nevertheless, with reference to the above elaborated moving average effect, it is clear that during the stabilized injection phase the output injected mass flow-rate is smaller than its authentic value under the condition of an enlarged C_1 (+200%). In that case,

the mass flow-rate evaluated by means of the EVI firstly gradually approaches to the correct value, and the flow-rate reducing phase is then retarded.

Chapter 3

Injection system optimization

3.1 Experimental setup

The experimental campaign on the CR and the CF systems has been performed at the same hydraulic test rig with the identical calibration fluid mentioned in Sect. 2.1. The Zeuch method-based flowmeter HDA is employed to evaluate the injected flow-rate time histories. The KMM flowmeters are employed to continuously detect the injectors recirculated flow-rates. The electric current distributions are measured by means of a current clamp. Furthermore, piezoresistive pressure sensors have been mounted in the CR and the CF system to capture the pressure time history at the electro-injector inlet. Finally, the rail pressure in the CR system is evaluated by means of the pressure transducer of the same type, while due to the lack of installation space, the CF system rail pressure has not been captured. All the hydraulic experiments have been conducted at a fixed pump speed of 1000 rpm, corresponding to an engine speed of 2000 rpm for both Sects. 3.2 and 3.3. Since the pump speed does not alter any boundary conditions of the system, and since the pressure waves travelling in the high-pressure circuit can be enough damped as the time of one engine cycle passes by, the obtained conclusions can be generalized to any other engine speeds.

The KMM device, whose layout is reported in Fig. 3.1, is a positive-displacement type continuous flowmeter. In such a device, the fuel enters the flowmeter after passing through a heat exchanger. A damper (cf. item 1 in Fig. 3.1), installed at the inlet of the flowmeter, then reduces the pressure pulsations due to the injections. In addition, the KMM consists of a hydraulic

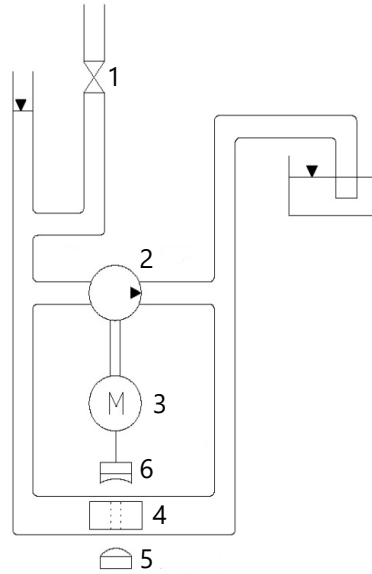


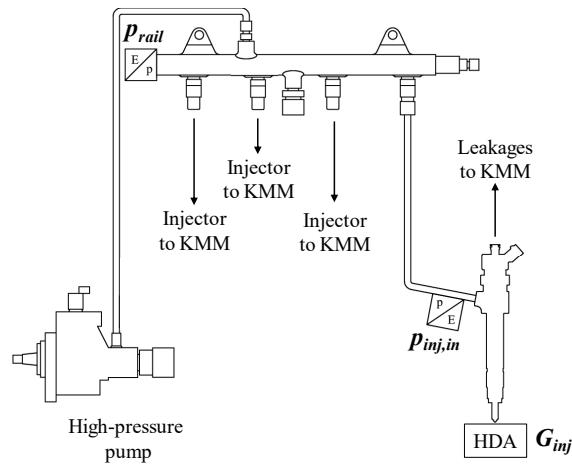
Figure 3.1: KMM flowmeter layout.

circuit featuring two piezometric pipes connected by means of two horizontal branches. Within the upper branch, a small displacement volumetric pump (cf. item 2 in Fig. 3.1), activated by means of an electric motor (cf. item 3 in Fig. 3.1), is located. Meanwhile, a floating piston is mounted at the lower branch. This piston features a hole, through which, in the condition of equilibrium, the light beam, given by means of the optical emitter (cf. item 5 in Fig. 3.1), is intercepted by a receiver (cf. item 6 in Fig. 3.1). This receiver then sends a drive signal to the motor. When fuel is discharged into the piezometric tube upstream of the pump, the hydraulic head of this duct increases. The floating piston thus shifts and obscures part of the light beam. In consequence, the receiver sends a signal to the motor to activate the pump with a speed proportional to the degree of dimming of the optical sensor. Until the pump restores the same elevation head in the two pipes, the piston returns to the equilibrium position, causing a decrease in the pump speed. Through the above elaborated method, the system retains the pressure within the two piezometric tubes the same. In result, the pump displacement value and the number of revolutions, which have been performed to balance the elevation head in the two ducts, can be correlated to the fuel flow-rate passing through the device. The KMM flowmeter is capable to accurately evaluate the flow-rate of a stable

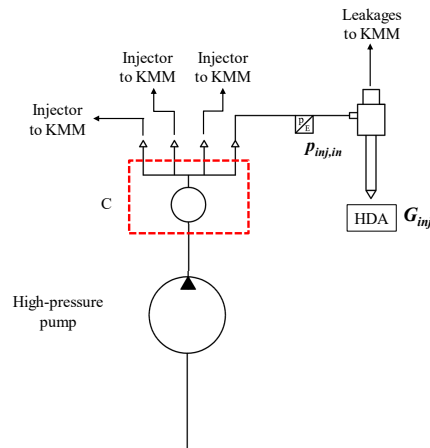
continuous flow. Whereas, it is not designed to characterize pulse-like injection rates.

3.2 Common-Feeding system

A CR system (cf. Fig. 3.2a) and a CF system (cf. Fig. 3.2b) that adopts the same high-pressure pump and the same injectors, produced by Nanyue Fuel Injection Systems Co., Ltd, have been tested. In order to match the operating conditions of a light duty commercial vehicle engine, the injector of this type is designed to stably inject from 0.5 mg to 60 mg of fuel per engine



(a) CR system



(b) CF system

Figure 3.2: The schematic of the high-pressure circuit of the CR and the CF systems.

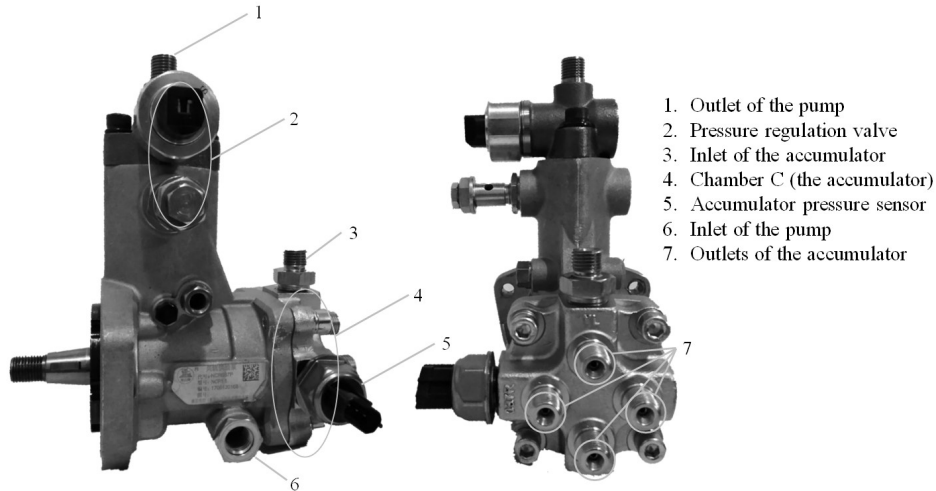


Figure 3.3: The high-pressure pump integrated with the accumulator.

cycle. As regards the CR system, the high-pressure pump is connected to the common rail, whose standard volume (V_{rail}) is 12.9 cm^3 . In order to evaluate the influence of the accumulator size in a light duty vehicle, a series of rail prototypes with $V_{rail} = 10 \text{ cm}^3$, 4.7 cm^3 and 2.1 cm^3 , manufactured by varying the internal cylinder diameter with the same length, has been realized. In the CF system [29], visible in Figs. 3.2b and 3.3, a chamber C with the internal volume $V_C = 10 \text{ cm}^3$ has been realized. The internal volume of the chamber features a cross shape. Three chamber prototypes with the same internal volume shape have been manufactured. Among those, two are equipped with an additional gauged orifices ($d_{or} = 1.2 \text{ mm}$ or $d_{or} = 1.6 \text{ mm}$). Such orifices have been manufactured at the connection ports to the injector supplying tubes, in order to damp the pressure waves transmitted along the high-pressure circuit. The original common rail pressure transducer (cf. item 5 in Fig. 3.3) has been mounted in chamber C to evaluate the internal pressure transients. By adopting this layout, a cost reduction and an easier engine installation can be achieved. In both the CR and the CF systems, a single cylinder double-acting hydraulic pump is employed. Furthermore, at the high-pressure side of the

pump, a solenoid valve (cf. item 2 in Fig. 3.3) is the only means to control the fuel pressure of the high-pressure circuit, by expelling the excess pumped fuel back to the tank [108]. Meanwhile, all the high-pressure connecting pipes feature a length $l = 300$ mm with a diameter $d = 2.7$ mm.

All the tests reported in this section were evaluated for the steady state working conditions referring to fixed p_{nom} and ET values as averages over 100 consecutive engine cycles.

Fig. 3.4 reports the time histories of the inlet pressure ($p_{inj,in}$), of the injected mass flow-rates (G_{inj}) and of the energizing currents for different rail volumes (V_{rail}) under two operating conditions ($p_{nom} = 1100$ bar, $ET = 220$ μ s and $p_{nom} = 1100$ bar, $ET = 800$ μ s). Particularly, $p_{inj,in}$ is a key parameter that affects the general pressure transients in the hydraulic high-pressure circuit, and the pressure oscillation could be greater as the measuring location is closer to the injector nozzle. Before the supply of the current signals (0 ms $< t - t_0 < 0.5$ ms), all the $p_{inj,in}$ pertaining to different V_{rail} values are quasi horizontal, that is, stabilized. Thus, ignorable influences are given to the subsequent injections. Nevertheless, minor fluctuations present in $p_{inj,in}$, due to that the pressure waves, triggered in the previous injection cycle, have been damped along the rail-to-injector pipe, where the pressure transducer is mounted. In addition, it is noteworthy that the pumping stroke is phased around the start of the energizing currents of the investigated injector.

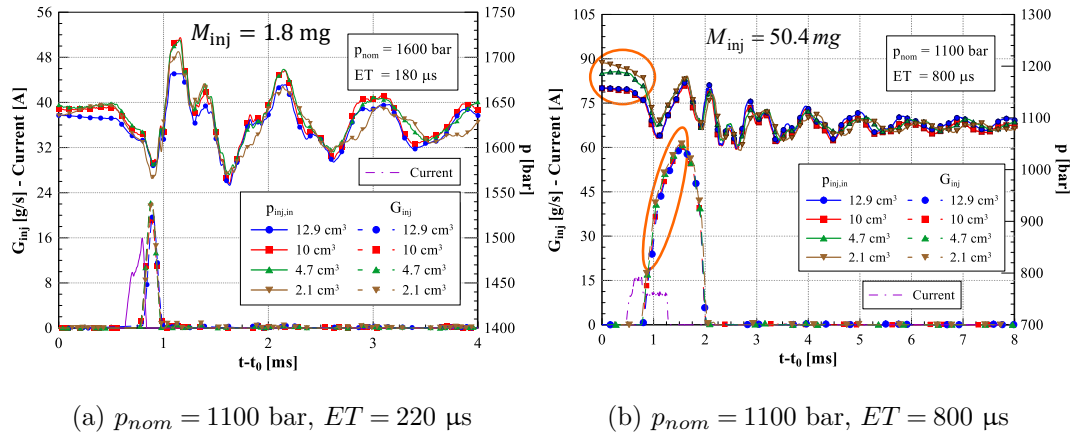


Figure 3.4: Comparison on the G_{inj} and the $p_{inj,in}$ between the CR systems with different rail volumes.

As regards a small injection ($M_{inj} = 1.8$ mg) reported in Fig. 3.4a, the $p_{inj,in}$ and the G_{inj} time distributions are analogous for all V_{rail} values during the entire time length ($0 \text{ ms} < t - t_0 < 4 \text{ ms}$) shown. Thus, it can be inferred that the change in V_{rail} has a minor effect on the performance of small injections.

On the contrary, when a large injected quantity ($M_{inj} = 50.4$ mg and cf. Fig. 3.4b) is considered, the initial $p_{inj,in}$ level, circled in Fig. 3.4b, appears to rise as the accumulator volume reduces. Such a phenomenon can accelerate the lifting up process of the needle during the nozzle opening phase with a smaller accumulator. Furthermore, a slightly higher instantaneous value, circled part of G_{inj} in Fig. 3.4b, is present in the injected flow-rate rising phase, and in turn the total injected quantity is altered when a fixed electrical command is supplied. On the other hand, independently of V_{rail} , a depression wave arises immediately when the nozzle starts to inject, and it travels along the hydraulic pipeline from the injector nozzle to the common rail. During this process, the wave arrives at the pressure sensor location where $p_{inj,in}$ is measured at $t - t_0 \approx 0.8$ ms. As a result of the depression wave, the fuel that reaches the nozzle from the injector feeding pipe is restricted by the passage between the needle and the seat in the injector body. A compression pressure wave is thus generated at $t - t_0 \approx 1$ ms. Meanwhile, the above mentioned depression wave reaches the common rail and is reflected as a compression wave, propagating towards the injector nozzle.

As mass conservation equation is applied to the common rail volume, it is approximately obtained:

$$\frac{V_{acc}}{c^2} \cdot \frac{dp_{acc}}{dt} = G_{pump} - G_{inj} - G_{leak} \quad (3.1)$$

in which V_{acc} is the accumulator (common rail in this case) volume, p_{acc} is the mean fuel pressure inside of the accumulator, and G_{pump} , G_{inj} and G_{leak} are respectively the fuel pumped, injected and leaked mass flow-rates with respect to the high-pressure circuit. Integrating Eq. (3.1) over an engine cycle (T_{inj}), the formula writes

$$\frac{V_{acc}}{a^2} \cdot \int_{t_0}^{t_0+T_{inj}} \frac{dp_{acc}}{dt} = M_{pump} - M_{inj} - M_{leak} \quad (3.2)$$

where t_0 is a reference time instant. Since a similar amount of fuel mass ($M_{inj} + M_{leak}$), which is independent of V_{rail} , is expelled from the injector

within one engine cycle, and since the pumped fuel amount (M_{pump}) is as well approximately the identical, $p_{inj,in}$ curves of the reduced V_{rail} values initialize with higher levels. This is purposely controlled by the ECU to converge the rail pressure time average value to the preset nominal value. The differences in $p_{inj,in}$ between varied V_{rail} diminish as the injection is being performed. In fact, in Fig. 3.4b from $t - t_0 \approx 1.6$ ms on, the $p_{inj,in}$ profiles turn to be basically overlapped. At the time instant $t - t_0 \approx 2$ ms, which is around the *EOI*, the nozzle is closed, and a water hammer and the subsequent oscillations can be observed in $p_{inj,in}$.

With respect to another operating condition ($M_{inj} = 61.4$ mg), Fig. 3.5 demonstrates the identical variables as Fig. 3.4. The performance of the CF configuration, whose internal volume $V_C = 10$ cm³ (without the gauged orifices), is presented by means of the orange curves. The $p_{inj,in}$ initial value pertaining to the CF system is between that of the two CR systems with different V_{rail} . In turn, the rising part of the G_{inj} is as well between those of the CR configurations. This phenomenon confirms that the above mentioned characteristics are determined by the V_{acc} .

It can be observed from Fig. 3.5 that the amplitudes and the frequencies of the free pressure waves that take place after the hydraulic injection events are influenced by the V_{rail} . Nevertheless, even though the CF configuration features $V_C = 10$ cm³, the natural frequency of its pressure wave is approximately 30% smaller than those of the CR layouts., which feature $V_{rail} = 12.9$ cm³ and

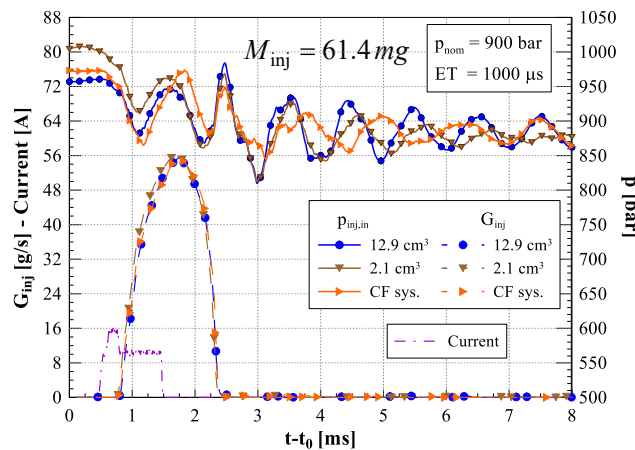


Figure 3.5: Comparison on the G_{inj} and the $p_{inj,in}$ between the CR and the CF systems.

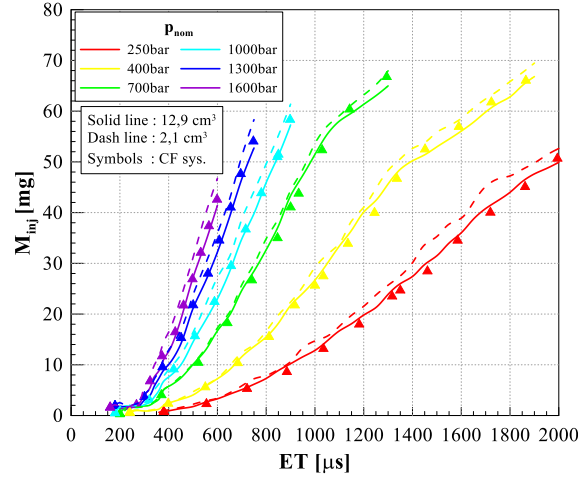


Figure 3.6: Comparison on the M_{inj} between the CR ($V_{rail} = 12.9 \text{ cm}^3$ and 2.1 cm^3) and the CF (without gauged orifices) systems.

$V_{rail} = 2.1 \text{ cm}^3$. Such a phenomenon is probably ascribed to the change in the accumulator shape.

The injector characteristics of the CR and the CF systems are reported in Fig. 3.6. The results pertain to the CR systems featuring V_{rail} of two extreme values and the CF system without the gauged orifices. The CR system with the minimum V_{rail} features the maximum slope upon the $M_{inj} - ET$ curve and the greatest difference in M_{inj} between the two CR systems is approximately 5.5 mg. The CF system characteristics are analogous to those of the standard CR ($V_{rail} = 12.9 \text{ cm}^3$) system, since the CF system features a similar accumulator size ($V_C = 10 \text{ cm}^3$). Therefore, it is reasonable to confirm that the characteristics slope reduces as the size of the accumulator increases and is virtually independent of the accumulator shape. In addition, this trend is as well in line with the change in the $p_{inj,in}$ initial value as the accumulator volume is modified (cf. Fig. 3.4b).

The static leakage measures the fuel amount discharged from one injector to the recirculation pipe as the pilot valve is closed over one engine cycle and under steady state. The measurement is carried out by maintaining the high-pressure circuit of the system at a preset p_{nom} value while no injection is being performed. Fig. 3.7a reports the static leakages per engine cycle for the CR systems. When the $p_{nom} > 1200 \text{ bar}$, it can be observed that an evident trend, in which the leakage reduces as the V_{rail} decreases. Generally, the stationary volumetric flow-rate following the Hagen-Poiseuille expression

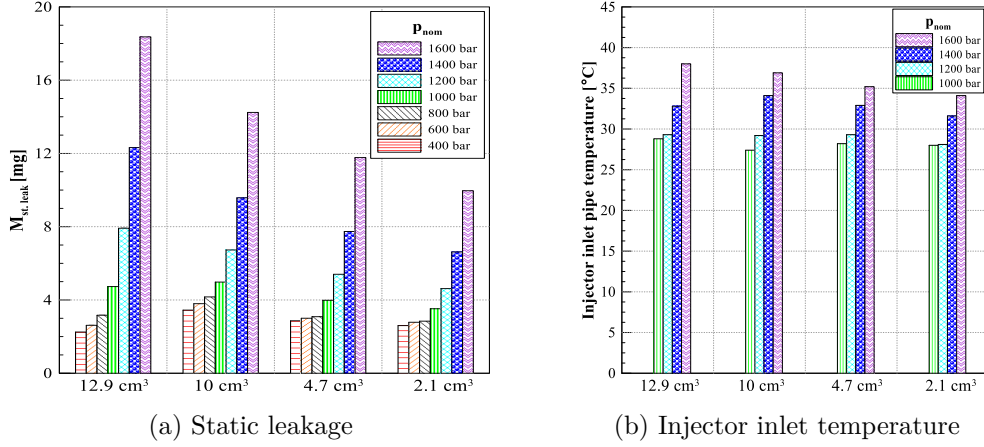


Figure 3.7: Comparison on the $M_{st,leak}$ and the $T_{inj,in}$ between the CR systems with varied V_{rail} .

can be applied to analyze static leakages. One thus writes

$$Q_{leak} = K \frac{\bar{p}}{\bar{\mu}} \quad (3.3)$$

in which K stands for a geometrical coefficient determined by the pilot valve layout and by the other possible passages. $\bar{\mu}$ is the mean oil dynamic viscosity, which is a function of the average values of the p and the T in the injector, namely, \bar{p} and \bar{T} . The variable \bar{p} retains generally identical in different V_{rail} as the p_{nom} is fixed by the ECU, while the $T_{inj,in}$, captured at the injector inlet on the feeding pipe and shown in Fig. 3.7b, demonstrates an analogous trend with respect to V_{rail} as that of $M_{st,leak}$. Since $\bar{\mu}$ is sensitive to the variable \bar{T} , the differences in the static leakage could be ascribed to a thermal influence.

The dynamic leakage, calculated by subtracting the static leakage from the total leakage in one engine cycle, provides the leaked fuel quantity going through the pilot valve as the solenoid in the injector is being energized. Such quantities are demonstrated in Fig. 3.8. As ET rises, since the pilot valve opening time length increases, it is pronounced that the dynamic leakage augments. Moreover, higher the p_{nom} , greater the $M_{dyn,leak}$, while no evident trend in $M_{dyn,leak}$ can be found with respect to V_{rail} .

As regards all possible operating conditions of the CR systems over 100 consecutive engine cycles, the coefficients of variation in the injected mass, measured by means of the HDA, are reported in Fig. 3.9. An injection pattern, which can be applied to a production engine, should possess a cycle-to-cycle

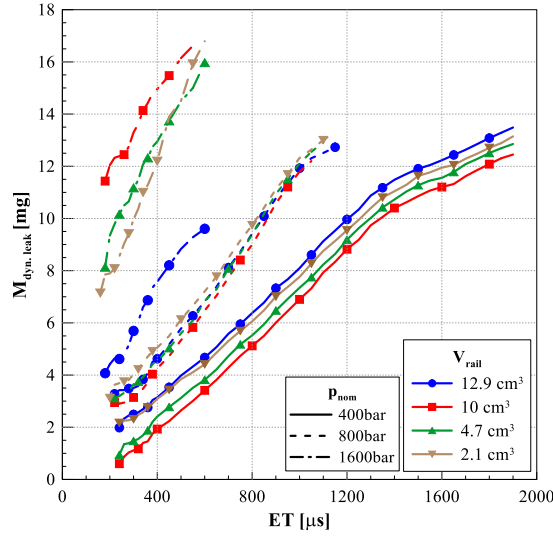


Figure 3.8: Comparison on the $M_{dyn,leak}$ between the CR systems with varied V_{rail} .

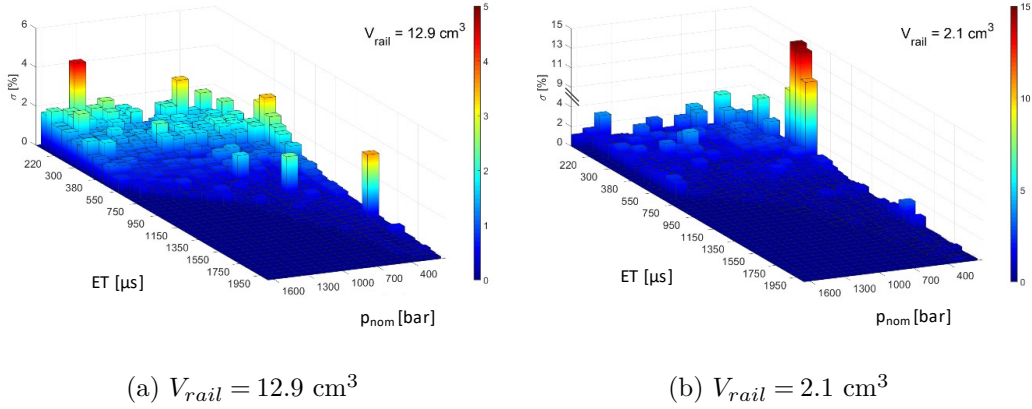
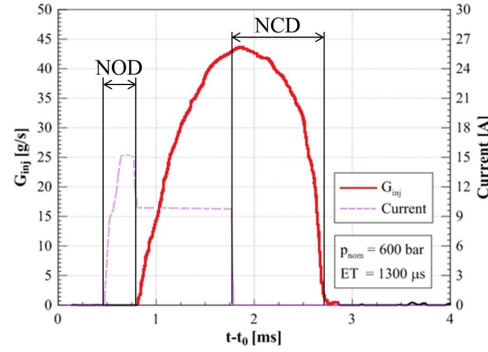
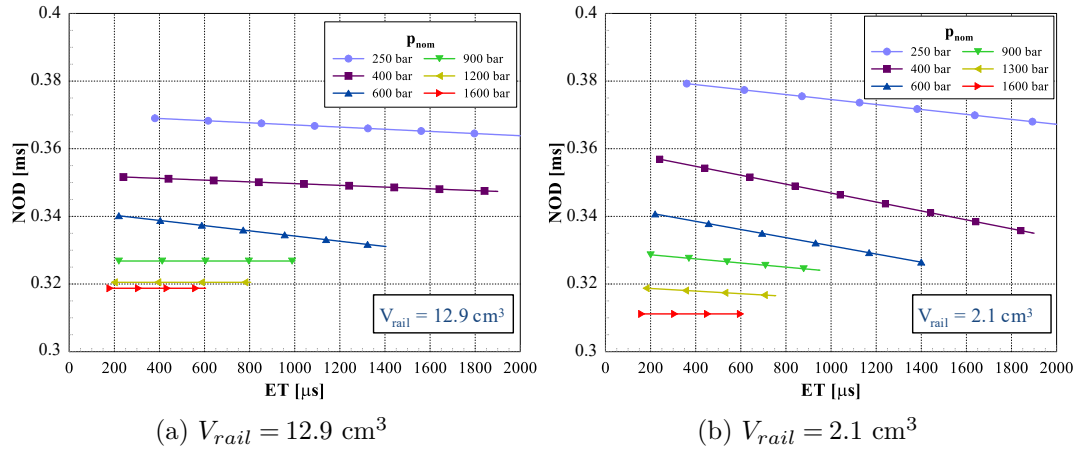


Figure 3.9: Comparison on the σ between the CR systems with different V_{rail} .

variation smaller than 10% [29]. All the tested operating points fulfill such criterion, except a few under $p_{nom} = 250$ bar and small ET in Fig. 3.9b. Higher coefficients of variation take place at either small p_{nom} or reduced ET values. Meanwhile, the σ decreases sharply as the ET rises. On the other hand, it is obvious that as the V_{rail} reduces, the cycle-to-cycle dispersion worsens in the operating zone of Fig. 3.9. The data of the CR system with $V_{rail} = 10 \text{ cm}^3$ and 4.7 cm^3 follow the identical trend, while are not presented for the sake of conciseness.

Figure 3.10: Definitions of *NOD* and *NCD*.Figure 3.11: *NOD* of the CR systems with different V_{rail} .

The nozzle opening delay (*NOD*), defined as the time interval between the start of the energizing current and the effective hydraulic *SOI*, is reported in Fig. 3.10. The smaller the *NOD*, the better the injector dynamic response. The *NOD* pertaining to the CR systems with $V_{rail} = 12.9 \text{ cm}^3$ and 2.1 cm^3 are respectively reported in Figs. 3.11a and 3.11b. For each layout, the data under the working conditions of one p_{nom} value have been fitted by means of a straight line. While in fact, it is merely a slight change between the original data and the fitted ones. As a whole, the *NOD* augments as the p_{nom} diminishes, since the higher pressure leads to a greater dynamic leakage flow-rate through the pilot valve, and the smaller time length is needed to empty the control chamber [109].

The nozzle closure delay (*NCD*), which evaluates the time interval needed by the needle to close the nozzle as soon as the electric current, has been shut

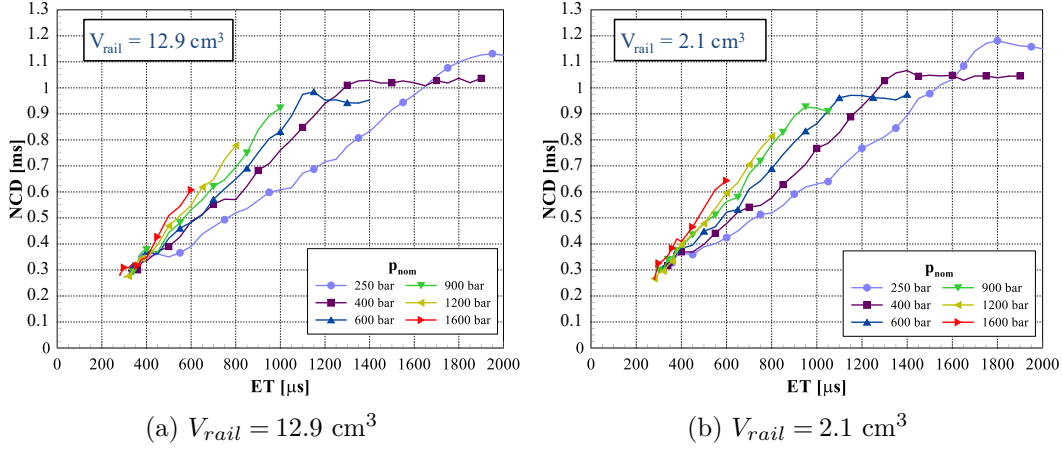
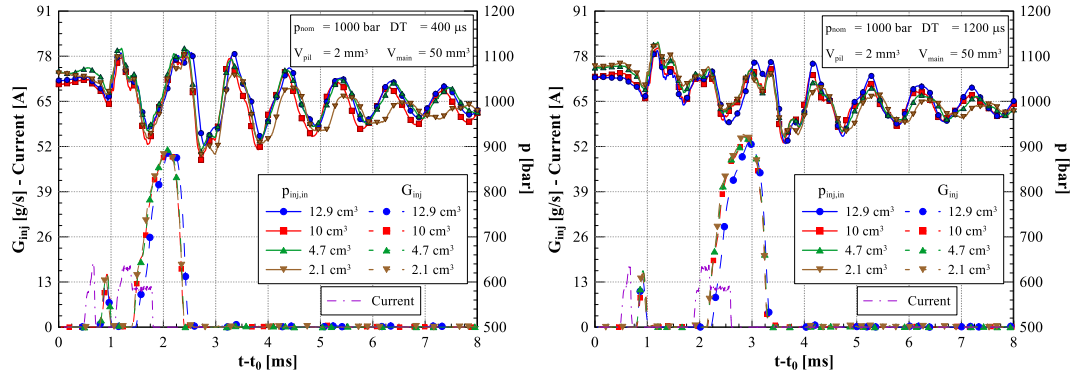


Figure 3.12: NCD of the CR systems with different V_{rail} .

down, is exhibited in Fig. 3.12. Similarly, this variable is not influenced by the V_{rail} . NCD rises as ET increases, and the $NCD - ET$ curves under greater p_{nom} values feature greater slopes. If ET is enough long to allow the needle reaching the upper stroke end, the NCD remains constant as the ET further augments [109]. Since higher p_{nom} provides a faster dynamic response, the maximum NCD occurs at reduced p_{nom} values.

Fig. 3.13 demonstrates the same variables as Fig. 3.4 for pilot-main injections. With respect to each V_{rail} , the ET s of both the pilot and the main injections have been determined to achieve the identical injected volumes when DT is fixed at 3000 μ s, where the pressure waves triggered by the pilot injection do not strongly affect the consecutive main injection. Since the energizing currents pertaining to different V_{rail} are analogous, only one current time distribution is reported. The instantaneous pressure signals are similar between different V_{rail} . Thus, the hydraulic events are affected by the pressure dynamics in an analogous way.

As the injections are about to start, the $p_{inj,in}$ for all V_{rail} values are generally horizontal. A depression wave is triggered by the pilot injection, and immediately a compression wave follows as above explained. Since pilot injection lasts for quite short time length, as soon as the needle returns to its seat, the water hammer is formed, and the induced pressure wave as well transmits along the rail-to-injector pipe. The amplitude of this wave observed at the injector inlet can be up to 200 bar with a frequency of 1 kHz. As reported in Fig. 3.13a, the main injection starts when a depression wave arrives at the



(a) $p_{nom} = 1000$ bar, $V_{pil} = 2$ mm³,
 $V_{main} = 50$ mm³ and $DT = 400$ μs

(b) $p_{nom} = 1000$ bar, $V_{pil} = 2$ mm³,
 $V_{main} = 50$ mm³ and $DT = 800$ μs

Figure 3.13: Comparison on the G_{inj} and the $p_{inj,in}$ between the CR systems with different V_{rail} for pilot-main injections.

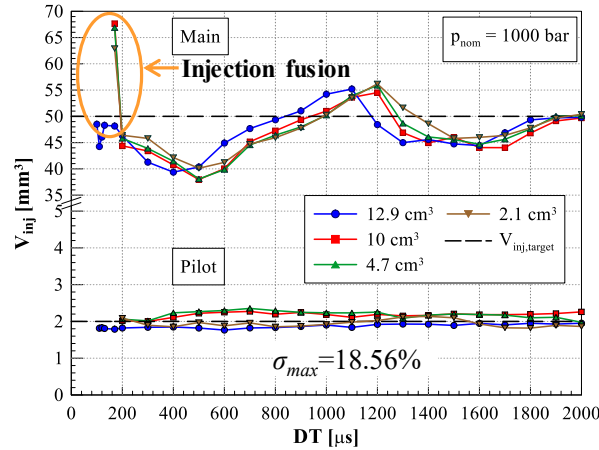


Figure 3.14: Comparison on the V_{inj} between the CR systems for pilot-main injections ($p_{nom} = 1000$ bar).

nozzle. While in Fig. 3.13b, with the supplied ET s respectively the identical as those in Fig. 3.13a for different V_{rail} , the main injection is in phase with a compression wave.

The needle lift pertaining to the main injection is possibly significantly influenced by the pressure internal oil pressure, and the effective injection duration is thus modified [110]. In fact, the injection duration reported in Fig. 3.13b are longer than those in 3.13a. Consequently, the injected quantities in Fig. 3.13b are generally greater. Such a phenomenon can as well be observed in Fig. 3.14, in which the V_{inj} of the pilot (lower curves) and the main (upper

curves) injections with respect to DT in the range between 100 μs and 2000 μs are reported. When DT is below a specific injection fusion threshold (IFT), the two injections merge, and the flowmeter is only capable to measure a unique injection event. Therefore, sharp increases in the main injected quantities are present below certain DT s, while no corresponding pilot injection values are reported.

As the values of DT are greater than the IFT , the pilot injected volumes ($V_{inj,pil}$) are generally the same, while the variation in the main injected volumes ($V_{inj,main}$) can be expressed as

$$\sigma = \left| \frac{V_{main}(DT) - \bar{V}_{main}}{\bar{V}_{main}} \right| \quad (3.4)$$

in which $V_{main}(DT)$ stands for the main injected volume under a specific DT , and \bar{V}_{main} is the mean main injected volume acquired over the entire DT range. As is shown in Fig. 3.14, the σ reaches up to approximately 20% as DT provides small values. In addition, the $V_{inj,main} - DT$ curves fluctuate with an identical frequency as that of the free pressure waves reported in Fig. 3.13. This confirms that the $V_{inj,main}$ is affected by the pressure waves induced by the pilot injections and propagating along the rail-to-injector pipe.

Fig. 3.15 exhibits the $V_{inj,main} - DT$ curves for the CF systems. The identical operating conditions have been implemented as those in Fig. 3.14. It

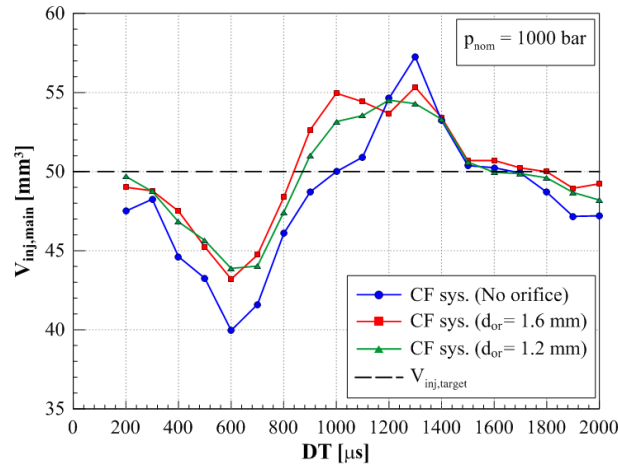


Figure 3.15: Comparison on the V_{inj} fluctuations with DT between the CF systems for pilot-main injections ($p_{nom} = 1000\text{bar}$).

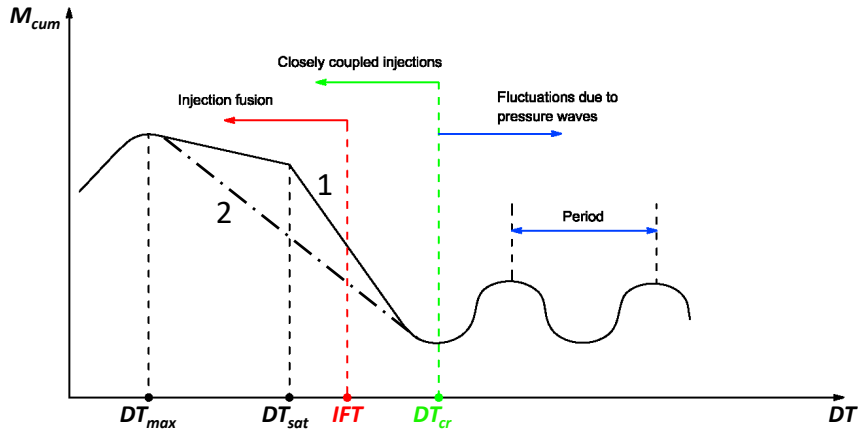
can be inferred that as the gauged orifices are installed at the pump delivery port in the CF system, the pressure waves in the high-pressure circuit are probably damped passively. Consequently, the amplitude of the oscillation in $V_{inj,main}$ is mitigated. As can be observed in Fig. 3.15, the fluctuation is more attenuated with a smaller d_{or} . Moreover, the tests, which have been carried out in a previous study, shows that the passive wave damping method, by means of gauged orifices, can reduce the injected volume up to 8% [110]. In result, the maximum injected flow-rate can be limited when the orifices are mounted in the CF system.

3.3 Injector setup

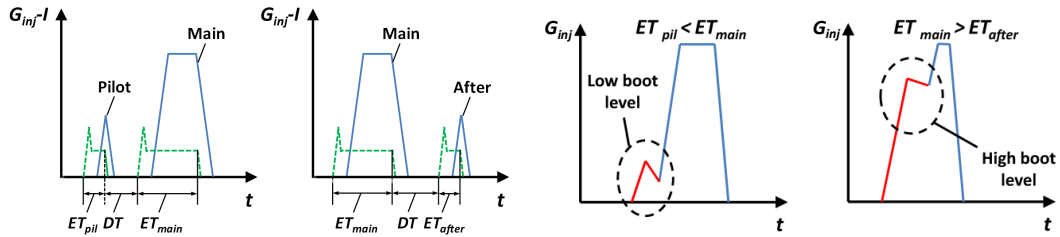
Two series of state-of-the-art injection systems, featuring respectively CRI 2.18 and CRI 2.20 solenoid injectors, have been tested. The pump applied to these two systems are identical, in order to compare their performance within the short DT range. In fact, the hydraulic layouts design of these two types of injectors feature vital differences.

3.3.1 Closely-coupled multiple injections

Fig. 3.16a schematically presents the injection regimes that can take place in double injections as the DT (cf. Fig 3.16b) is varied. Fig. 3.16b reports the patterns of the current I (dashed curve) and of the injected mass flow-rates G_{inj} (continuous curve) in pilot-main and main-after injections. In Fig. 3.16a, the solid curve marked with 1 refers to main-after injections, while the dashed-dotted curve marked with 2 stands for pilot-main injections. Outside the range of $DT_{max} < DT < DT_{cr}$, the solid curve is as well in force for pilot-main injections, whereas it is noteworthy that in fact, the DT_{cr} is different for diversified working conditions no matter they are pilot-main or main-after injections. If the DT is long enough, that is, in the field of the conventional DT for production engines ($DT > DT_{cr}$), fluctuations occur in the overall injected mass (M_{cum}), due to the oscillation of the second injected mass. The reason is that the pressure waves, triggered by the needle closure of the first injection, propagate forward and backward through the high-pressure circuit of the system and induce a modification of the effective injection time length of the second injection [109].



(a) Schematic of the $M_{cum} - DT$ curve



(b) Schematic of double injections

(c) Schematic of boot injections

Figure 3.16: Double injections realized by means of solenoid injectors.

The schematic of $M_{cum} - DT$ curves present an evident rising trend as the DT reduces into $DT < DT_{cr}$. The vital cause of such an anomalous increase in M_{cum} is that the interference between the injector internal hydraulic dynamics and the mechanical transients, triggered by the first shot, affecting the second injection [35]. In fact, if the first injection is closely-coupled to the second one ($DT < DT_{cr}$), the fuel pressure in the injector control chamber has not been restored when the energizing current pertaining to the second shot is switched on. The NOD of the second shot thus reduces compared with that

occurs in the range of $DT > DT_{cr}$. Meanwhile, a higher maximum needle lift can be reached as $DT < DT_{cr}$, if the needle valve of the injector is ballistic. Therefore, either M_{main} of the pilot-main injection or M_{after} of the main-after injection augments as DT reduces within the range of $DT_{max} < DT < DT_{cr}$. Such interference between the two injections culminates with injection fusion, which unites the two injected flow-rate time distributions. Since NCD generally exists to close the nozzle after the end of the electric current, even though the electrical commands pertaining to the two injections are separated, the needle cannot finish the stroke to reach its seat when the second upstroke phase starts.

The minimum electric DT value, with which two consecutive injection rate time histories remain distinct, is referred to as injection fusion threshold (IFT) [35]. In this study, three practical criteria have been applied to identify the IFT in Sect. 3.3.2. Digital rate-shaping techniques, referring to DT values slightly greater than the IFT , perform hydraulic shots within the range of closely-coupled injections. While injection fusion strategies ($DT < IFT$), can be adopted to realize continuous rate-shaping patterns (cf. Fig. 3.16c) by means of solenoid injectors. These injection patterns provide the possibilities that solenoid injectors are capable to achieve boot injections of the direct acting piezoelectric injectors. In addition, the initial injection rate level of the boot-like injections can be adjusted by modifying the ET of the first injection.

The primary difference between the solid curve marked with 1 and the dashed-dotted curve marked with 2 in Fig. 3.16a is a saturation like condition, which takes place in the main-after injection curve but disappears in the pilot-main injection one. This condition provides a minor variation in M_{cum} as DT reduces from DT_{sat} to DT_{max} . Within this DT range, the needle seat passage flow-area basically exceeds that pertaining to the nozzle holes, due to the high needle lift. Therefore, any modifications in the DT value merely give minor changes in M_{cum} [35].

3.3.2 IFT determination criteria

The original IFT determination criterion was developed on the flow-rate results obtained by means of Bosch method based flowmeters [109], such as the EVI device. The pilot-main injection ($p_{nom} = 1250$ bar, $ET_{pil} = 270$ μ s, $ET_{main} = 530$ μ s) and the main-after injection ($p_{nom} = 750$ bar, $ET_{main} = 670$ μ s, $ET_{after} = 310$ μ s) flow-rate time histories with different DT s, captured

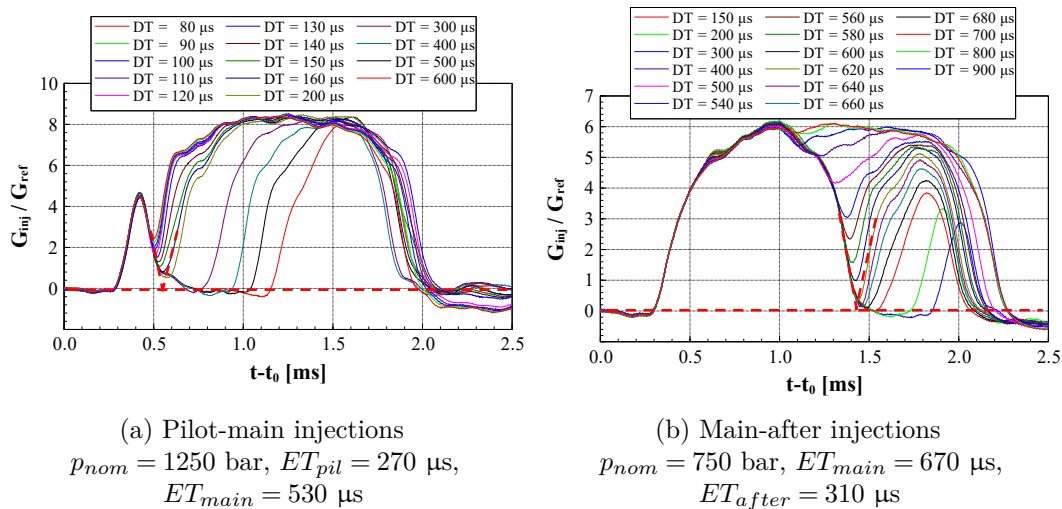


Figure 3.17: Injection flow-rates under different DT 's captured by EVI.

by the EVI device, are shown in Figs. 3.17a and 3.17b, respectively. Due to the working principle of Bosch method-based flowmeters, every single injection flow-rate time history ends with a tail, which has not any physical meaning [13]. IFT cannot therefore be easily determined by evaluating whether the flow-rate time histories that pertain to two consecutive injection events are merged. An approximate method can be used: the latter part of the flow-rate curve pertaining to the first shot and the initial part of the flow-rate curve pertaining to the second shot are approximated with straight lines (cf. dashed lines in Figs. 3.17a and 3.17b). IFT is determined when the intersection point between these straight lines occurs at a virtually nil flow-rate value. For the considered working conditions, the IFT occurs at $DT = 160 \text{ } \mu\text{s}$ for the pilot-main injections (cf. Fig. 3.17a) and at $DT = 620 \text{ } \mu\text{s}$ for the main-after injections (cf. Fig. 3.17b).

By using Zeuch method-based flowmeters, such as HDA and Mexus [11], the injections do not show any anomalous tail after the nozzle closure event. Furthermore, Zeuch method-based flowmeters can as well provide a measurement of the injected mass. Three newly developed criteria are here proposed for identifying IFT in Zeuch method-based flowmeters.

The first method relies on the injected mass. If two injections are merged, the total injected mass is correctly measured, whereas the injected masses pertaining to each shot cannot be accurate. With reference to the same nominal pressure and ET values shown in Fig. 3.17, Figs. 3.18a and 3.18b

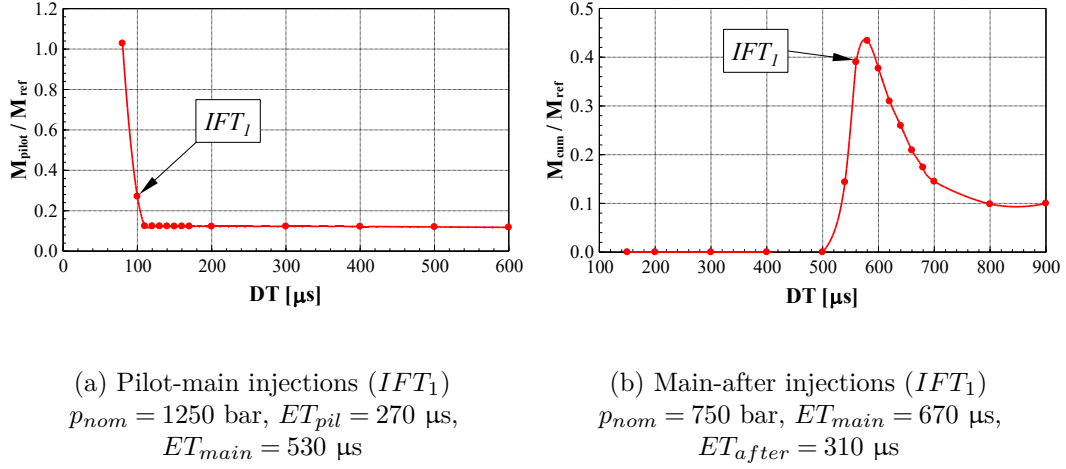
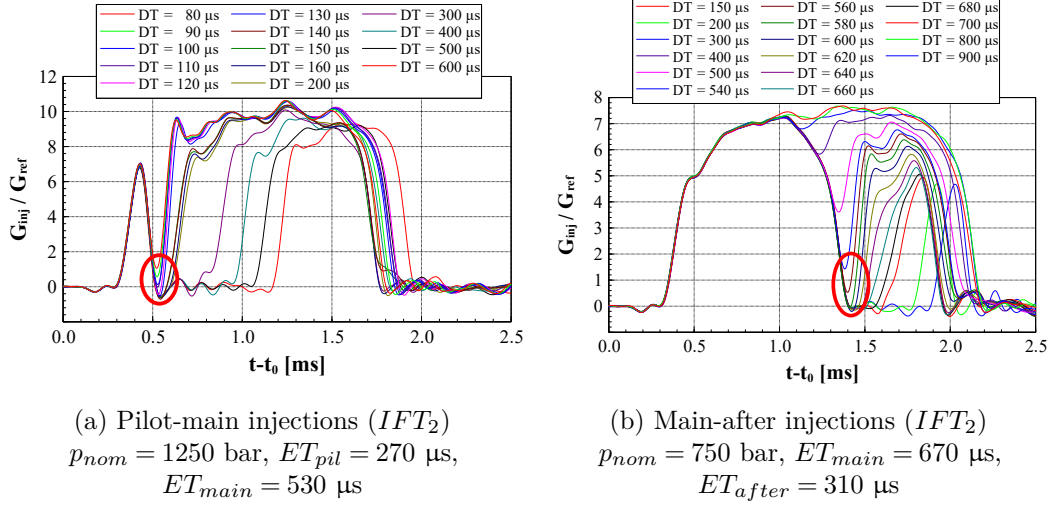
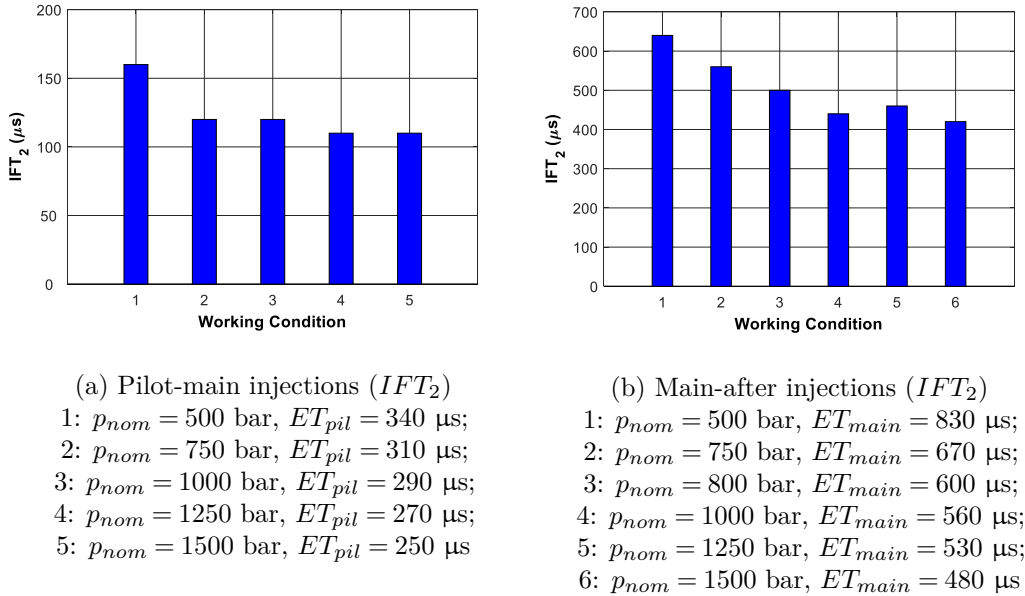


Figure 3.18: Injected masses under different DT s (IFT_1 determination).

report the pilot and the after injection mass values, respectively, as measured by HDA. Fig. 3.18a shows that the measured pilot injected mass at $DT = 100$ μs presents a greater value than the nominal one, while it is smaller than the sum of the pilot and main quantities: this abnormality means that injection fusion happens at this working point with a certain percentage of probability and the corresponding DT is marked as IFT_1 .

A similar method can be adapted to main-after injections in Fig. 3.18b. However, the difference compared to Fig. 3.18a, in which the pilot injected mass keeps constant in the absence of fusion, is that, as already mentioned, when DT reduces below DT_{cr} , the after injection mass should gradually augment. This occurs up to $DT = 560$ μs in Fig. 3.18b, whereas, for lower DT values than this threshold, the HDA estimated after injection mass results to reduce abruptly, thus highlighting that a part of the after injection is computed in the main injected mass, consistently with a fusion phenomenon occurrence. As a result, $DT \approx 560$ μs is regarded as the IFT_1 .

The second method for determination of IFT is based on the flow-rate curves shown in Figs. 3.19a and 3.19b (the working conditions are the same as in Fig. 3.17), which are acquired by means of Mexus. The injection fusion threshold is here defined as the greatest DT for which no flow-rate value between the two electric current time histories is equal or below zero. Therefore, the pilot-main injection IFT (marked as IFT_2) occurs at $DT = 110$ μs , while the main-after injection IFT_2 is at $DT = 560$ μs . The IFT_2 of pilot-main

Figure 3.19: Injection flow-rates under different DT s (IFT_2 determination).Figure 3.20: The IFT s based on the 2nd criterion.

and main-after injections are shown in Figs. 3.20a and 3.20b, respectively, for different working conditions. However, due to the pressure transients in the measuring chamber of Zeuch method-based flowmeters, it is possible that the flow-rate value between the two current time histories goes below zero even in the presence of merged injection. As a consequence, there is the possibility that fused injections are regarded as two distinct injection events.

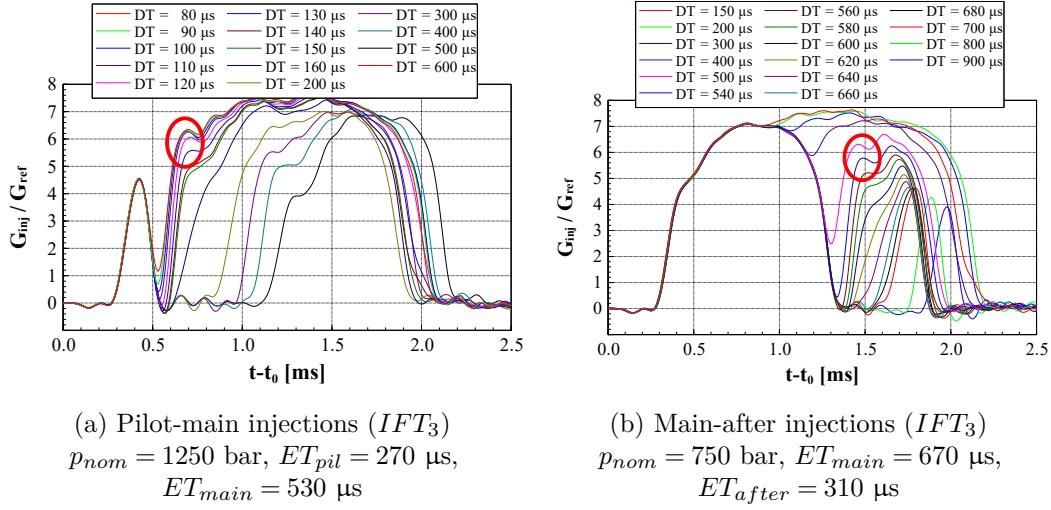


Figure 3.21: Injection flow-rates under different DT s (IFT_3 determination).

For HDA, when DT is close to IFT , a flow-rate peak is observed at the beginning of the second injection (cf. the circled areas in Figs. 3.21a and 3.21b). Such a phenomenon also occurs in the corresponding flow-rates data acquired by means of the Mexus, (cf. Fig. 3.19), but is not detected in the flow-rate profiles pertaining to the EVI device (cf. Fig. 3.17), which, as already mentioned, is a Bosch method based flowmeter. The peak takes place at slightly lower DT s than IFT_2 and there is satisfactory repeatability under different nominal pressures. A compressed wave, triggered by the closure of the needle at the end of the former shot, is reflected at the injector inlet as a compressed wave and is transmitted to the nozzle, thus inducing the flow-rate peak. As a consequence, the largest DT for which this peak can be observed is treated as the third criterion and gives rise to IFT_3 . In Fig. 3.21, IFT_3 is 130 μ s for the pilot-main injections and is 600 μ s for the main-after injections.

It can be inferred that the injection fusion threshold determined according to the three new criteria is generally smaller than that obtained on the basis of the EVI data. This proves that the Bosch method based flowmeters can lead to higher possibility of inaccuracy in the estimation of IFT . Since the IFT_2 values are generally intermediate between those of IFT_1 and IFT_3 , the three criteria have been compared by assuming IFT_2 as the reference. With reference to pilot-main and main-after injection data reported Fig. 3.20, quantities $\Delta IFT_1 = IFT_1 - IFT_2$ and $\Delta IFT_3 = IFT_3 - IFT_2$ are plotted in Figs. 3.22a and 3.22b respectively. It should be noted that there is no overlap

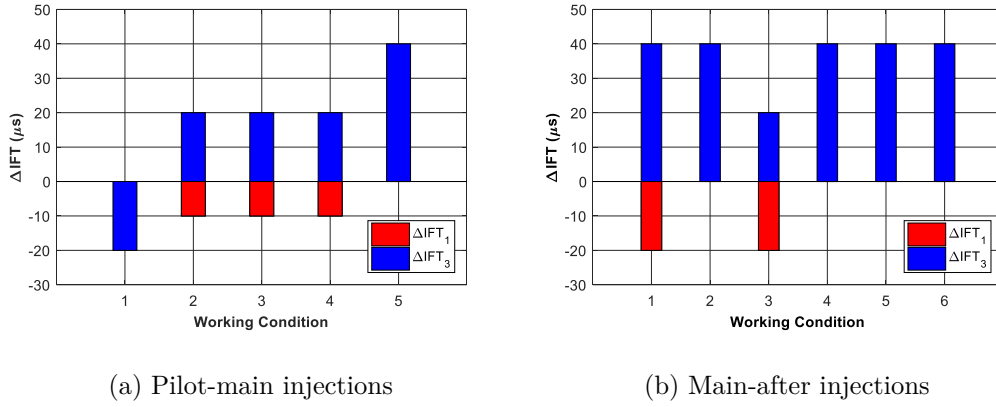


Figure 3.22: Analysis of the differences between IFT_1 , IFT_2 and IFT_3 .

between the bars of the graphs. Furthermore, for working conditions 1, 5 in Fig. 3.22a and 2, 4-6 in Fig. 3.22b, $IFT_1 \approx IFT_2$ and hence $\Delta IFT_1 = 0$.

3.3.3 Cycle-to-cycle dispersion analysis

The cycle-to-cycle dispersions in M_{cum} , evaluated by means of the HDA instrument under varied DT values for the pilot-main injections ($p_{nom} = 1250$ bar, $ET_{pil} = 270$ μs and $ET_{main} = 530$ μs) and the main-after injections ($p_{nom} = 750$ bar, $ET_{main} = 670$ μs and $ET_{after} = 310$ μs), are reported in Figs. 3.23a and 3.23b. As regards the pilot-main injections plotted in Fig. 3.23a, the

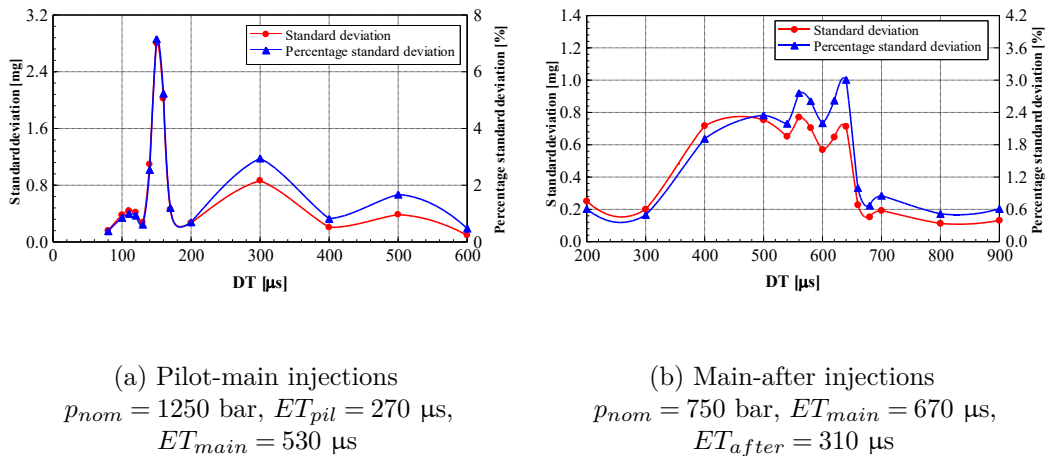


Figure 3.23: Cycle-to-cycle dispersion in M_{cum} for double injections.

IFT_2 is approximately $130 \mu\text{s}$, and with respect to the main-after injections demonstrated in Fig. 3.23b, the IFT_2 value is around $560 \mu\text{s}$. It is distinct that the cycle-to-cycle dispersions evidently ascend as the DT values are close to the corresponding IFT_2 . Whereas, if the DT is small enough compared to this threshold ($DT \leq DT_{max}$ in pilot-main injections or $DT \leq DT_{sat}$ in main-after injections), the cycle-to-cycle dispersions in M_{cum} descend and turn to be comparable to those for the DT longer than $600 \mu\text{s}$ for pilot-main injections or $700 \mu\text{s}$ for main-after injections.

Generally, in Fig. 3.23 the DT ranges, in which the cycle-to-cycle dispersions are relatively high, match the DT intervals of the corresponding $M_{cum} - DT$ graphs, where the M_{cum} rising rate by decreasing DT is great ($DT_{max} < DT < DT_{cr}$ in Fig. 3.24a and $DT_{sat} < DT < DT_{cr}$ in Fig. 3.24b). Furthermore, IFT_2 generally takes place in the center of the zone where M_{cum} increases sharply by reducing DT , while it can be as well close to DT_{max} for pilot-main injections.

Fig. 3.25 reports some of the mass flow-rates acquired by means of HDA for 25 consecutive engine cycles with respect to some typical operating points. Fig. 3.25a reports the injection rate time distribution referring to the maximum cycle-to-cycle dispersion in Fig. 3.23a. Two distinct families of injection flow-rate time histories can be observed, and this point as well refers to an irregular trend of the $M_{cum} - DT$ curve in the vicinity of $DT = 150 \mu\text{s}$ in Fig. 3.24a.

On the basis of the dispersion data reported in Fig. 3.23, as the standard deviation starts to increase when DT reduces, such as $DT = 300 \mu\text{s}$ for pilot-

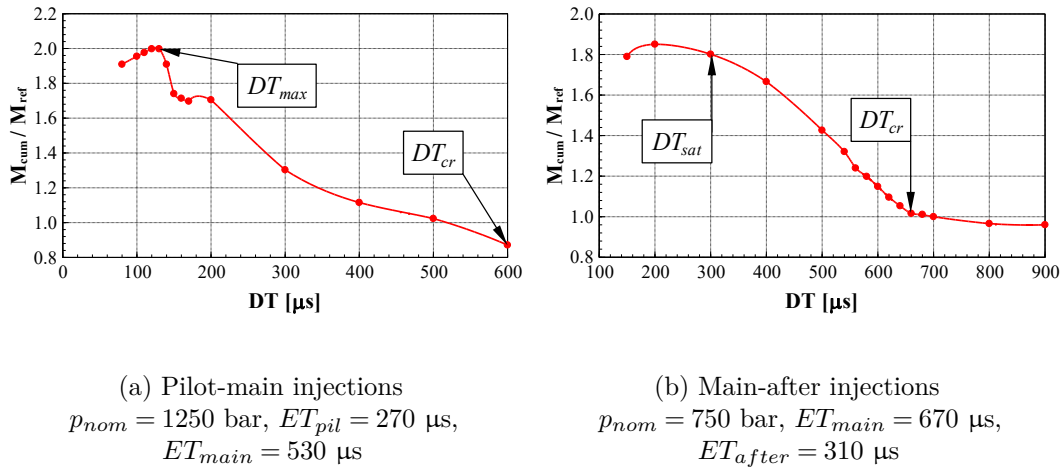


Figure 3.24: Injected mass depending on DT for double injections.

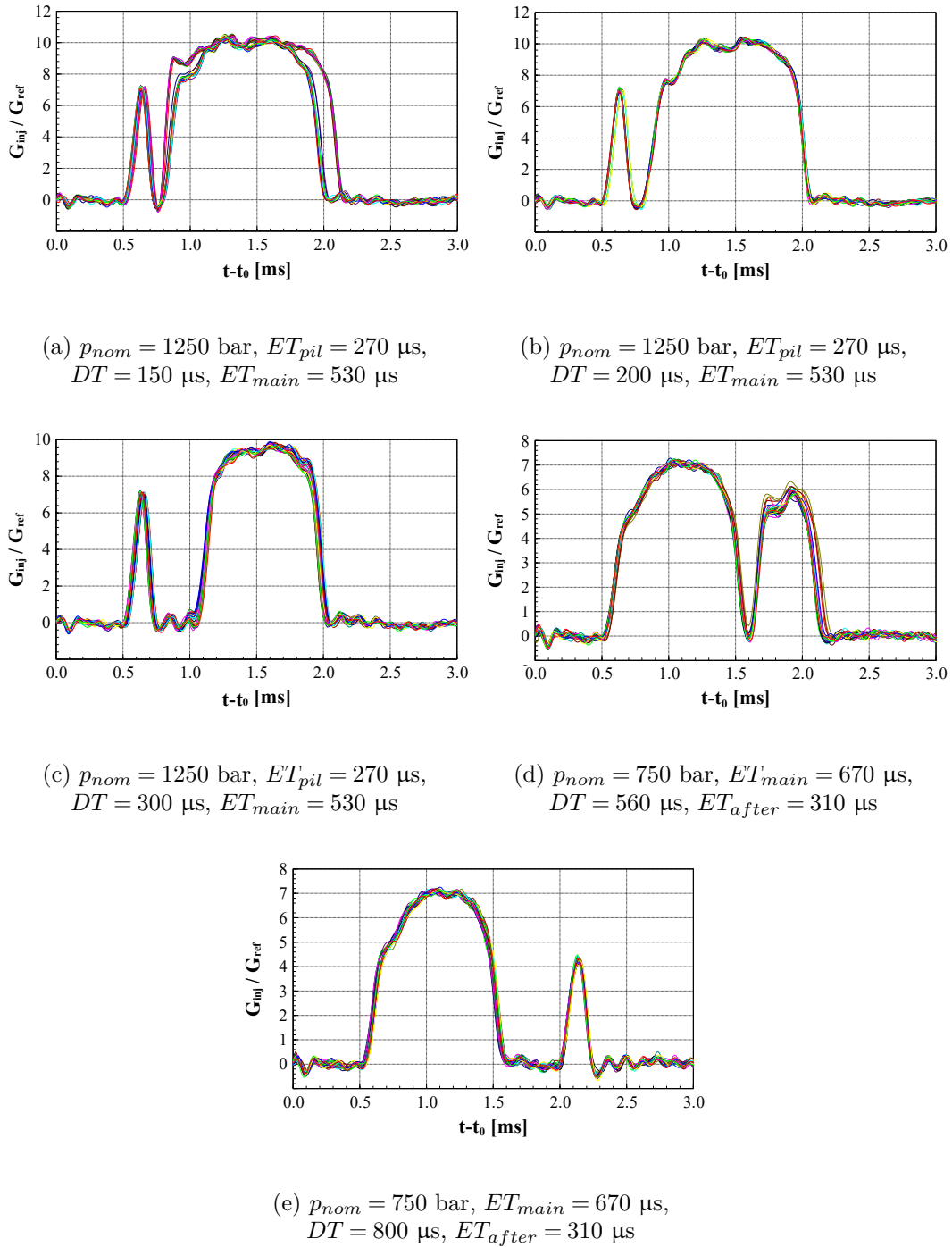


Figure 3.25: Cycle-to-cycle dispersion in injection rates.

main injections shown in Fig. 3.25c and $DT = 560$ μ s for main-after injections demonstrated in Fig. 3.25d, some variations in the injected flow-rate time

histories can be detected. Whereas, no distinct different families of the flow-rates can be found in those two figures. In addition, if the cycle-to-cycle dispersions in the M_{cum} are enough low, such as $DT = 200 \mu\text{s}$ reported in Fig. 3.25b and $DT = 800 \mu\text{s}$ exhibited in Fig. 3.25e, the injection rate time distributions for different engine cycles are generally coincident.

All of the previously discussed proofs indicate that the increase in the cycle-to-cycle dispersion of M_{cum} correlates well with the slope of the $M_{cum} - DT$ curve in the region of DT_{max} (or DT_{sat}) $< DT < DT_{cr}$. A great value of the slope or the presence of the irregular variations in the same slope in Fig. 3.24 induce an augment in the cycle-to-cycle dispersion of M_{cum} . Such a phenomenon significantly worsens the coefficient of variation of the indicated mean effective pressure and turns to be the primary obstacle to fully exploit the benefit of digital and continuous rate-shaping strategies in solenoid injectors [99].

Therefore, if the interval of DT_{max} (or DT_{sat}) $< DT < DT_{cr}$ can be shortened or shifted, there will be wider suitable and exploitable DT range, in which low dispersions in the M_{cum} occur. Continuous and digital rate-shaping techniques can be thus more efficiently applied.

3.3.4 Numerical model

The numerical tests have been conducted based on a previously developed 1D diagnostic model of a CR system, featuring a solenoid injector equipped with a pressure-balanced pilot valve. Fig. 3.26 reports the schematic of the model in which CRI 2.18 injector is adopted [111]. The model contains the high-pressure circuit of the injection system with one detailed injector submodel, in which the hydraulic, the mechanical and the electromagnetic components are simulated. In short, the hydraulic portion of the model is a network of 0D chambers, in which the pressure is uniform, connected by means of either calibrated orifices or 1D pipes.

The fluid dynamics along the 1D pipes is governed by the generalized Euler partial differential conservation equations of mass and momentum balance:

$$\frac{\partial}{\partial t} \begin{bmatrix} \rho \\ \rho u \end{bmatrix} + \frac{\partial}{\partial x} \begin{bmatrix} \rho u \\ \rho u^2 + p \end{bmatrix} = \begin{bmatrix} 0 \\ -4\tau_w/D \end{bmatrix} \quad (3.5)$$

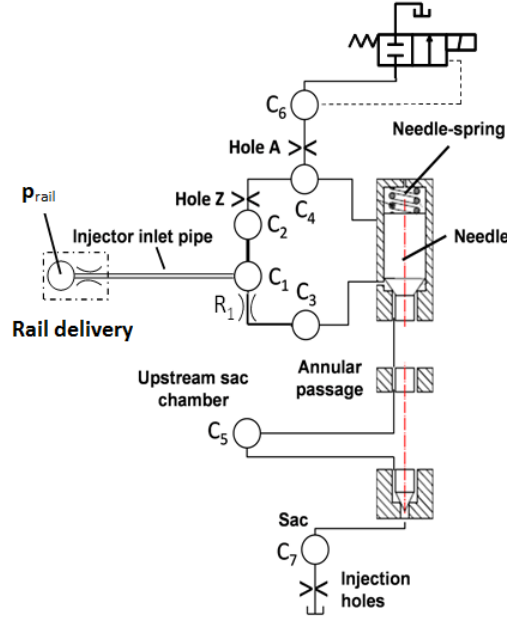


Figure 3.26: Schematic of the numerical model of the CR system.

in which τ_w models the wall shear stress, including both a steady-state term and a frequency dependent friction term as discussed in Sect. 2.3.1. Since no energy equation is considered and an iso-thermal evolution is applied, the state equations are adopted to compute the effects due to the fuel compressibility.

As regards the mechanical parts, the needle and the pilot valves are governed by Newton equilibrium ordinary differential equations. Furthermore, the electromagnetic force (F_m) that acts on the pilot valve is expressed as a function of the energizing current (I)

$$|F_m| = \frac{N^2 I^2}{2\mu_0 R^2} \left(\frac{1}{\Sigma_1} + \frac{1}{\Sigma_2} \right) \quad (3.6)$$

where N represents the number of injector solenoid windings, R is the reluctance of the entire magnetic circuit, varying linearly with the lift of pilot valve [112], μ_0 stands for the magnetic constant and Σ are the cross sections of the magnetic circuit. The first of these cross sections is delimited by the internal surface of the recirculation passage and by the solenoid internal area, while the second is confined by the solenoid external surface and by the anchor.

The energizing current time history supplied to injector solenoid and the rail fuel pressure time distributions are applied to the numerical model as the

boundary conditions. Among those, the rail pressure data allows the effects of the pressure control system and of the pump to be considered [111].

Some challenging model validation examples of the injector inlet pressure time history and the injection rate are reported in Fig. 3.27. Moreover, $M_{cum} - DT$ curves of the same injection system for both pilot-main and main-after injections are as well plotted in Fig. 3.28. In general, the agreement between the numerical and the experimental data plotted in Figs. 3.27 and 3.28 confirms the reliability of the model for the simulations in multiple injections. Particularly, the satisfactory estimation of the injector internal pressure time history indicates a good accuracy of the hydraulic section within the model.

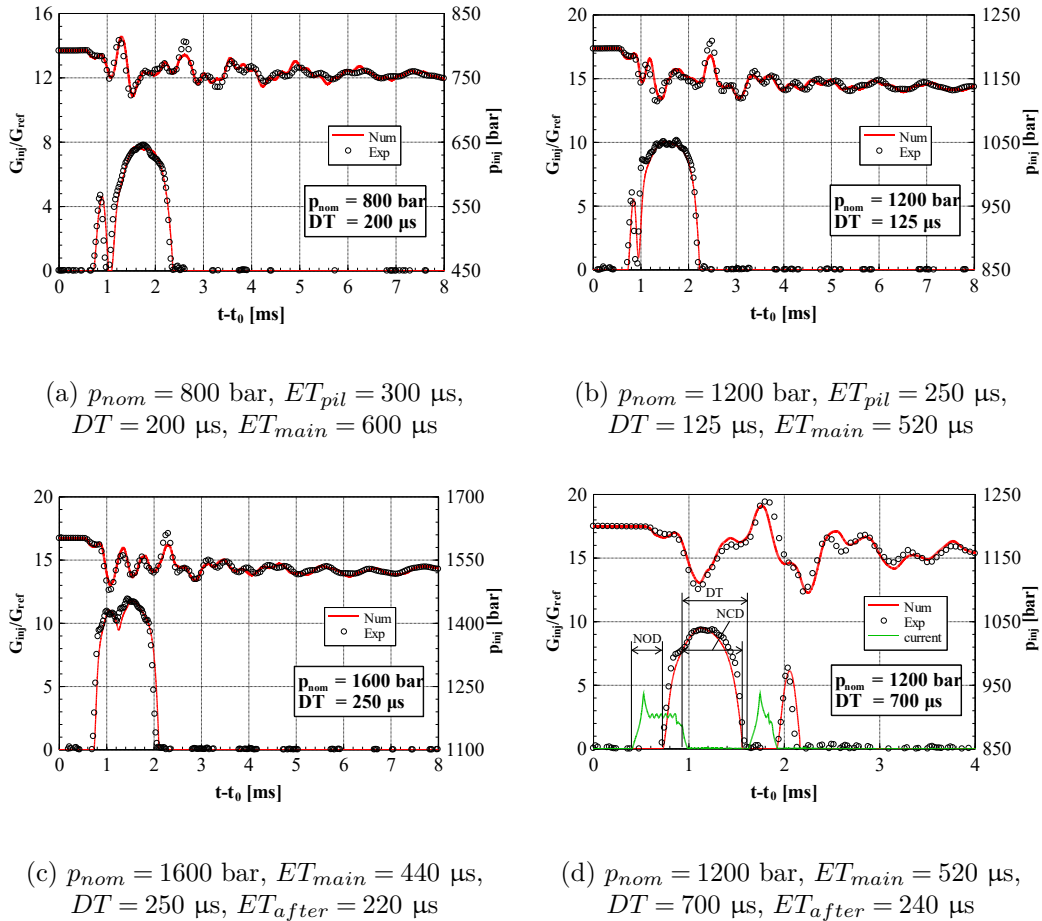


Figure 3.27: Injected mass flow-rates and injector inlet transients model validation tests under different operating conditions.

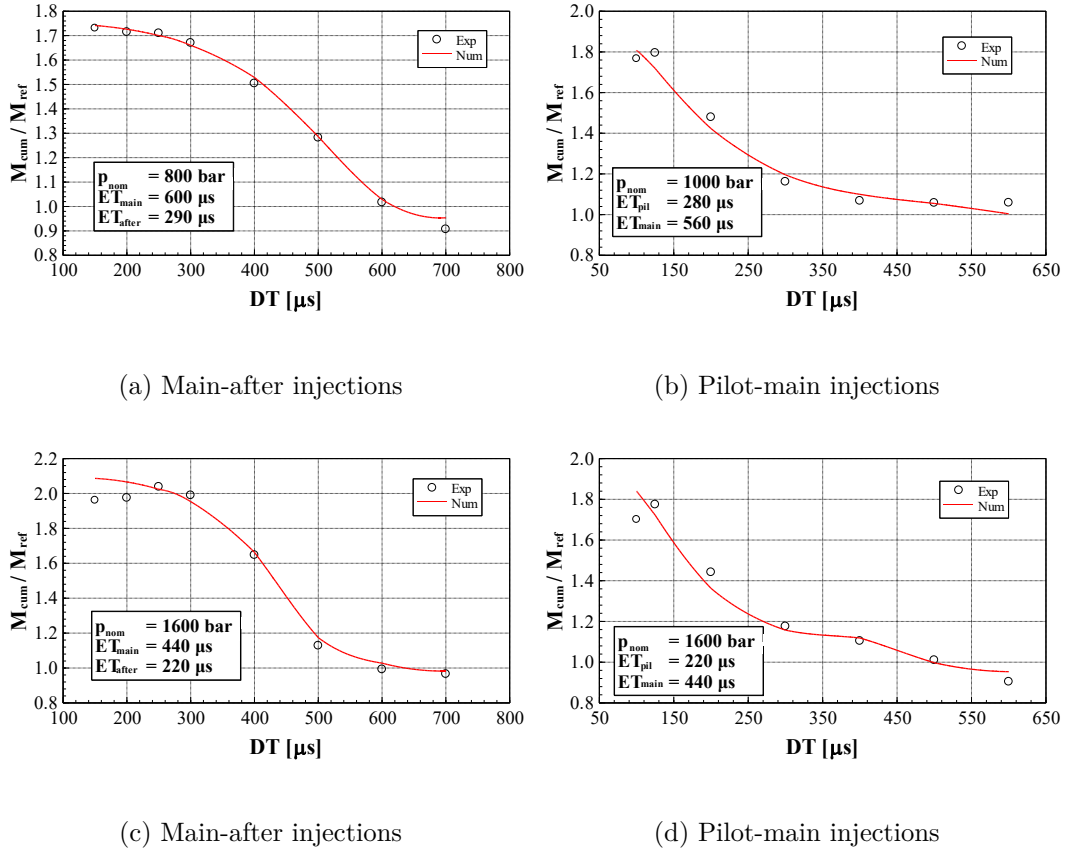


Figure 3.28: Overall injected mass model validation tests under different operating conditions.

Moreover, the accurate prediction of the NOD , NCD and the injected flow-rate guarantees the reliability in the calculation of IFT_2 .

3.3.5 Methodology applied in the parametric tests

Numerical tests have been conducted to evaluate the effects of the key parameters of the CRI 2.18 injector layout on continuous and digital injection rate-shaping techniques. As one parameter is modified, the injected fuel quantity under the fixed values of ET , of DT , and of p_{nom} generally varies. In consequence, in order to avoid significant variation in the hydraulic effects, the ET s of the double injection have been calibrated in the parametric tests to maintain the mass injected per shot by fixing p_{nom} and when DT is sufficiently large.

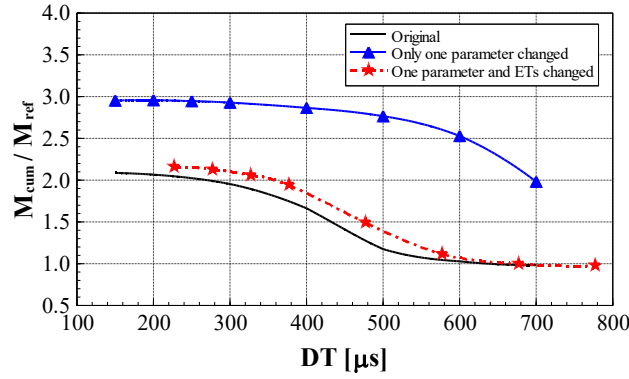


Figure 3.29: M_{cum} as a function of DT ($p_{nom} = 1600$ bar, $M_{main} = 20$ mg), $M_{after} = 2.5$ mg.

Fig. 3.29 plots the M_{cum} as results of different methods applied for the parametric tests. The solid curve without symbol is the numerical result of M_{cum} data for a main-after injection working condition ($p_{nom} = 1600$ bar, $ET_{main} = 440$ μs , $ET_{after} = 220$ μs , $M_{main} = 20$ mg and $M_{after} = 2.5$ mg) based on the original setup of the injector. In addition, both the continuous curves with triangle and star symbols correspond to the injector layout with one identical parameter modified. The curve with triangle symbols refers to the same ET s as the original setup, while in the curve with star symbols, the ET s have been tuned in order to retain the original injected mass ($M_{main} = 20$ mg and $M_{after} = 2.5$ mg) under the working condition with a relatively large DT .

By taking into account that the first injection takes place at $p_{nom} = 1600$ bar, ET_{main} has been preliminarily adjusted in the modified injector to match the nominal M_{main} . In result, the pressure waves induced by this shot turn to be analogous to that of the original injector working at the same p_{nom} and M_{main} levels. A relatively large DT value (700 μs for main-after injections tests in the present investigations) has been chosen to adjust the ET_{after} to basically restore the injected quantity of the after injection pertaining to the original injector. By applying this method, new ET s are selected respectively for the main and the after injections, and the DT value should be progressively modified in order to synchronize the pressure waves with those pertaining to the same working condition performed by means of the original injector. In results, the dashed-dotted curve with star symbols pertaining to the modified

injector is derived. Similarly, pilot-main injection tests can as well be adjusted by adopting the same method. Whereas ET_{pil} should be initially selected, and the relatively large DT value is chosen as $600 \mu\text{s}$ in this case.

It is noteworthy that the p_{rail} time distributions, captured under the operating conditions by means of the original injector, has been applied to the numerical model as one boundary condition as well for the modified injector. Since the newly triggered pressure waves by adopting the above mentioned method can reproduce the analogous phenomena from hydraulic point of view, and the modifications in the parametrical analyses generally concern details of the injector layout, which has minor effects on the dynamics of p_{rail} , the original hydraulic boundary condition can be thus generalized in those cases to couple the responses of the pump and of the pressure control system.

However, in the investigations of the delivery chamber volume (V_{dc}), the p_{rail} value is assumed to be constant, since an evident change in V_{dc} can significantly affect the p_{rail} trace. In this case, the ET s pertaining to the two shots in the considered double injections have been separately adjusted in order to reproduce the nominal injected mass by means of two purposely-designed numerical tests on the modified injectors with the new V_{dc} value performing single injections.

3.3.6 Results of the parametric tests

The parametric analyses have been conducted on the numerical model referring to a CRI 2.18 injector (cf. Fig. 3.30). All the tests have been performed on the DT sweeps of the working conditions reported in Tab. 3.1. Figs. 3.31-3.39 demonstrate the $M_{cum} - DT$ graphs as the injector setups, listed in Tab. 3.1, are modified. Besides, in the legends of the plots, the IFT (the IFT_2 discussed in Sect. 3.3.2) values pertaining to each investigated values of the modified setup variables for pilot-main injections are presented.

The first group of the tests has been conducted on the diameter of the control piston (cf. d_{cp} in Fig. 3.30). Figs. 3.31a and 3.31b respectively report the DT sweeps for the pilot-main injections and for the main-after injections. The variations in d_{cp} investigated are up to $\pm 4\%$, based on the baseline value, since the performance of the injector is quite sensitive to this variable, and a modification of 4% of the value can induce a significant change in the injected flow-rate patterns. In fact, the objective of this investigation is to optimize

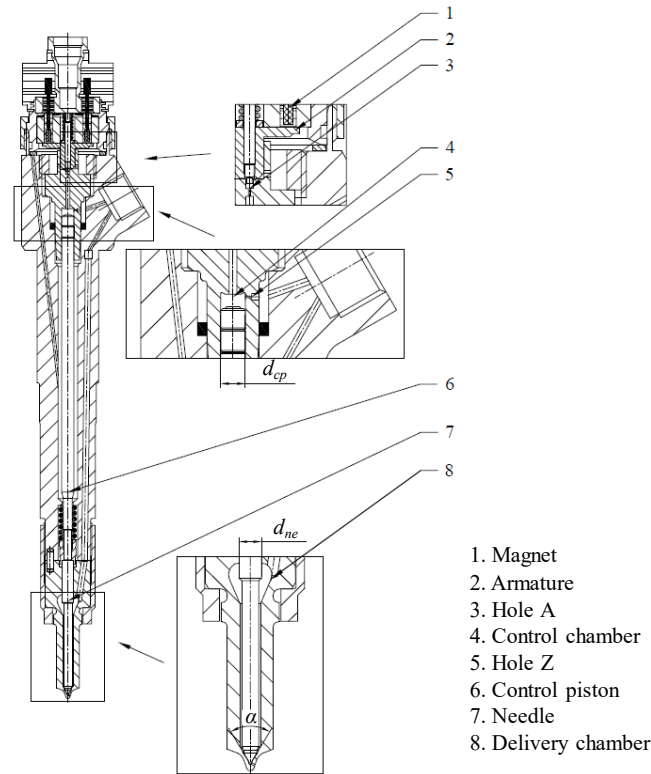


Figure 3.30: Investigated solenoid injector (CRI 2.18 injector).

Table 3.1: Working conditions and the parameters analyzed

Working conditions	
pilot-main	$p_{nom} = 1000 \text{ bar}$, $M_{pil} = 2.5 \text{ mg}$, $M_{main} = 20 \text{ mg}$
main-after	$p_{nom} = 1600 \text{ bar}$, $M_{main} = 20 \text{ mg}$, $M_{after} = 2.5 \text{ mg}$
Parameters analyzed	
1	diameter of the control piston (d_{cp})
2	external diameter of the needle (d_{ne})
3	hole A diameter (d_A)
4	hole Z diameter (d_Z)
5	air gap (L_{gap})
6	maximum current level (L_{max})
7	needle valve cone angle (α)
8	delivery chamber volume (V_{dc})
9	control chamber volume (V_{cc})

the injected flow-rate performance in the vicinity of IFT without modifying evidently the injection rate time distributions.

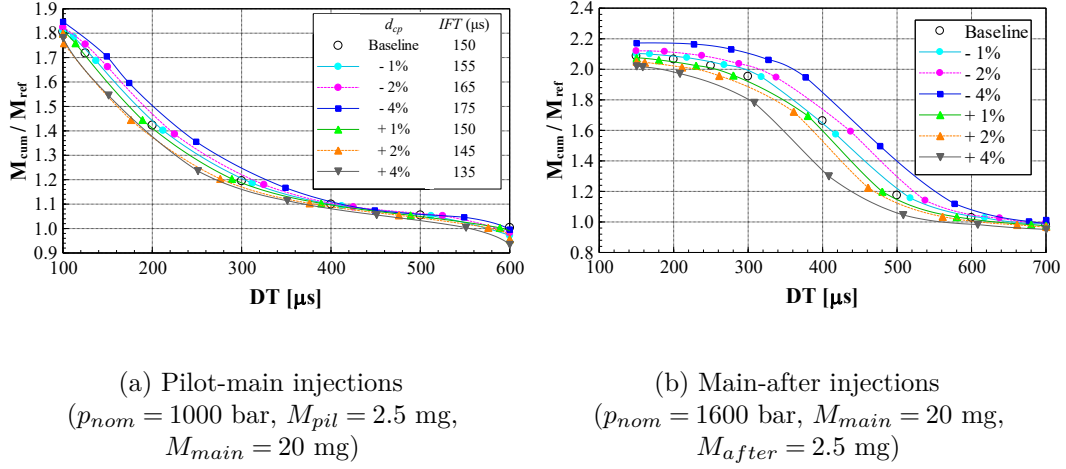


Figure 3.31: DT sweeps for different values of d_{cp} .

As regards the pilot-main injections plotted in Fig. 3.31a, no saturation point is observed in M_{cum} as DT decreases, and DT_{max} takes place below $100 \mu\text{s}$. Whereas the saturation presents distinctly in the main-after injections reported in Fig. 3.31b. As above discussed, the M_{cum} values have been adjusted to be generally identical with different parameters set at $DT = 600 \mu\text{s}$ in Fig. 3.31a and at $DT = 700 \mu\text{s}$ in Fig. 3.31b, while M_{cum} vary as DT reduces.

An increase in d_{cp} enlarges the area on which the fuel pressure in the control chamber acts. Thus, the force that closes the needle valve turns to be amplified. If a ballistic injector is adopted, the maximum needle lift during one hydraulic injection tends to be lowered, and the NOD reduces. Such a decrease in the NCD of the former injection leads to a reduction in the IFT (cf. Fig. 3.31a). Meanwhile, as d_{cp} is amplified, for both the pilot-main and the main-after operating conditions, the $M_{cum} - DT$ curves in Fig. 3.31 tend to move to the left. Moreover, DT_{sat} in Fig. 3.31b shifts for approximately $50 \mu\text{s}$, from around $200 \mu\text{s}$ to about $150 \mu\text{s}$, when a change of $+4\%$ is provided to d_{cp} starting from the baseline value. However, no distinct alteration in DT_{max} can be found in the both graphs in Fig. 3.31. In addition, with the same alteration of the d_{cp} value, a reduction in DT_{cr} as well as in the interval of $DT_{sat} < DT < DT_{cr}$ is thus obtained (cf. 3.31b).

The results of the parametric analyses on the external diameter of the needle (cf. d_{ne} in Fig. 3.30), reported in Fig. 3.32, are analogous to those pertaining to the variable d_{cp} (cf. Fig. 3.31). Indeed, an increase in d_{ne} amplifies the

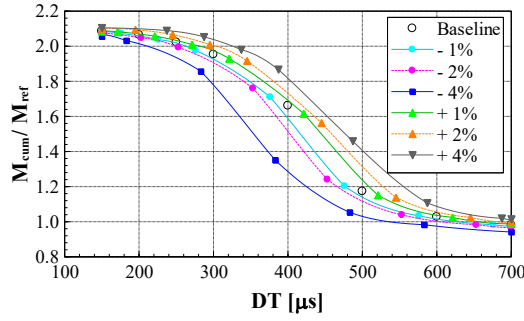
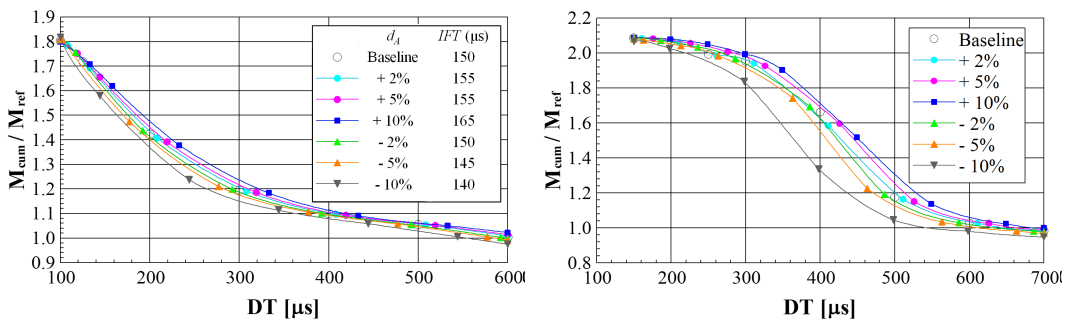


Figure 3.32: DT sweeps in the main-after injections for different values of d_{ne} ($p_{nom} = 1600$ bar, $M_{main} = 20$ mg, $M_{after} = 2.5$ mg).

pressure force that opens the needle valve. In result, an enlargement in d_{ne} is expected to exert an analogous influence as a decrease in d_{cp} . Fig. 3.32 confirms this hypothesis in the case of main-after injection patterns. As d_{ne} rises, the DT_{cr} value as well as the interval of $DT_{sat} < DT < DT_{cr}$ progressively increase.

Figs. 3.33 and 3.34 respectively exhibit the numerical tests pertaining to hole A diameter (d_A) and hole Z diameter (d_Z). Among those Figs. 3.33a and 3.34a display the influence of the values of the d_A and of the d_Z on the pilot-main injection performance, while Figs. 3.33b and 3.34b report the effects of the same parameters on the DT sweeps in main-after injections.



(a) Pilot-main injections
($p_{nom} = 1000$ bar, $M_{pil} = 2.5$ mg,
 $M_{main} = 20$ mg)

(b) Main-after injections
($p_{nom} = 1600$ bar, $M_{main} = 20$ mg,
 $M_{after} = 2.5$ mg)

Figure 3.33: DT sweeps for different values of d_A .

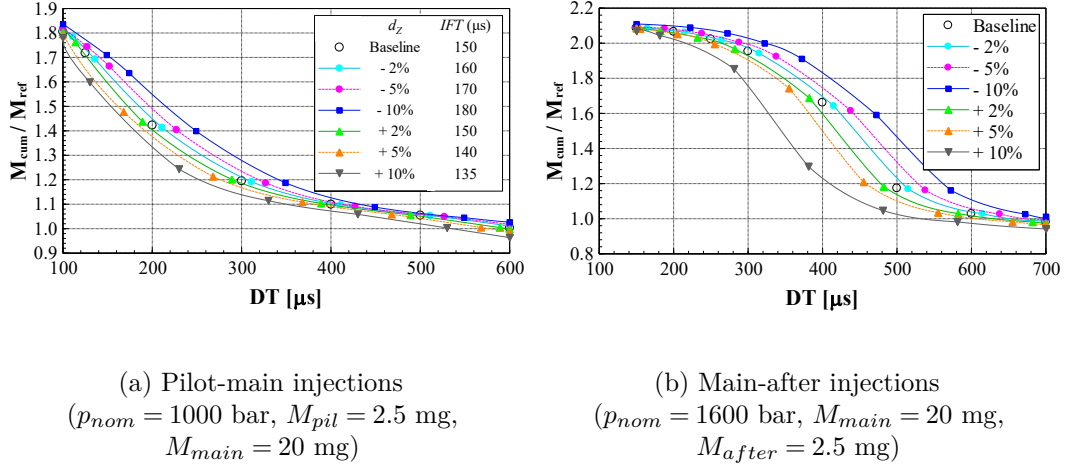
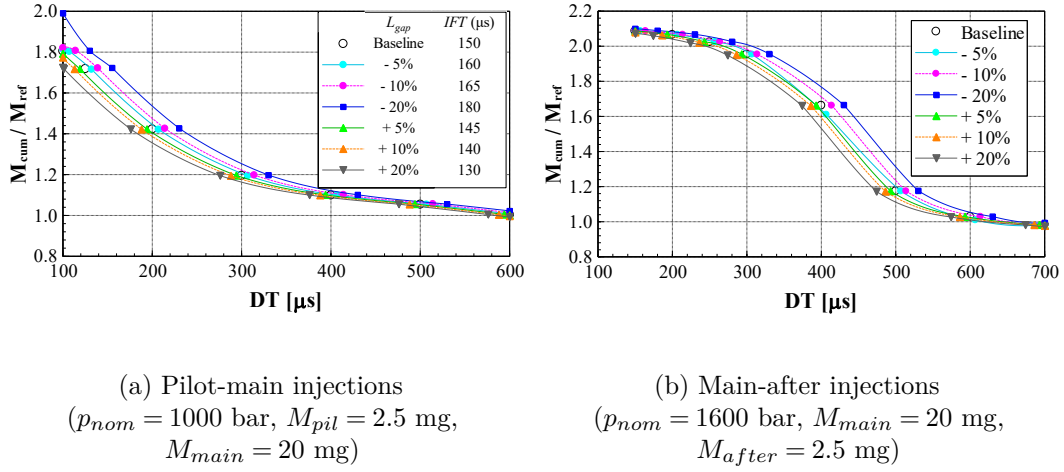
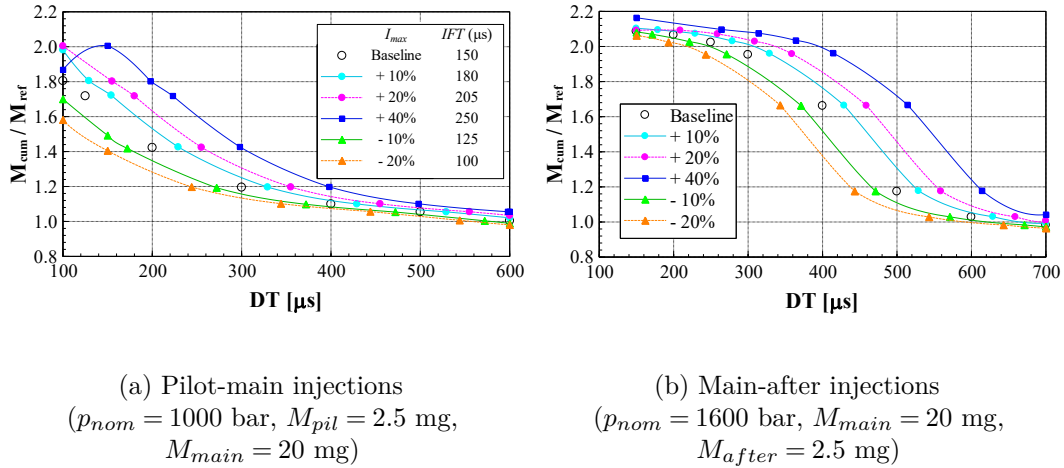


Figure 3.34: DT sweeps for different values of d_Z .

When d_A is enlarged, the emptying process of the control chamber turns to be faster. As a result, NOD diminishes, and the peak needle lift becomes higher. On the other hand, as d_Z reduces, the control chamber discharging is faster, and the refilling of the chamber after the current command becomes slower. The latter effect in turn augments the NCD value. As is observed in Figs. 3.33b and 3.34b, either an increment in d_A (up to +10% is feasible) or a reduction in d_Z (up to -10% is feasible) enlarges the values of DT_{sat} , DT_{cr} and IFT as well as the interval of $(DT_{cr} - DT_{sat})$. Moreover, the simulations results display that the injector performance is more sensitive to d_Z than to d_A .

The DT sweeps of the pilot-main and the main-after injections for the variable of the air gap (L_{gap}) are demonstrated in Fig. 3.35, while the results of the same tests on the maximum current level (I_{max}) provided to the solenoid are reported in Fig. 3.36. The electromagnetic force that lifts the pilot valve augments, when either L_{gap} diminishes or I_{max} grows. Under both situations, the opening time lengths of both the pilot valve and the needle valve increase. In result, the IFT is enlarged and the curves of $M_{cum} - DT$ shift to the right.

As can be observed in Figs. 3.35 and 3.36, DT_{sat} is affected by the L_{gap} and the I_{max} to different degree and in opposite ways. A certain increment (reduction) in L_{gap} has the identical effects on the DT_{max} , the DT_{sat} and the DT_{cr} as a smaller decrease (increase) in the I_{max} . Furthermore, a modification of the I_{max} even shifts the DT_{max} location in $M_{cum} - DT$ curves for pilot-main

Figure 3.35: DT sweeps for different values of L_{gap} .Figure 3.36: DT sweeps for different values of I_{max} .

injections. Similarly, the slopes of the same curves and the DT_{cr} value vary significantly. As I_{max} differs by 20–40%, remarkable corrections in the ET s are required to retain the identical injected mass when $DT > DT_{cr}$. Whereas the interval of $DT_{sat} < DT < DT_{cr}$ generally maintains. Moreover, the dynamics of both the mechanical components and the hydraulic response basically remain after the modifications of the electromagnetic parameters.

Figs. 3.31-3.36 report the effects of the parameters, which appreciably affect the performance of the double injection DT sweeps. On the other hand, Figs. 3.37-3.39 refer only to the hydraulic variables. Fig. 3.37 is related to the needle

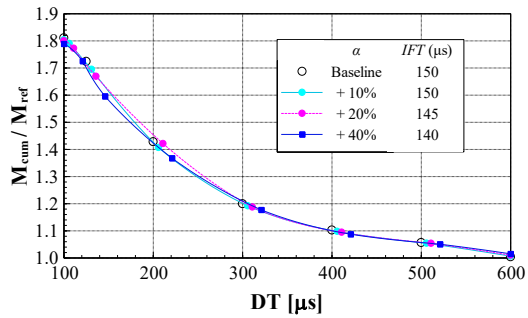


Figure 3.37: DT sweeps in the pilot-main injections for different values of α ($p_{nom} = 1000$ bar, $M_{pil} = 2.5$ mg, $M_{main} = 20$ mg).

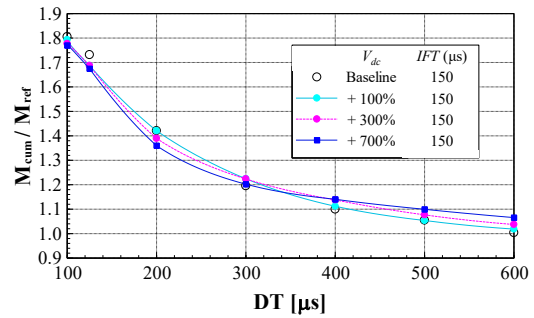


Figure 3.38: DT sweeps in the pilot-main injections for different values of V_{dc} ($p_{nom} = 1000$ bar, $M_{pil} = 2.5$ mg, $M_{main} = 20$ mg).

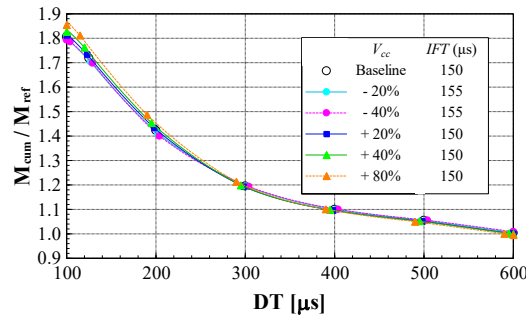


Figure 3.39: DT sweeps in the pilot-main injections for different values of V_{cc} ($p_{nom} = 1000$ bar, $M_{pil} = 2.5$ mg, $M_{main} = 20$ mg).

valve cone angle (cf. α in Fig. 3.30); Fig. 3.38 is connected to the volume of the delivery chamber V_{dc} (cf. item 8 in Fig. 3.30); Fig. 3.39 is linked to the volume of the control chamber V_{cc} (cf. item 4 in Fig. 3.30).

The needle valve cone angle generally varies the flow area between the needle and its seat (cf. 3.37). Whereas, the parametric analyses are carried out when the ET 's have been adjusted to respectively realize the same injected mass as the baseline tests for $DT > DT_{cr}$. α does not exert any evident effect on the DT sweeps. The similar phenomena have been discovered in the same analyses of the main-after injection, which have been omitted for the reason of conciseness.

Finally, no significant influence of V_{dc} and V_{cc} can be found on the DT sweep results of the pilot-main injections (cf. Figs. 3.38 and 3.39). In short, although Figs. 3.37-3.39 solely display the pilot-main injection results, it has been verified that similar conclusions, which are the minor influences of α , V_{dc} and V_{cc} on the DT sweeps, can be extended to the main-after injection patterns.

3.3.7 Benchmark between injectors with Minirail and without it

Two injection systems equipped with the same high-pressure pump and the same common rail are adopted in the experimental campaign, while the only difference between the two systems are respectively the installed CRI 2.18 (without Minirail and cf. Fig. 3.40) and CRI 2.20 (2 cm³ Minirail is integrated with the delivery chamber and cf. Fig. 3.41) injectors. DT sweeps on pilot-main injections have been conducted in the range of closely-coupled injections and of injection fusion at the hydraulic test bench. The ET s have been initially selected in order to achieve $M_{pil} = 2.5$ mg and $M_{main} = 20$ mg at $DT = 600$ μ s, and then the DT has been gradually lowered.

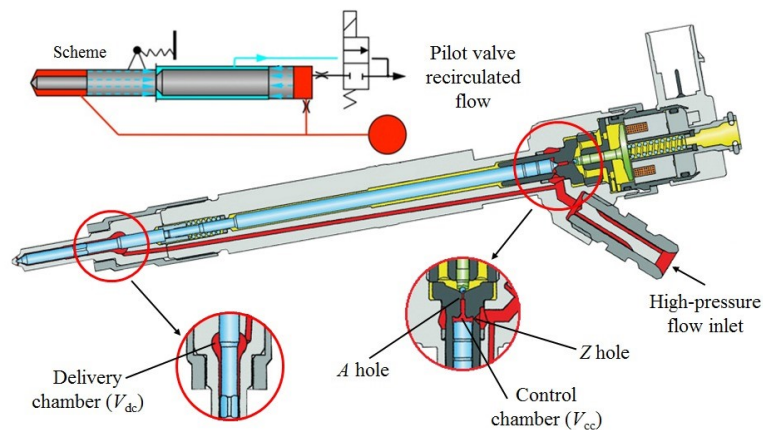


Figure 3.40: CRI 2.18 solenoid injector.

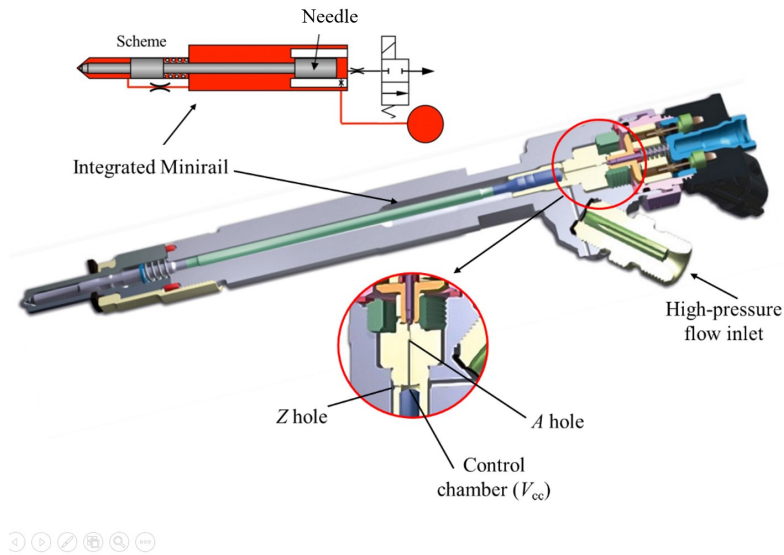


Figure 3.41: CRI 2.20 solenoid injector.

The overall injected mass M_{cum} and the percentage cycle-to-cycle dispersion data, which have been evaluated by means of the HDA, are plotted in Figs. 3.42 and 3.43. In general, as regards both systems, when DT diminishes below DT_{cr} , the M_{cum} augments rapidly, except for the DT range, where the anomalous reduction of M_{cum} takes place in the results of CRI 2.20 system (cf. the interval of $170 \mu s < DT < 200 \mu s$ in Fig. 3.42). The values of IFT are similar with respect to both the systems as displayed in Fig. 3.42. In short, IFT changes as ET_{pil} or p_{nom} varies. Therefore, comparisons on IFT pertaining to different systems are influenced by the investigated operating conditions. Moreover, based on the parametric tests above performed, it has been elaborated that even if the injector typology has been initially selected (such as the CRI 2.18 or the CRI 2.20), IFT can possibly differ with the mechanical, the hydraulic, and the electromagnetic setups as well as the fuel thermal states in the injector. In result, values of IFT under a selected operating condition can be discrepant for an injector type, if these data pertain to two injector samples, which equip different features of the pilot stage, of the needle or of the nozzle.

Similarly, it is as well confirmed in Fig. 3.43 that the cycle-to-cycle dispersion achieves the maximum values around the DT ranges of the IFT for both systems. With regards to the CRI 2.20 system, the abnormal reduction in the M_{cum} within the DT range of $DT_{max} < DT < DT_{cr}$ occurs in the right vicinity

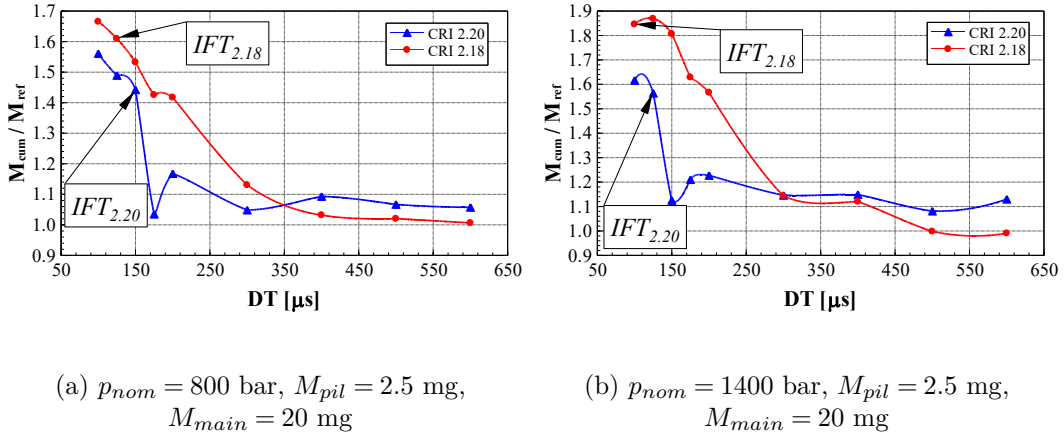


Figure 3.42: DT sweeps in the pilot-main injections for the systems of CRI 2.18 and of CRI 2.20.

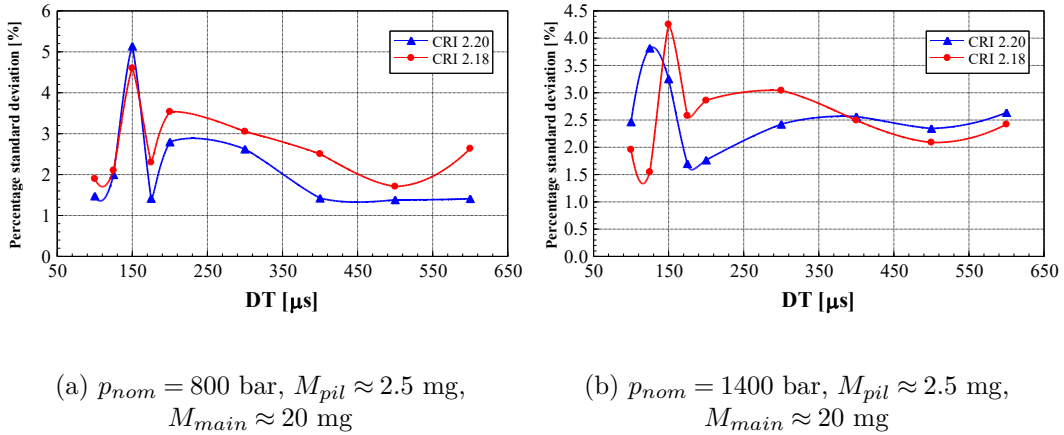


Figure 3.43: Cycle-to-cycle dispersions in the pilot-main injections for the systems of CRI 2.18 and of CRI 2.20.

of the IFT (cf. Fig. 3.42) and the phenomenon can be thus ascribed to the instability related to the injection fusions.

On the other hand, the DT_{cr} are substantially varied for those two systems. Particularly, the DT_{cr} values and the intervals of $DT_{max} < DT < DT_{cr}$ are evidently smaller in the results of the CRI 2.20 injector, and those provide a better performance in the digital rate-shaping strategy for the injectors of this type.

The dynamic responses of the solenoids equipped by those two injectors under a constant voltage have been evaluated, and it has been observed that the

results are similar. In addition, the design data of the primary electromagnetic variables, such as L_{gap} , I_{max} and the number of injector solenoid windings, provide analogous electromagnetic force to the pilot valves for the both injectors. Finally, the delivery chamber (or the Minirail) size (cf. item 8 in Fig. 3.30) merely provides a minor effect on DT_{cr} , as explained with Fig. 3.38. Therefore, the change in the performance of the injectors cannot be ascribed to this parameter.

The injectors of CRI 2.18 and of CRI 2.20 have been disassembled in order to measure the key geometrical parameters. The similar d_A values are adopted by the both injectors. Whereas, the d_Z of the CRI 2.20 injector is approximately three times of the that for the CRI 2.18. The parametric analyses have verified that an augment in d_Z can reduce all values of DT_{sat} , DT_{cr} and $(DT_{cr} - DT_{sat})$.

Since the Minirail is equipped by the CRI 2.20 injector, the unique mobile mechanical element in the high-pressure circuit is the needle, linking the control chamber and the nozzles. Meanwhile, in the CRI 2.18 injector body, two mobile mechanical components, the needle and the control piston (cf. items 7 and 6 in Fig. 3.30), are present. In order to compare the pressure forces that control the nozzle opening and closure between the two injectors, an equivalent area ratio (EAR) of the active surfaces present in the control chamber to those designed in the delivery chamber and around the nozzle has been introduced and calculated by experimentally measuring the dimensions. The active surfaces that in the control chamber determine the pressure force, which tends to push down the needle. While the pressure forces, exerted in the delivery chamber and on the nozzles, is capable to pull up the needle. It has been evaluated that the CRI 2.20 EAR is around half of that for CRI 2.18 injector. It can be inferred, based on the parametric analyses above performed, that a decrease in EAR can enlarge both DT_{cr} and $(DT_{cr} - DT_{sat})$. Even though the influence of a reduction in EAR mitigates the influence of an increment in d_Z , the values of DT_{cr} , DT_{sat} as well as $(DT_{cr} - DT_{sat})$ for main-after injections, sharply decrease passing from the CRI 2.18 injector to the CRI 2.20 injector.

It is noteworthy that the conclusions of the measurements of the internal features of the CRI 2.18 and the CRI 2.20 injectors are in line with the parametric analysis conclusions. It has been as well verified that the presence of a Minirail does not influence evidently the performance in the small DT

injection regime, whereas the other mechanical or electromagnetic variables in the injector are vital for the performance in the tested DT regimes.

Chapter 4

Closed-loop control strategy of injected mass

4.1 Experimental setup

The experimental campaign has been carried out on the Moehwald Bosch hydraulic test bench installed at the ICE laboratory of Politecnico di Torino as explained in Sect. 2.1. Similarly, the injection rate and the injected quantity of the injectors are evaluated by means of HDA [95]. The energizing current supplied to the investigated injector is measured by means of a current clamp.

In Sect. 4.2, in order to capture the pressure time histories in the high-pressure pipelines, as reported in Fig. 4.1, one piezoresistive pressure transducer is installed along the rail-to-injector pipe of the system. Meanwhile, a PXI (from National Instrument) is linked to the outputs of the pressure transducers and of the test bench, for the purpose of collecting the corresponding data with a frequency of 500 kHz.

On the other hand, in Sect. 4.3, two pressure piezoresistive transducers are mounted along the pipe. Furthermore, the PXI is linked with the two pressure sensors to acquire the pressure time distributions and to perform necessary calculations. The results of the computations are then fed to a flexECU, which, in a closed-loop, controls the energizing currents sent to the injectors and the duty cycles of the fuel metering valve (FMV) and of the pressure control valve (PCV) in the system.

Two state-of-the-art fuel injectors (CRI 2.18 and CRI 2.20), whose internal dimensions have been measured in Sect. 3.3.7, are involved in the following

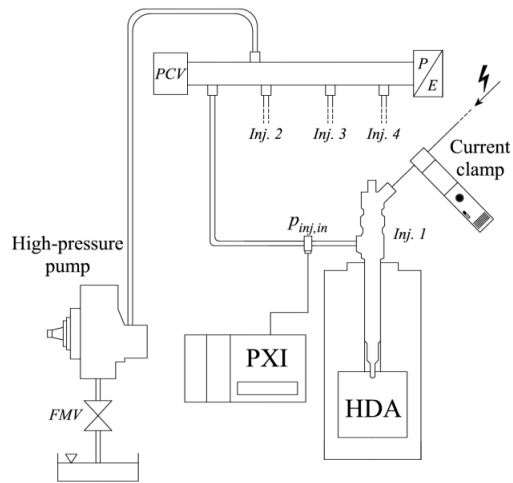


Figure 4.1: The experimental layout of the injection system for testing TFA based method.

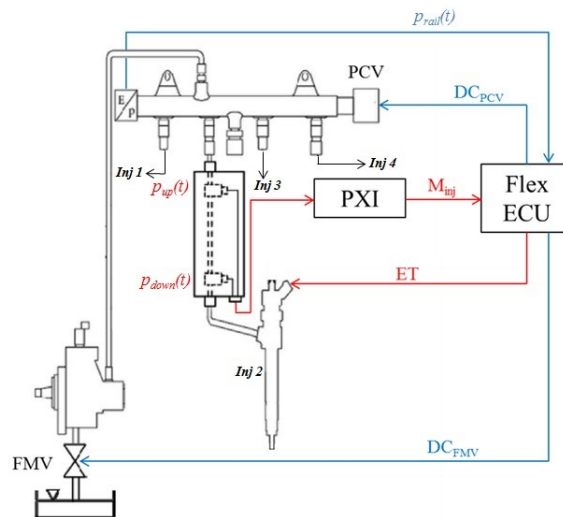


Figure 4.2: The experimental layout of the injection system for testing physical equation based methods.

experiments. In Sect. 4.2 and in the single injection tests within Sect. 4.3, CRI 2.20 are applied, while in the double injection tests within Sect. 4.3, CRI 2.18 are adopted. In addition, the same high-pressure pump and the same pipelines are employed in all the tests.

All the experimental tests of this chapter have been conducted at a fixed pump speed of 2000 rpm, corresponding to an engine speed of 2000 rpm. Since

the pump speed does not generate any obvious effect on the CR performance, the obtained results can be generalized to other engine speeds.

4.2 TFA based technique

4.2.1 Time-frequency analysis

The TFA is the method that investigates signals in both the time and the frequency domains, in order to indicate the variations in the frequency spectrum of a transient signal $g(t)$. In this section, the focus of the work is on the time instant identifications referring to the nozzle opening and closure time instants. A great number of fast Fourier transforms (FFT) are conducted over consecutive short time periods, which are overlapped, and each result of FFT is connected to the mean instant of this short time interval. It is assumed that stationary performance is owned by the unsteady signals over each time range. Therefore, a local frequency spectrum is formed. A windowing of signal $g(t)$ is in turn obtained by multiplying the signal $g(t)$ with a selected window function $h(t - \tau)$, which contains well unit energy and is non-zero only over the interval in the vicinity of time instant τ . The short time Fourier transform (STFT) is thus found as follows

$$F_l(\nu, \tau) = \int_{-\infty}^{+\infty} f(t) \cdot h(t - \tau) e^{-j2\pi\nu t} dt \quad (4.1)$$

Since the window function should not vary the energy, the energy density spectrum P is derived

$$P_f(\nu, t) = |F_l(\nu, t)|^2 \quad (4.2)$$

Denoted as E_f , the energy of signal f is expressed as

$$E_f = \int_{-\infty}^{+\infty} \int_{-\infty}^{+\infty} P_f(\nu, t) dt d\nu \quad (4.3)$$

The P_f can be written as a probability density function to evaluate the mean instantaneous frequency (*MIF*):

$$\bar{\nu}(t) = \frac{1}{\int_{-\infty}^{+\infty} P_f(\nu, t) d\nu} \int_{-\infty}^{+\infty} \nu \cdot P_f(\nu, t) d\nu \quad (4.4)$$

4.2.2 Injector characteristics

Evaluated by means of the HDA instrument, the average injected mass over 100 consecutive engine cycles with respect to different p_{nom} and ET are shown in Fig. 4.3. Two groups of data, in which the temperature of the in-tank fuel is set as either 40 °C (cf. dashed lines in Fig. 4.3) or 68 °C (cf. continuous lines in Fig. 4.3), are reported. Due to safety reasons, 68 °C refers to the maximum value reachable with the current test rig. With respect to each p_{nom} and T_{tank} value, the $M_{inj} - ET$ curves are fitted by third order polynomials; M_{inj} grows as T_{tank} ascends, when p_{nom} and ET are fixed. Particularly, as $p_{nom} = 800$ bar and $ET = 800 \mu s$ are employed, the difference in M_{inj} between the two fuel temperatures reach a value up to 3 mg. Moreover, the variation in the fuel temperature is often evidently greater, when the injection system is operating on the engine, than it is being tested at the test bench with T_{tank} ranging from 40 °C to 68 °C. On the other hand, the temperature variation significantly affects the fuel viscosity, and thus alters the injector dynamics [113].

Fig. 4.4 reports the curves of the injected mass flow-rate (G_{inj}) with respect to $p_{nom} = 1600$ bar and $ET = 600 \mu s$, while the fuel temperature (T_{tank}) are set as either 40 °C or 68 °C. As reported, the starts of injection (SOI) take place at the identical time instants and the injected flow-rates (G_{inj}) remain unchanged till the electrical command finishes. Whereas, the G_{inj} referring to the lower fuel temperature starts to decline around 0.1 ms earlier than that

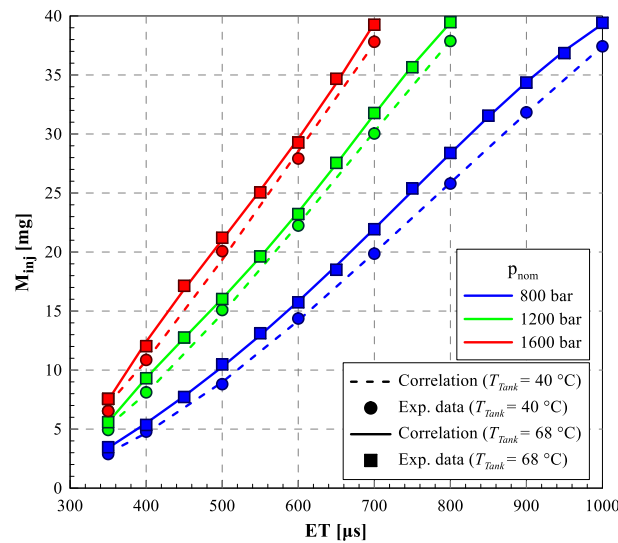


Figure 4.3: Injector characteristics $ET - M_{inj}$ for different p_{nom} and T_{tank} .

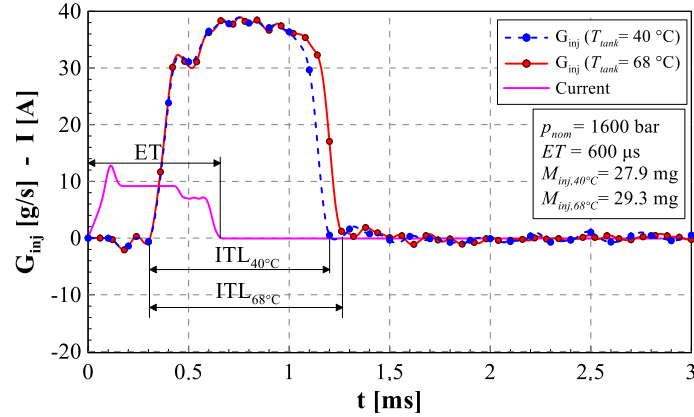


Figure 4.4: Influences of the fuel temperature on the injected mass flow-rate.

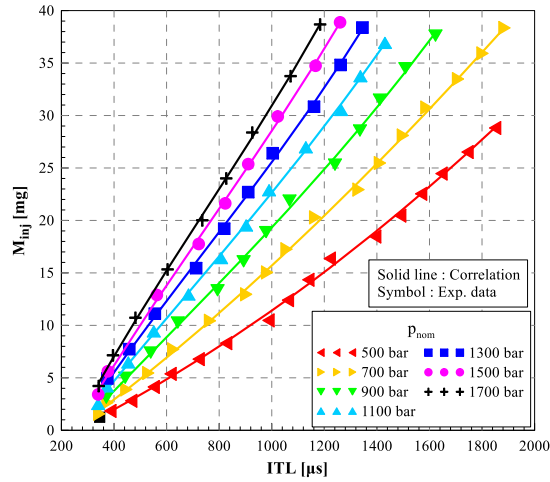


Figure 4.5: $ITL - M_{inj}$ for different p_{nom} and T_{tank} .

pertaining to the higher temperature. An analogous variation in the ends of injection (EOI) between the two injections is as well observed. Since ITL can be expressed as

$$ITL = EOI - SOI \quad (4.5)$$

it is obvious that the ITL as well as the injected fuel mass rise as the T_{tank} increases. Therefore, if the p_{nom} is fixed and the fuel temperature ascends, the correlation between the M_{inj} and the ET shifts, and this conclusion is in line with the results exhibited in Fig. 4.3.

The third order polynomial fitting of the $M_{inj} - ITL$ data for different p_{nom} are shown in Fig. 4.5. As can be observed, the correlation between the ITL and the M_{inj} generally remains, when T_{tank} changes from 40 °C to 68 °C. It

follows that $ITL - M_{inj}$ correlation is approximately independent of the fuel thermal regimes. This provides a possible solution to derive M_{inj} from the values of the p_{nom} and the ITL .

4.2.3 TFA sensor

Fig. 4.6 reports the G_{inj} , the p_{inj} and the energizing current for the working point of $p_{nom} = 1200$ bar and $ET = 600 \mu s$. All the exhibited traces have been dealt with the average filter over 100 consecutive engine cycles. As reported, before the injection event, no evident residual pressure waves can be observed in the hydraulic circuit. The p_{inj} thus remains approximately horizontal. As the energizing current is supplied, due to the opening of the pilot valve, a slight decrease in p_{inj} occurs. Immediately after the effective injection starts (SOI), an expansive pressure wave is formed, leading to a great reduction in p_{inj} (marked as 1 in Fig. 4.6). the triggered rarefaction waves are reflected at the common rail and transmit forward and backward along the rail-to-injector pipe, inducing the oscillations in the curve of $p_{inj} - t$. Although the pressure waves are gradually damped by the wall friction along the rail-to-injector pipe and by certain concentrated losses, the p_{inj} fluctuation amplitude retains evident over the injection event in Fig. 4.6. As soon as the effective injection finishes (at EOI), the needle closure results in a water hammer, shown as a sudden rise in p_{inj} (marked as 2 in Fig. 4.6).

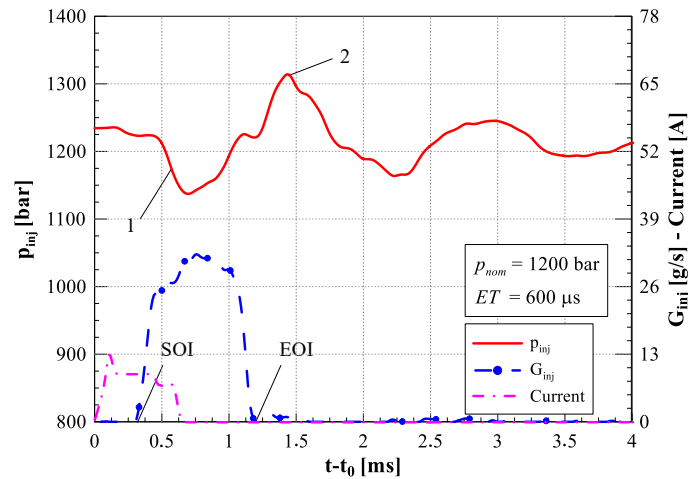


Figure 4.6: G_{inj} , p_{inj} and the current pertaining to $p_{nom} = 1200$ bar and $ET = 600 \mu s$.

The instants of vital changes in p_{inj} (cf. events 1 and 2 in Fig. 4.6) are related to certain hydraulic events (*SOI* and *EOI*). Whereas, an accurate evaluation of the exact time instant at which the reduction in p_{inj} linked to the *SOI* is not a simple task, since any pressure variation can influence the capture of the instant. Particularly, some pressure waves propagating along the rail-to-injector pipe can superpose with the key identification characteristics in p_{inj} , thus misleading the detection of the *SOI*.

As a useful tool, TFA can be employed to analyzing p_{inj} signals to extract the important information. Generally, *SOI* and *EOI* of one injection event are concentrated within a time length of 4 ms. In order to locate those instants by applying the TFA method and to avoid the leakage error pertaining to the start and the end of the signal, the trace of p_{inj} with a time length of 8 ms have been extract as the signal in which the *MIF* is determined. For a purpose of smoothening the p_{inj} curve, a Butterworth lowpass filter has been initially applied to the raw signal. The processed signal, namely $p_{inj,fil}$, substitutes $f(t)$ in Eq. (4.1). The Hanning window then has been chosen as the window function applied to Eq. (4.1):

$$h(n) = 0.5 \left(1 - \cos \left(2\pi \frac{n}{N} \right) \right), \quad 0 \leq n \leq N \quad (4.6)$$

where n is a discretized time instant within the window, and $N + 1$ stands for the number of the total samples contained by the signal. In the current work, the window length has been selected as 502 μ s. As the sample frequency is chosen as 500 kHz, N is thus equal to 250. By applying those variables, the STFT of p_{inj} is thus derived, and the *MIF* can be then calculated with Eqs. (4.2) and (4.4).

4.2.4 Results

Figs. 4.7-4.9 report the G_{inj} , the energizing currents and the *MIF* traces pertaining to three different operating conditions of p_{nom} and *ET* over a time length of 4 ms. In those graphs, due to the leakage errors, before the start of the electrical currents, the *MIF* curves take high values (above the upper border of the graphs). The first local maximum (marked as 1 in Figs. 4.7-4.9) is regarded as the effective start of the hydraulic injection. This time instant occurs approximately 0.15 ms after the effective time instant at which the

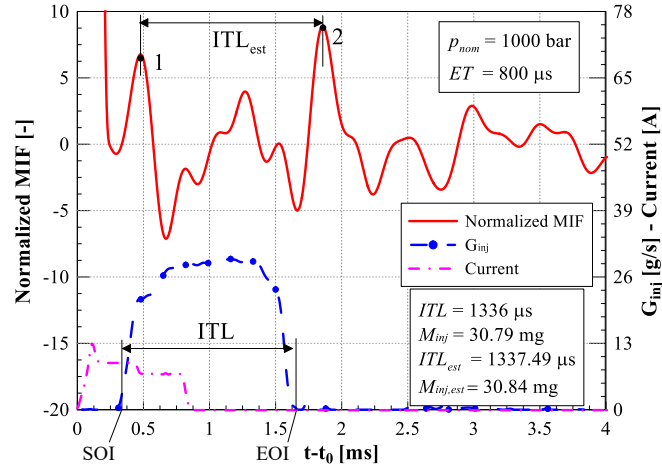


Figure 4.7: G_{inj} , p_{inj} and the normalized MIF ($p_{nom} = 1000$ bar and $ET = 800$ μ s).

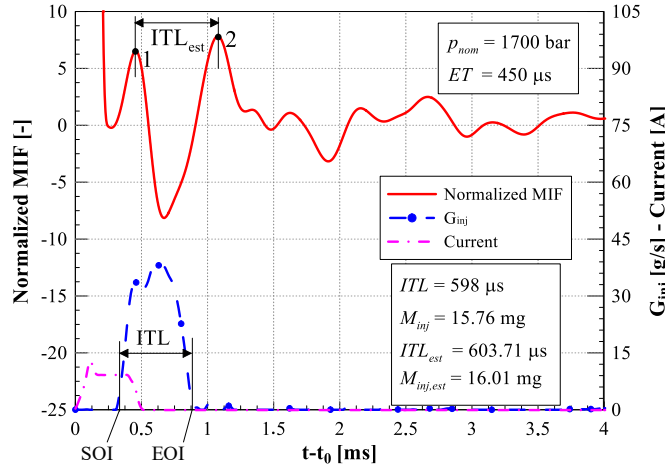


Figure 4.8: G_{inj} , p_{inj} and the normalized MIF ($p_{nom} = 1700$ bar and $ET = 450$ μ s).

nozzles open and the G_{inj} turn to be greater than zero (cf. Figs. 4.7 and 4.8). Such a time delay is essential for the injection triggered expansive wave propagate from the nozzle to location where the pressure transducer is mounted [70]. Similarly, the EOI linked instant, at which the overall maximum value of the MIF is found, takes place around 0.15 ms after the effective ending of the injection.

The predicted injection temporal length (ITL_{est}) and the authentic one, namely ITL , have been in turn computed by means of Eq. (4.5) with the corresponding experimental data. Since analogous time delays happen at both the start and the end of ITL_{est} with respect to ITL , ITL_{est} and ITL are

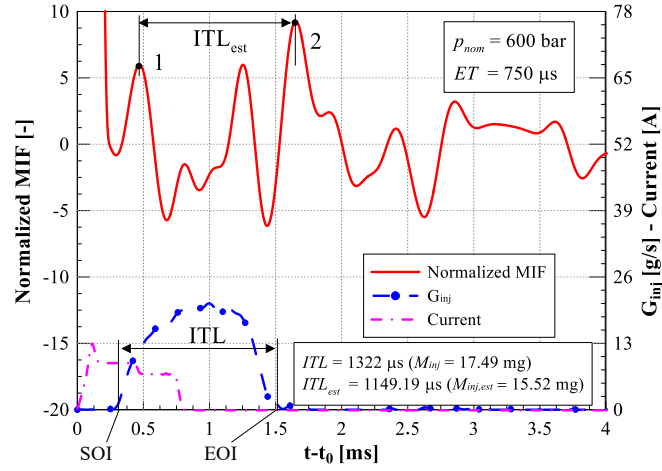


Figure 4.9: G_{inj} , p_{inj} and the normalized MIF ($p_{nom} = 600$ bar and $ET = 750$ μ s).

considered as coincident. As reported in the legends of Figs. 4.7 and 4.8, the differences between the ITL and the ITL_{est} are merely 1.49 μ s and 5.71 μ s with both the percentage errors below 1%.

Fig. 4.9 demonstrates the same variables as those reported in Figs. 4.7 and 4.8, but for the operating point of $p_{nom} = 600$ bar and $ET = 750$ μ s. Similarly, the estimated time instants connected to the SOI and the EOI , based on the MIF calculation, feature a time delay of about 0.15 ms compared to the authentic values. Whereas, on the basis of the G_{inj} traces, the difference between the ITL_{est} and the ITL is as high as 172.81 μ s, which is remarkable in the estimation work. This distortion can be ascribed to the superposition of the common rail reflected pressure waves and the nozzle closure triggered water hammer along the rail-to-injector pipe.

$M_{inj} - ITL$ curves, covering all the engine operating conditions, have been above fitted and plotted in Fig. 4.5. The ITL_{est} data obtained through Figs. 4.7 and 4.8 have been collected by the correlations exhibited in Fig. 4.5, and the estimated injected mass ($M_{inj,est}$), which are respectively 30.84 mg and 16.01 mg, have been in turn derived. The comparisons between the estimated and the HDA flowmeter evaluated genuine M_{inj} data have been performed, and the prediction errors are well below 0.5 mg, which is satisfactory. Whereas, if the case reported in Fig. 4.9 is considered, the $M_{inj,est}$ is 15.52 mg, and an error of 1.97 mg is found when compared to the M_{inj} provided by means of the HDA flowmeter.

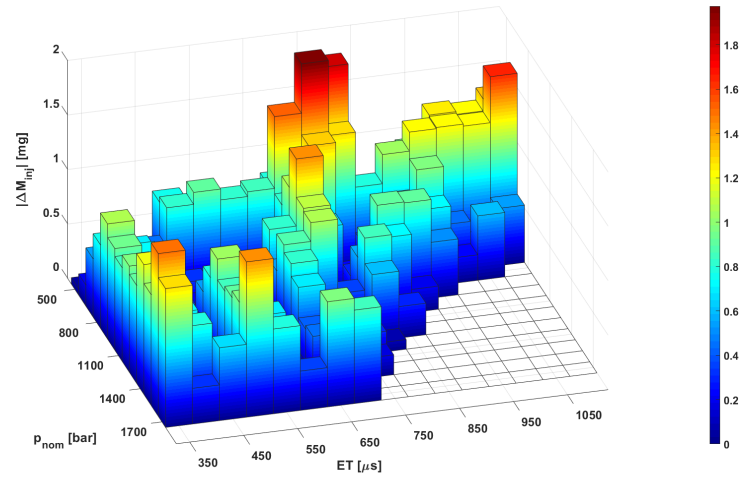


Figure 4.10: Accuracy of the estimated injected mass.

The estimated M_{inj} have been determined for large numbers of steady state operating conditions in terms of p_{nom} and ET by means of the TFA technique. The modulus of the error between the M_{inj} and the $M_{inj,est}$, which is the accuracy of the estimation ($|\Delta M_{inj}|$), has been computed and plotted in the 3D diagram of Fig. 4.10. In this plot, the fuel temperature in the tank T_{tank} has been fixed at 40 °C. The data of M_{inj} , as the averages of 100 consecutive engine cycles, were obtained by means of the HDA flowmeter. Since the injector was designed to expel less than 45 mg per engine cycle, the working conditions, which take both high values of p_{nom} and ET , have been excluded in the investigation.

In general, the accuracy is within 1.5 mg and below 1 mg over 80% of the tested operating conditions. In addition, the percentage error is within 7% and below 5% over 90% of the tested points. Meanwhile, the unsatisfactory predicted injected mass are concentrated within certain working zones. In particular, with respect to the operating points referring to either $500 \text{ bar} \leq p_{nom} \leq 600 \text{ bar}$ with medium ET values or $350 \mu\text{s} \leq ET \leq 450 \mu\text{s}$ with high p_{nom} values, the $|\Delta M_{inj}|$ can be found greater than 1.5 mg.

It is noteworthy that two parts can give the contribution to the error of $|\Delta M_{inj}|$. The first is the error due to the correlation. Although the fitting technology gives a generally satisfactory error, which is below 0.5 mg, this alteration is not ignorable with respect to state-of-the-art systems. On the

other hand, the second contribution, which is the primary one, is the error in the evaluation of ITL , due to the superposition of the pressure waves.

4.3 Physical equation based techniques

4.3.1 Control strategy and prototypal hardware

As the injected mass is real-time predicted, MATLAB Simulink was employed to establish the ECU software, which as well contains the standard control module of the p_{nom} and the ET . Starting from the system layout given by Fig. 4.2, the schematic of the prototypal hardware is reported in Fig. 4.11.

As far as the control strategy is concerned, the rail pressure is monitored every 5 ms by means of a Flexible ECU (from ETAS), and a processed signal, namely $p_{filter}(t)$, is generated (cf. H2 in Fig. 4.11). This signal is then compared to the value of the set p_{nom} , and the difference $e(t) = p_{nom} - p_{filter}(t)$ is thus derived and turns to be the input of R2 in Fig. 4.11. Such a block includes a PID controller, which eventually calculates the duty cycle of the PCV or of the FMV. In other words, block R2 (cf. Fig. 4.11) reproduces the standard closed-loop control of the fuel pressure in the common rail as a commercial ECU.

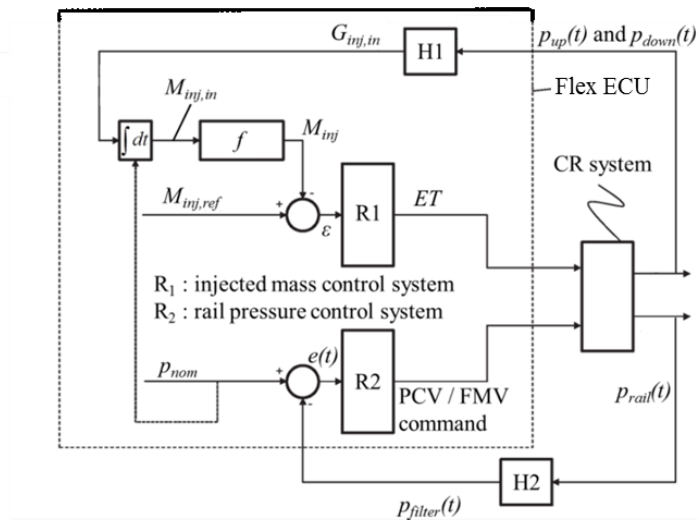


Figure 4.11: Injection system prototypal hardware.

The innovative part in the control strategy refers to the closed-loop of the injected mass. Captured by means of the piezoresistive pressure transducers (cf. Fig. 4.2) mounted on the rail-to-injector pipe, the pressure time distributions (p_{up} and p_{down}) are applied to the calculation of the injected mass (M_{inj}). If the nominal injected mass ($M_{inj,ref}$) is less than 5 mg, only one pressure trace, namely p_{down} is needed to estimated M_{inj} .

Under such circumstance, following Bosch method, similar to Eq. (2.7) in Sect. 2.2, the mass flow-rate at the injector inlet is initially evaluated based on the expression [105]:

$$G_{inj,in} = -A \int_0^t \frac{dp_{down}}{c} \quad (4.7)$$

where A is the internal cross-section area of the tube in which the p_{down} is measured, and c is the sound speed of the fluid.

On the other hand, if the $M_{inj,ref}$ is greater than 5 mg or pilot-main injections are considered, the $G_{inj,in}$ is derived through the following equation, which involves both p_{up} and p_{down} [114]:

$$G_{inj,in} = \frac{A}{l} \int_0^t \Delta p dt - \frac{A}{l} \langle \Delta p \rangle \cdot t \quad (4.8)$$

in which l is the pipe length between the two pressure sensors, $\Delta p = p_{up} - p_{down}$, and $\langle \Delta p \rangle$ stands for the time average of Δp over the entire evaluated signal trace per engine cycle. Both Eqs. (4.7) and (4.8) are included by the block H1 in Fig. 4.11. The obtained mass flow-rate $G_{inj,in}$ is then integrated over the time length between two optimized instants, namely t_i and t_f , the estimated injected mass is thus found:

$$M_{inj,in} = \int_{t_i}^{t_f} G_{inj,in} dt \quad (4.9)$$

It is reported in Fig. 4.12 that in all cases, the t_i corresponds to the time instant where the energizing current starts ($t_i = 0$), and t_f refers to the instant in the vicinity of the $G_{inj,in}$ maximum occurs. Furthermore, the pressure waves induced by the injection events can travel forward and backward along the rail-to-injector pipe, and the negative flow-rates in Fig. 4.12 thus can be observed. The contribution of those reverse flows has been well considered in Eq. (4.9), and does not distort the final estimation of the injected mass.

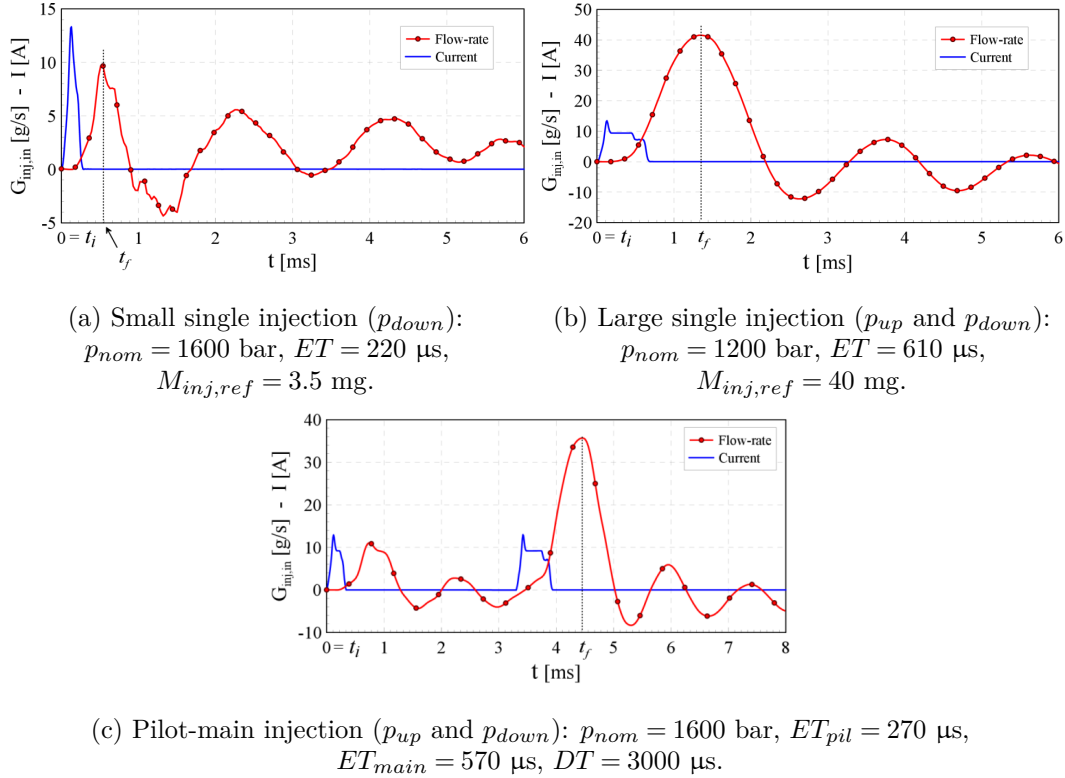
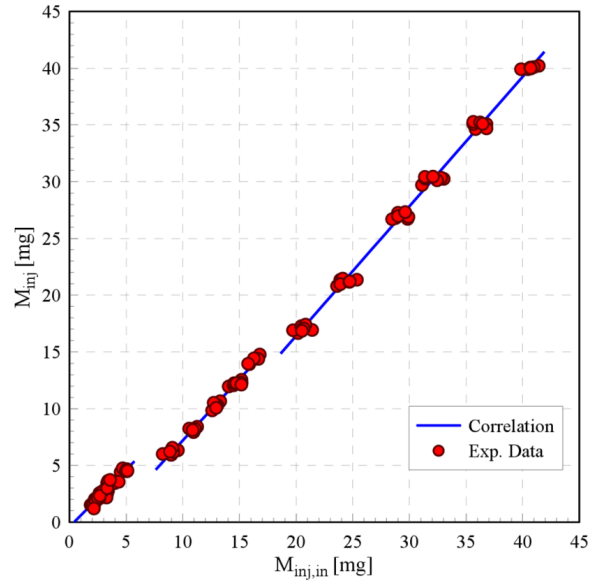


Figure 4.12: Time histories of the mass flow-rates at the injector inlet.

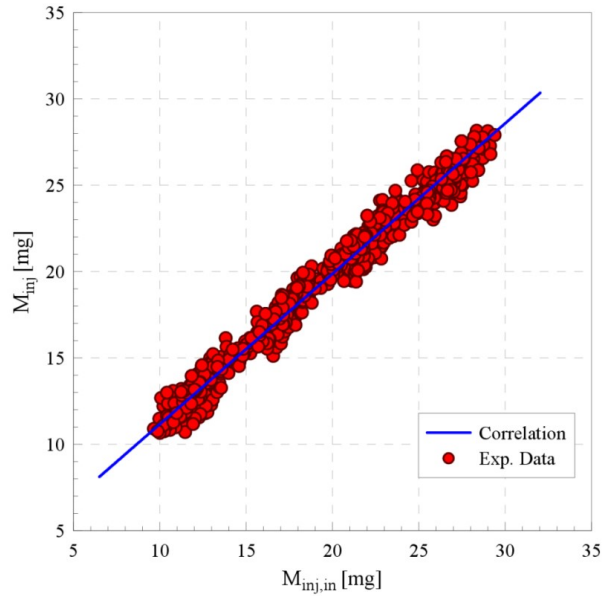
As the $M_{inj,in}$ has been calculated, this result ($M_{inj,in}$) can correlate well with the HDA flowmeter evaluated injected mass M_{inj} , and the correlations of single injections and of pilot-main injections are exhibited in Fig. 4.13. With respect to the correlation related to single injections, all tested points have been divided into small, medium and large injected quantities, while only one correlation has been employed for pilot-main injections.

The piecewise linear fitting lines for single injections are given in Fig. 4.13a, while the same line for pilot-main injections is reported in Fig. 4.13b. Those lines interpret a linear mathematical law $M_{inj} = f(M_{inj,in})$, and the application of those correlations in Fig. 4.13 provides the possibility to estimate M_{inj} in real time when the system is operating.

The error, between the authentic injected mass and the injected mass target applied to the ECU ($\varepsilon = M_{inj,ref} - M_{inj}$), is utilized as the input for a PID controller, which is contained by means of R1 in Fig. 4.11. Meanwhile, the R1 output refers to the modified energizing times supplied to the injector to correct the error in the injected mass in the next engine cycle.



(a) Single injections



(b) Pilot-main injections

Figure 4.13: Correlation between the $M_{inj,in}$ and the M_{inj} .

Eqs. (4.7)-(4.9) and the correlation $M_{inj} = f(M_{inj,in})$ have been implemented in a PXI (from NI) instrument (cf. Fig. 4.2), which takes the p_{up} and the p_{down} as the input data. The M_{inj} , as the output of the PXI, is fed to the Flexible ECU through a CAN interface cable, and the Flexible ECU thus can adjust the ET supplied to the solenoid injectors based on the error ε .

ETAS EHOOKS software has been employed to implement the control strategy in the Flexible ECU. The software of the CR system can be separated into two parts: 1) the basic software, generally offered by the supplier of the system, provides all basic variables; 2) the application software, in which the control strategies of p_{nom} and ET are included. The EHOOKS combines those two software. A single software package is then generated and uploaded to the Flexible ECU.

4.3.2 Results for single injections

All the tests reported in this section apply the CRI 2.20 indirect acting solenoid injector. All injected oil mass (M_{inj}) was evaluated for the working conditions of steady states referring to fixed p_{nom} and $M_{inj,ref}$ values, by means of the HDA flowmeter, as an average over 100 consecutive engine cycles. Meanwhile, the p_{rail} is controlled by means of FMV. The modulus of the error between the M_{inj} and $M_{inj,ref}$, which is $|\Delta M_{inj}|$, is exhibited in the

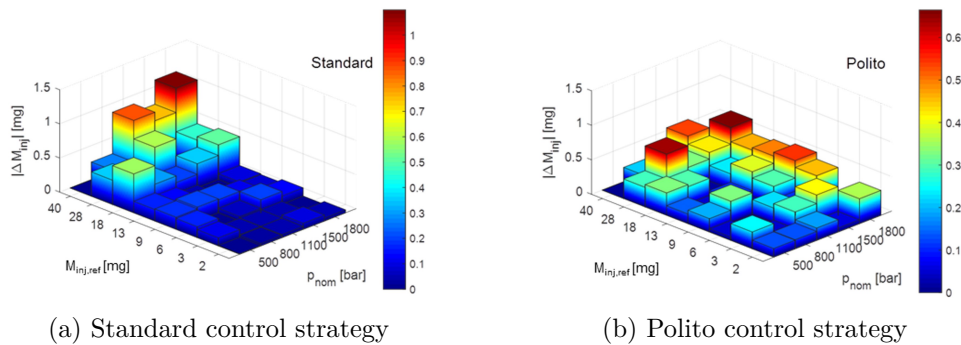


Figure 4.14: M_{inj} performance related to different control strategies ($T_{tank} = 40\text{ }^{\circ}\text{C}$).

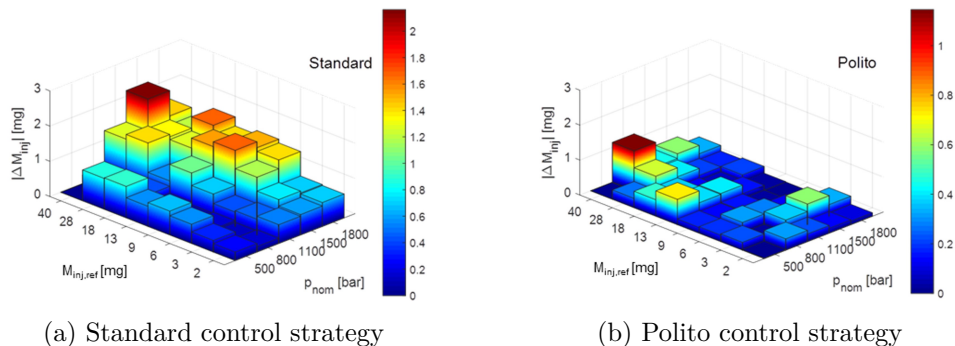


Figure 4.15: M_{inj} performance related to different control strategies ($T_{tank} = 68\text{ }^{\circ}\text{C}$).

3D diagram (cf. Fig. 4.14) as a function of p_{nom} and $M_{inj,ref}$. Figs. 4.14a and 4.14b respectively report the measured M_{inj} referring to the standard open-loop control strategy of M_{inj} and the same quantity for the innovative Polito closed-loop control strategy [115], under the condition of $T_{tank} = 40$ °C. It is noteworthy that the standard control system as well features a closed-loop control strategy of the fuel pressure in the common rail. Furthermore, the same performance related to $T_{tank} = 68$ °C are demonstrated in Fig. 4.15.

As can be observed, the accuracy of the M_{inj} is improved in both Figs. 4.14 and 4.15 as the closed-loop strategy of injected mass is activated. The maximum error $|\Delta M_{inj}|$ is smaller than 0.55 mg in Fig. 4.14b and is around 1 mg in Fig. 4.15b. However, the maximum error is greater than 1 mg in Fig. 4.14a and is larger than 2 mg in Fig. 4.15b for the standard case.

The injection system pertaining to the innovative closed-loop control strategy possesses a quite satisfactory performance under all explored operating conditions, and the accuracy is generally worsened as the T_{tank} passes from 40 °C to 68 °C for all cases. In particular the $|\Delta M_{inj}|$ ($\approx 1.5 - 2.2$ mg) evidently

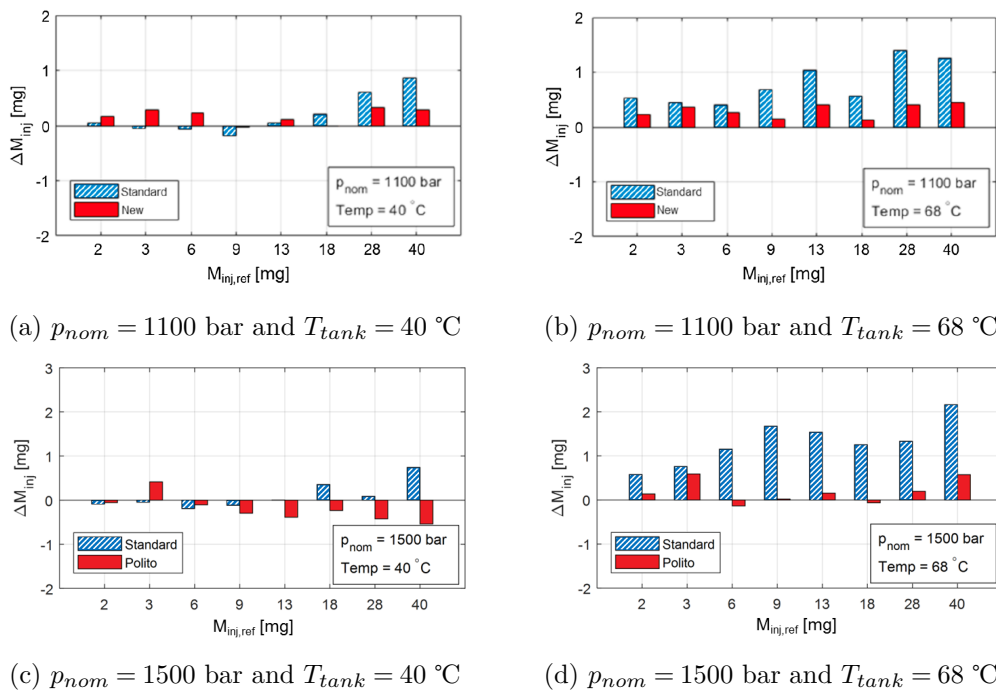


Figure 4.16: Comparison of the ΔM_{inj} performance for different p_{nom} and T_{tank} values.

turns to be larger in the standard system, while only a small deterioration can be found in the Polito system.

Fig. 4.16 reports some comparisons of the ΔM_{inj} values in the two systems under certain operating conditions included in Figs. 4.14 and 4.15. It is clear that the M_{inj} of the standard system for the CRI 2.20 injector takes higher values than required as the T_{tank} is equal to 68 °C, and this phenomenon becomes dramatic when the p_{nom} and $M_{inj,ref}$ take high values.

The dynamic performance of the innovative Polito strategy for one operating condition ($p_{nom} = 1600$ bar, $T_{tank} = 68$ °C and $M_{inj,ref} = 40$ mg) is shown in Fig. 4.17. The dashed curve refers to the estimated injected quantity per shot as a function of time, while the thick continuous curve reports a moving average of the dashed curve. This thick curve is evidently closer to the target value (thin continuous line) for the Polito system (right part in Fig. 4.17) than that for the original standard one (left part in Fig. 4.17). Meanwhile, immediately after the activation of the closed-loop control ($t \approx 10$ s), the thick curve approaches the target line, and the error in M_{inj} reduces sharply.

The commercial injector, applying the standard control strategy, is designed to obtain the optimum performance at a nominal T_{tank} value with an injected quantity of low to medium value. For instance, it can be 40 °C with $M_{inj,ref} \leq 15$ mg. Under such conditions, in Figs. 4.14a, 4.15a and 4.16, the standard open-loop strategy as well possesses satisfactory results.

The accuracy of M_{inj} for this injector with the standard control strategy generally worsens when the fuel at the injection nozzles increases, compared to the working conditions, where the performance is designed as optimum.

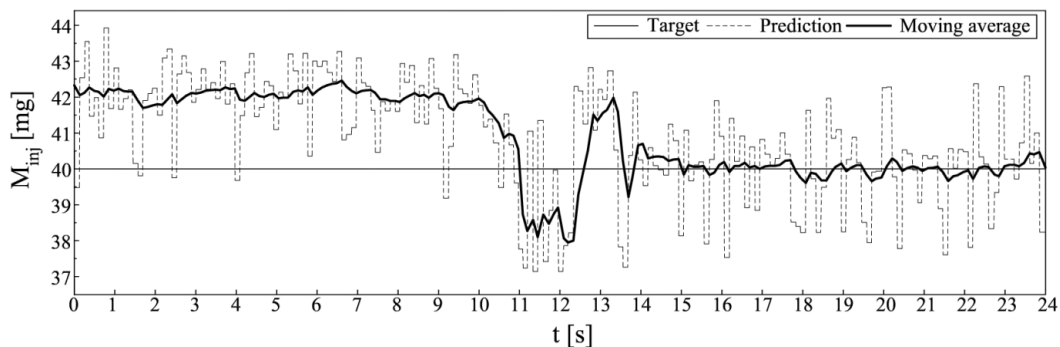


Figure 4.17: Performance of the estimated M_{inj} when the closed-loop strategy is activated ($p_{nom} = 1600$ bar, $T_{tank} = 68$ °C and $M_{inj,ref} = 40$ mg).

Meanwhile, it is clear that the temperature around the nozzles augments with the T_{tank} . Moreover, the higher either p_{nom} or $M_{inj,ref}$ is, the greater the amount of fuel throttling through the injector. Similarly, a higher final temperature of the injected fuel is thus obtained. The newly established control strategy is sensitive to the influence of the in-nozzle fuel temperature. As this temperature is varied, the $M_{inj,in}$ is in turn modified and is then read by the ECU. In addition, the $M_{inj,in} - M_{inj}$ correlation has been verified to be independent of the fuel temperature over $18\text{ }^\circ\text{C} < T_{tank} < 68\text{ }^\circ\text{C}$.

The disturbance given by the in-injector fuel temperature on the injection performance is a well-known problem for engine calibration specialists and is responsible for the differences in the injector calibration maps applied at the engine dynamometer cell and at the hydraulic test bench. In general, these maps are the lookup tables stored in the ECU that provides the links between $M_{inj,ref}$, p_{nom} and ET .

Tab. 4.1 demonstrates the evaluated injected mass at the hydraulic test bench under the standard open-loop control strategy, while the lookup table referring to $M_{inj,ref} = f(p_{nom}, ET)$ was calibrated at the dynamometer cell. As the identical $T_{tank}(= 40\text{ }^\circ\text{C})$ value is provided, the error between the injected quantity and its target (the first row in Tab. 4.1) augments with the value of either p_{nom} or $M_{inj,ref}$, and can approximately reach 9.5 mg. The injection system under such condition has been found to inject less fuel than the target. In fact, the M_{inj} , with respect to certain p_{nom} and ET , rises as the in-nozzle fuel temperature increases. In addition, the map is calibrated to obtain the optimum performance as the engine was operating at the dynamometer cell, where the injected fuel temperature can be significantly higher than that at the hydraulic test bench. These data in Tab. 4.1 thus agrees better with the working conditions in Fig. 4.16 with $T_{tank} = 68\text{ }^\circ\text{C}$. Whereas, the errors $|\Delta M_{inj}|$ are greater in Tab. 4.1 than those in Fig. 4.16, since the in-nozzle fuel temperature at the dynamometer cell is even higher than that occurs at the maximum T_{tank} value set in the hydraulic test rig. Therefore, if the innovative Polito strategy is applied to an engine, more significant benefits, in terms of the accuracy of M_{inj} , than those obtained in the above mentioned tests at the hydraulic test bench are expected.

It is noteworthy that an accurate open-loop compensation of the injected mass, as a function of the thermal regime of the engine, is quite difficult to obtain,

Table 4.1: Injected mass measured at the hydraulic test rig with the lookup table calibrated at the dynamometer cell.

p_{nom} [bar]	2 mg	3 mg	6 mg	9 mg	13 mg	18 mg	28 mg	40 mg
500	1	1.9	4.3	6.5	10.3	14.5	23.6	35.5
800	0.8	1.4	4.4	6.8	9.9	13.9	23.6	34.7
1100	0.7	1.3	3.3	5.3	9.2	13	22.1	33.8
1500	0.5	1.2	2.6	3.9	6.5	11.6	20.8	32.3
1800	0.3	1	2.8	4.1	5.7	10.1	20.7	31.4

since the in-nozzle fuel temperature inside of the combustion chamber is as well influenced by the passed speed and load history of the engine. This history is irregularly varied with respect to time, and it is problematic to establish an accurate open-loop strategy, on the basis of operating point and engine coolant temperature, to compensate the variation in the injected quantity.

Fig. 4.18 exhibits the coefficient of variation of the injected mass, evaluated over 100 consecutive engine cycles, by means of the HDA flowmeter, at fixed operating conditions of p_{nom} , $M_{inj,ref}$ and engine speed ($p_{nom} = 1100$ bar or $p_{nom} = 1500$ bar with an engine speed of 2000 rpm) for both $T_{tank} = 40$ °C and

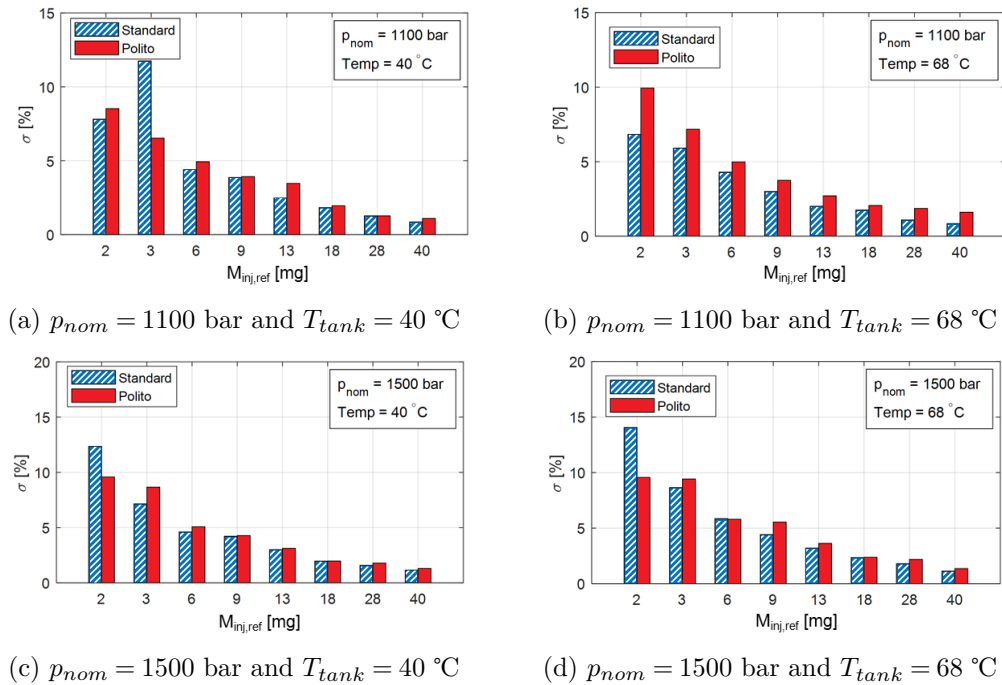


Figure 4.18: Coefficient of variation in the M_{inj} for different p_{nom} and T_{tank} values.

$T_{tank} = 68 \text{ }^\circ\text{C}$. As can be observed, in all reported cases, the Polito system, endowed with the closed-loop control strategy of the injected mass, possesses comparable precision as that measured in the standard system. In fact, the stringent tolerances adopted to manufacture the CRI 2.20 injectors and the integration of the Minirail improve significantly the stability in the injected mass. To improve this performance is thus a challenging task. In fact, as reported in Fig. 4.18, the dosage precision is not enhanced when the closed-loop strategy is equipped.

Fig. 4.19 reports the test results for the dynamic response in p_{nom} and $M_{inj,ref}$ at the hydraulic rig for both $T_{tank} = 40 \text{ }^\circ\text{C}$ and $T_{tank} = 68 \text{ }^\circ\text{C}$. At a constant engine speed, this system is capable to respond to a sudden change in the engine load, realized by means of modifications in p_{nom} and $M_{inj,ref}$. As can be observed, the Polito system achieves a better dynamic response than the standard system. Both the systems can reach the new injected mass state rapidly, while the Polito system is able to realize an improved accuracy. Moreover, Fig. 4.20 proves that a similar outcome as that reported in Fig. 4.19 is obtained, if ramps in p_{nom} and $M_{inj,ref}$ are provided at the hydraulic test rig.

In short, the dynamic experiments reported in Figs. 4.19 and 4.20 emphasize that the Polito closed-loop control strategy of the injected mass is capable to reply to the transient injection variables with improved performance, and this characteristic could be exploited to enhance engine performance in the emission cycles, which features significant transient states.

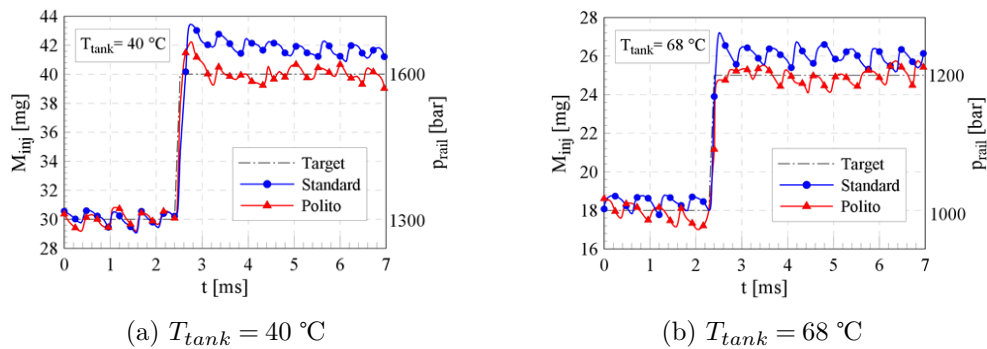


Figure 4.19: Dynamic response to steps in p_{nom} and $M_{inj,ref}$ values.

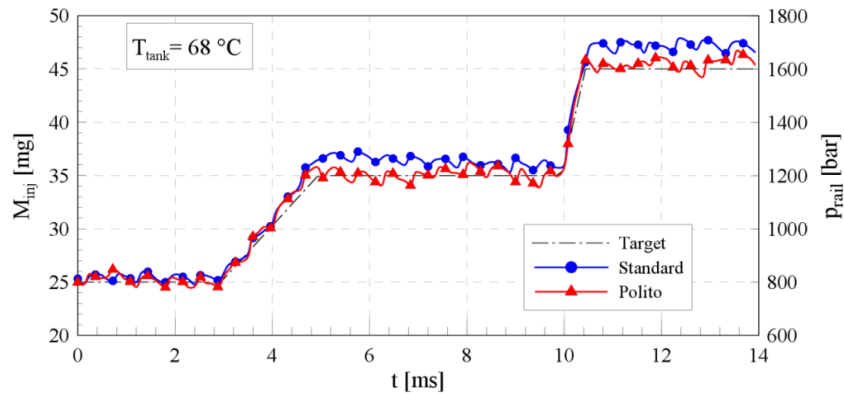


Figure 4.20: Dynamic response to ramps in p_{nom} and $M_{inj,ref}$ values.

4.3.3 Results for pilot-main injections

All the tests reported in this section apply the CRI 2.18 indirect acting solenoid injector. Fig. 4.21 exhibits the injected mass of pilot-main injections, as a function of DT , for fixed nominal pressure (p_{nom}), reference pilot injection mass ($M_{pil,ref}$) and reference main injection mass ($M_{main,ref}$) with the standard open-loop control strategy. Since it is not a closed-loop control of the injected mass, the energizing times (ET_{pil} and ET_{main}) are fixed based on the injected mass reference. It can be observed that the $M_{inj}(=M_{pil}+M_{main})$

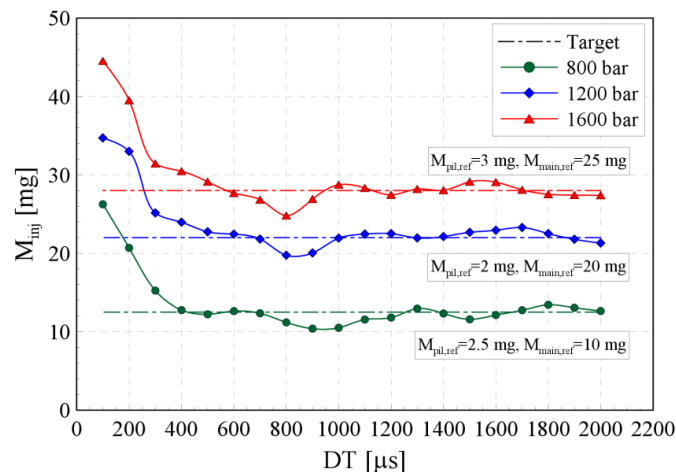


Figure 4.21: Pilot-main injected mass as a function of p_{nom} and DT with the standard system.

risers monotonically as the DT is reduced below $400 \mu\text{s}$. Such a phenomenon obviously anomalously increase the injected mass, compared with the mass target $M_{inj,ref} = M_{pil,ref} + M_{main,ref}$ (dashed-dotted lines in Fig. 4.21), due to the hydraulic interference that the pilot injection exerts on the main injection [116]. Similarly, the analogous curve patterns, which are not reported for the sake of conciseness, can be obtained for the CRI 2.20 injectors.

When the DT is lower than the critical dwell time, which has been elaborated in Sect. 3.3.1, the M_{inj} is quite sensitive to minor changes in the hydraulic

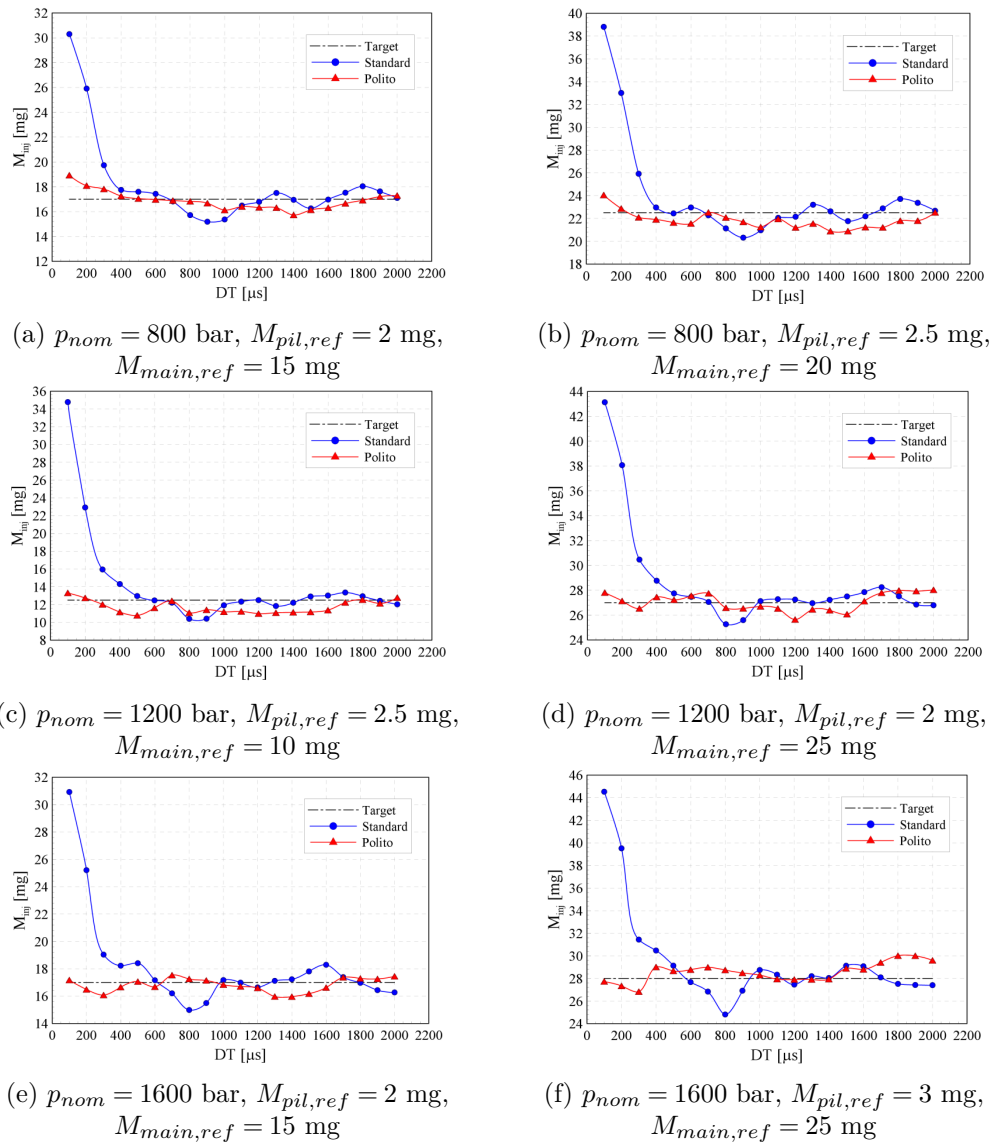


Figure 4.22: DT sweeps.

dwelling time, due to cycle-to-cycle dispersion in the needle lift time histories of the pilot injection and of the main shot. Although the influence of this variation can be acceptable in the injected amount of fuel at the hydraulic test bench [35], the consequences turn to be dramatic in the coefficient of variation of indicated mean effective pressure, as this injector is mounted on an engine.

Under the condition of $T_{tank} = 40$ °C, large amount of tests, in which the value of DT is swept with different fixed p_{nom} , $M_{pil,ref}$ and $M_{main,ref}$ values, have been carried out at the hydraulic test rig. Among those, a few results in terms of the injected mass are reported in Fig. 4.22. The investigated total injected fuel mass M_{inj} was evaluated by means of the HDA flowmeter, as an average over 100 consecutive engine cycles, and the fuel pressure in the common rail is controlled by means of FMV.

The Polito system is capable to control the accuracy of the injected mass in the pilot-main injections within 2 mg, over the entire DT range. In particular, the anomalous rise of the M_{inj} within the range of $DT < 400$ μ s disappears, while this problem remains in all cases applying the standard system.

In short, the newly developed closed-loop control strategy of the injected mass could be applied to the ECU of commercial CR diesel engines, in order to improve the instability in the indicated mean effective pressure, which occurs within short dwelling time range of the energizing current signal.

Chapter 5

Fanno flow approximated in polytropic process

5.1 Analytical relations for polytropic flows

A polytropic process, governed by Eq. (5.1), presents a link between the fluid pressure p and its density ρ with the help of a polytropic exponent m .

$$\frac{dp}{p} - m \frac{d\rho}{\rho} = 0 \quad (5.1)$$

As long as the relation in Eq. (5.1) holds under one circumstance, when investigating viscous flow patterns along a constant area pipe, the steady-flow energy equation generally employed in the analysis of Fanno flow should be discarded. Following similar approaches as the formulations of Fanno flow, Eq. (5.1) is coupled with perfect gas state equation (Eq. (5.2)), continuity equation (Eq. (5.3)), momentum equation (Eq. (5.4)), equation of isentropic stagnation pressure p_0 (Eq. (5.5)) and of isentropic stagnation pressure T_0 (Eq. (5.6)), the definition of isentropic Mach number Ma (Eq. (5.7)), the impulse function (Eq. (5.8)) and the change in entropy s between points x and y (Eq. (5.9)), in their suitable differential forms [84],

$$\frac{dp}{p} = \frac{d\rho}{\rho} + \frac{dT}{T} \quad (5.2)$$

$$\frac{d\rho}{\rho} + \frac{du^2}{2u^2} = 0 \quad (5.3)$$

$$-Adp - \tau_w dA_w = Gdu \quad (5.4)$$

$$\frac{dp_0}{p_0} = \frac{dp}{p} + \frac{\gamma Ma^2}{2 + (\gamma - 1) Ma^2} \cdot \frac{dMa^2}{Ma^2} \quad (5.5)$$

$$\frac{dT_0}{T_0} = \frac{dT}{T} + \frac{(\gamma - 1) Ma^2}{2 + (\gamma - 1) Ma^2} \cdot \frac{dMa^2}{Ma^2} \quad (5.6)$$

$$\frac{dMa^2}{Ma^2} = \frac{du^2}{u^2} - \frac{dT}{T} \quad (5.7)$$

$$\frac{dJ}{J} = \frac{dp}{p} + \frac{\gamma Ma^2}{1 + \gamma Ma^2} \cdot \frac{dMa^2}{Ma^2} \quad (5.8)$$

$$s_y - s_x = C_p \cdot \ln \frac{T_{0,y}/T_{0,x}}{(p_{0,y}/p_{0,x})^{\frac{\gamma-1}{\gamma}}} \quad (5.9)$$

where T , u , A , τ_w , A_w , G , γ , J and C_p respectively stand for flow temperature, flow velocity, hydraulic cross-section, shearing stress exerted on the stream by the walls, wetted wall area on which the shearing stress τ_w acts, mass flow-rate of the stream, isentropic exponent, the impulse and the heat capacity at constant pressure.

Substituting the definitions of friction factor f and of hydraulic diameter D , which are listed in Eqs. (5.10) and (5.11), into Eq. (5.4),

$$f \equiv \frac{\tau_w}{\rho u^2/2} \quad (5.10)$$

$$D \equiv 4 \frac{A}{dA_w} dx \quad (5.11)$$

After some algebraic manipulations among Eqs. (5.1)-(5.9), eight differential variables dp/p , $d\rho/\rho$, du/u , dT/T , dMa^2/Ma^2 , dp_0/p_0 , dT_0/T_0 , dJ/J and ds (cf. Eq. (5.12)) can be expressed as expressions combined with the term of $4fdx/D$, which is treated as independent. Those differential equations are capable to describe any viscous flow following a polytropic process, as long as no shock is present.

$$\left\{ \begin{array}{l}
\frac{dMa^2}{Ma^2} = -\frac{(m+1)Ma^2}{2(Ma^2 - m/\gamma)} \cdot \frac{4fdx}{D} \\
\frac{dp}{p} = \frac{Ma^2 m}{2(Ma^2 - m/\gamma)} \cdot \frac{4fdx}{D} \\
\frac{d\rho}{\rho} = \frac{Ma^2}{2(Ma^2 - m/\gamma)} \cdot \frac{4fdx}{D} \\
\frac{du}{u} = -\frac{Ma^2}{2(Ma^2 - m/\gamma)} \cdot \frac{4fdx}{D} \\
\frac{dT}{T} = \frac{(m-1)Ma^2}{2(Ma^2 - m/\gamma)} \cdot \frac{4fdx}{D} \\
\frac{dp_0}{p_0} = \frac{mMa^2}{2(Ma^2 - m/\gamma)} \left[1 - \frac{\gamma \frac{(m+1)}{m} Ma^2}{2 + (\gamma - 1) Ma^2} \right] \frac{4fdx}{D} \\
\frac{dT_0}{T_0} = \frac{mMa^2}{2(Ma^2 - m/\gamma)} \left[\left(1 - \frac{1}{m} \right) - \frac{(\gamma - 1) \frac{(m+1)}{m} Ma^2}{2 + (\gamma - 1) Ma^2} \right] \frac{4fdx}{D} \\
\frac{dJ}{J} = \frac{mMa^2}{2(Ma^2 - m/\gamma)} \left[1 - \frac{\gamma \frac{(m+1)}{m} Ma^2}{1 + \gamma Ma^2} \right] \frac{4fdx}{D} \\
ds = C_v \frac{m - \gamma}{2} \cdot \frac{Ma^2}{Ma^2 - m/\gamma} \cdot \frac{4fdx}{D}
\end{array} \right. \quad (5.12)$$

The flow expressed in Eq. (5.12) results to be choked when $Ma^2 = m/\gamma$ instead of $Ma^2 = 1$, which holds with respect to isentropic flows. Indeed, it can be seen in the formulations that all the logarithmic differential variables change their signs when this $Ma^2 = m/\gamma$ is crossed starting from either a subsonic or a supersonic flow. Furthermore, since the heat transfer with the pipe walls can take place in the polytropic flow, the stagnation temperature possibly varies along the duct. Finally, it is worthy to observe that when $m = 1$, Eq. (5.12) becomes the isothermal flow formulations obtained in [84], and the consistency is thus proved.

In order to obtain the formulas desired for practical calculations, the Mach number Ma is then regarded as the independent variable. The formula that links Ma and $4fdx/D$ in Eq. (5.12) is thus integrated over the duct length by assuming that the flow at the outlet of the duct is choked ($Ma^2 = m/\gamma$). As the integration form of $4fL/D$ has been obtained, substituting this result into other formulas in Eq. (5.12), all other equations can be as well integrated, and the final results are expressed as

$$\left\{ \begin{array}{l}
4f \frac{L_{max}}{D} = \frac{2}{m+1} \left[\ln \left(\frac{\gamma}{m} Ma^2 \right) + \frac{m - \gamma Ma^2}{\gamma Ma^2} \right] \\
\frac{p}{p^*} = \left(\frac{\gamma}{m} Ma^2 \right)^{-\frac{m}{m+1}} \\
\frac{\rho}{\rho^*} = \left(\frac{\gamma}{m} Ma^2 \right)^{-\frac{1}{m+1}} \\
\frac{u}{u^*} = \left(\frac{\gamma}{m} Ma^2 \right)^{\frac{1}{m+1}} \\
\frac{T}{T^*} = \left(\frac{\gamma}{m} Ma^2 \right)^{-\frac{m-1}{m+1}} \\
\frac{p_0}{p_0^*} = \left(\frac{\gamma}{m} Ma^2 \right)^{-\frac{m}{m+1}} \cdot \left(\frac{1 + \frac{\gamma-1}{2} Ma^2}{1 + \frac{\gamma-1}{2} \cdot \frac{m}{\gamma}} \right)^{\frac{\gamma}{\gamma-1}} \\
\frac{T_0}{T_0^*} = \left(\frac{\gamma}{m} Ma^2 \right)^{-\frac{m-1}{m+1}} \cdot \left(\frac{1 + \frac{\gamma-1}{2} Ma^2}{1 + \frac{\gamma-1}{2} \cdot \frac{m}{\gamma}} \right) \\
\frac{J}{J^*} = \left(\frac{\gamma}{m} Ma^2 \right)^{-\frac{m}{m+1}} \cdot \frac{1 + \gamma Ma^2}{1 + m} \\
s^* - s = C_v \frac{m - \gamma}{m + 1} \cdot \ln \left(\frac{\gamma}{m} Ma^2 \right) \quad (s^* = s_{max})
\end{array} \right. \quad (5.13)$$

in which L_{max} is a possible maximum pipe length, and the variables with an asterisk superscript stand for their corresponding values at the duct location where the flow is choked. Eq. (5.13) exhibits the relations between the flow properties at the pipe inlet and the corresponding ones at the duct outlet where the flow is choked. Meanwhile, the formula at the left sides of the equations in Eq. (5.13) turn to be algebraic functions of only the initial Mach number along a duct. Furthermore, as elaborated for classic Fanno flow in [84], since $4fL_{max}/D$ is a function only of Ma , the length of the duct L , over which Ma_x is transferred into Ma_y , can be calculated in Eq. (5.14). It follows that Eq. (5.13) can be generalized to compute the any polytropic flow with friction when the Mach numbers at the duct inlet and outlet are known.

$$4f \frac{L}{D} = \left(4f \frac{L_{max}}{D} \right)_{Ma_x} - \left(4f \frac{L_{max}}{D} \right)_{Ma_y} \quad (5.14)$$

5.2 Comparison between the polytropic and the classic Fanno flows

Following the above-mentioned analytical expressions and the classic Fanno flow equations elaborated in [84], comparisons between polytropic flow with

friction along a constant cross-section duct and classic Fanno flow have been carried out.

Classic Fanno flow cases are firstly tested. With respect to subsonic flow, the duct maximum length $L_{max,Fanno}$, the pipe diameter D as well as the isentropic exponent γ ($= 1.4$) are initially set. Meanwhile, a constant friction factor f is selected as 0.003 in all cases, since it is a reasonable value with respect to the turbulent flows within both the supersonic and the subsonic regimes [117]. The stagnation temperature T_0 and pressure p_0 are fixed at the inlet, and an ambient pressure p_{out} is selected at the outlet. Combining those fixed parameters according to [84], the corresponding Mach numbers at both extremities of the duct can be obtained. Whereas when the flow is choked at the duct outlet, it is evident that the pressure at the pipe exit does not decrease to the ambient value, but it reaches the value of p^* , as described in [84]. On the other hand, in the supersonic cases, taken into consideration the state equations, all flow properties at the pipe inlet are fixed as the inlet boundary condition. Meanwhile, the pipe length is fixed in order to guarantee that the duct outlet Mach number is greater than 1 in classic method and is greater than $\sqrt{m/\gamma}$ in polytropic method. Therefore, no shock is present. Knowing the Mach numbers, all flow properties along the duct can be subsequently solved.

As the polytropic flow with friction is considered, a constant polytropic exponent m is selected, by simply applying the polytropic evolution relation reported in Eq. (5.15) to the classic Fanno flow states at the duct extremities, in order to retain an analogous thermodynamic process along the duct.

$$m = \frac{\ln(p_{in}/p_{out})}{\ln(\rho_{in}/\rho_{out})} \quad (5.15)$$

Subsequently, the f , the D and the Ma at both duct ends found in the corresponding classic Fanno flow case are applied to Eqs. (5.13) and (5.14). A new pipe length $L_{pol.}$ is obtained and in turn employed to compute all other flow properties along the duct. Meanwhile, it is observed that the boundary conditions originally set in the classic Fanno flow is as well automatically fit in the polytropic case.

Figs. 5.1-5.4 present four investigated comparison cases under either supersonic or subsonic condition. The examined cases cover all possible continuous flow patterns that could occur. Among those figures, since the duct length applied to the polytropic method is modified, all pipe lengths are normalized

into 1, and the abscissa shown in Figs. 5.1-5.4 thus becomes the quotient of original space coordinate divided by the corresponding pipe length.

The first set of comparison in p , Ma , T , T_0 and u , demonstrated in Fig. 5.1, has been performed in the case under the conditions of $p_0 = 1$ bar, $T_0 = 400$ K, $p_{out} = 0.6$ bar and $L_{max,Fanno} = 80$ m. In this case, the pipe length of the polytropic flow $L_{max,pol.} \approx 80.28$ m, which is quite similar to $L_{max,Fanno}$. Meanwhile, the polytropic exponent $m \approx 1.17$. The Mach number (the continuous curve with rhombus symbols and the continuous curve) pertaining to both flows in Fig. 5.1 at the right boundary, which is the pipe outlet, are below $\sqrt{m/\gamma}$. Under such circumstances, in terms of both flow patterns, the pressure at the outlet are fixed at an identical value. Furthermore, it can be found in Fig. 5.1 that at the two pipe extremities all flow properties pertaining to those two analytical methods coincide, and naturally the trends of the properties for those two flows are generally analogous, except for the total temperature evolution. However, along the duct, none of selected properties in the polytropic flow repeats the trace pertaining to the same variable in the classic Fanno flow, although the differences between two same properties are quite small. The

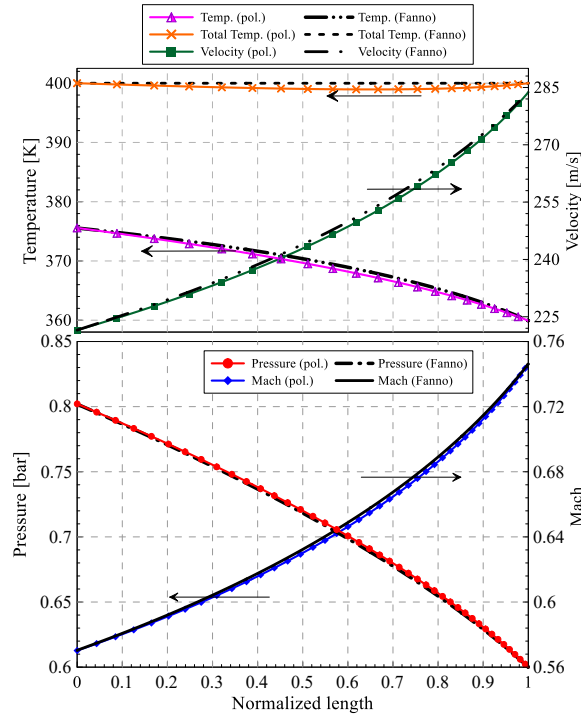


Figure 5.1: The comparison between the polytropic and the classic flows ($p_0 = 1$ bar, $T_0 = 400$ K, $p_{out} = 0.6$ bar, $L_{max,Fanno} = 80$ m)

maximum error in percentage in the polytropic flow can be found in the u (the continuous curve with square symbols in Fig. 5.1), and the value is 0.51%. Meanwhile, based on the curve of total temperature, it is inferred that through the polytropic flow, the system is no longer adiabatic, but initially expels heat and finally absorbs the same amount of heat. Nonetheless, the Fanno flow under this condition is interpreted by means of the polytropic flow with a satisfactory accuracy degree.

The second comparison, considering a choked subsonic flow ($p_0 = 1$ bar, $T_0 = 400$ K, $p_{out} = 0.3$ bar, $L_{max,Fanno} = 40$ m), is reported in Fig. 5.2. In this test, $L_{max,pol.} \approx 41.34$ m and $m \approx 1.28$. Compared to Fig. 5.1, the difference between $L_{max,pol.}$ and $L_{max,Fanno}$ is increased and m becomes closer to γ . In the polytropic flow, one evident discrepancy between the polytropic flow and the Fanno flow is that the Ma (the continuous curve with rhombus symbols in Fig. 5.2) does not arrive at 1, since the choking condition for the polytropic flow occurs at the Mach number $\sqrt{m/\gamma}$, and m , determined by means of the polytropic process between the inlet and the outlet of the Fanno flow, is not equal to γ . Therefore, the fluid properties at the duct outlet in the

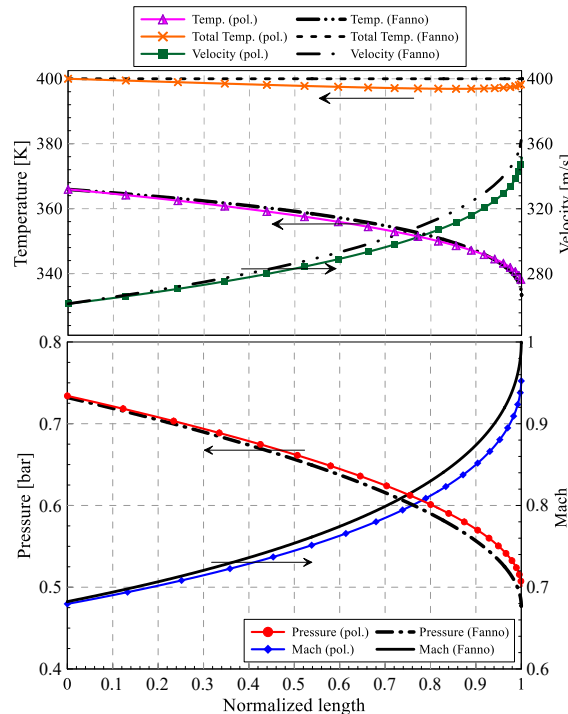


Figure 5.2: The comparison between the polytropic and the classic flows ($p_0 = 1$ bar, $T_0 = 400$ K, $p_{out} = 0.3$ bar, $L_{max,Fanno} = 40$ m)

polytropic flow form a new balance differed from that in the Fanno flow, albeit the polytropic processes are alike. None of the p , Ma and u in the polytropic flow at the right boundary returns to the corresponding values in the Fanno flow, and a maximum difference of 5.1% occurs in the p (the continuous curve with dot symbols and the dashed-dotted curve with narrow space in Fig. 5.2) at the 75% of the duct length. Similar to the case shown in Fig. 5.1, it can be observed that from the inlet to the outlet that in the total temperature (the continuous curve with cross symbols and the dashed line in Fig. 5.2) the stream rejects heat at the beginning and subsequently some heat is added. Whereas, the final added heat quantity cannot recover the previously lost amount, and at the end, 0.35% of the difference in T_0 remains. Furthermore, simultaneously with the change in the T_0 , the temperature of the stream (the continuous line with triangle symbols in Fig. 5.2) is firstly smaller than that in the Fanno flow then turns to be greater.

The comparisons under supersonic conditions are reported in Fig. 5.3 ($p_0 = 5.57$ bar, $T_0 = 900$ K, $u_{in} = 1000$ m/s, $L_{max,Fanno} = 35$ m) and Fig. 5.4 ($p_0 = 5.57$ bar, $T_0 = 1000$ K, $u_{in} = 1000$ m/s, $L_{max,Fanno} = 60.15$ m). In Fig. 5.3 $L_{max,pol.} \approx 34.7$ m and $m \approx 2.72$, while in Fig. 5.4, $L_{max,pol.} \approx 62.3$ m and $m \approx 1.93$. Combining the results obtained through Figs. 5.1 and 5.2, it is inferred that if the Mach number approaches 1 in the Fanno flow, $L_{max,pol.}$ tends to possess greater difference from $L_{max,Fanno}$. It is similar to Fig. 5.1 that in Fig. 5.3 all flow properties following polytropic method start and end at the identical values as those in the Fanno flow, and in both flows, those properties basically follow the analogous trends. What is different is that in the supersonic case, along every two traces pertaining to the same property, the maximum error between them is times greater. The maximum error occurs in p (the continuous curve with dot symbols in Fig. 5.3) reaches 5.5%, and all the errors pertaining to the other properties are above 1%.

On the other hand, similar characteristics as Fig. 5.2 is shown in Fig. 5.4, which refers to The supersonic Fanno flow with outlet $Ma = 1$ and its corresponding polytropic flow. The properties in the polytropic flow cannot come back to those in the Fanno flow at the duct outlet, even though the polytropic process is characterized by the fluid states between the inlet and the outlet in the Fanno flow. Moreover, greater difference between the fluid properties pertaining to the two flows are shown in Fig. 5.4. The maximum

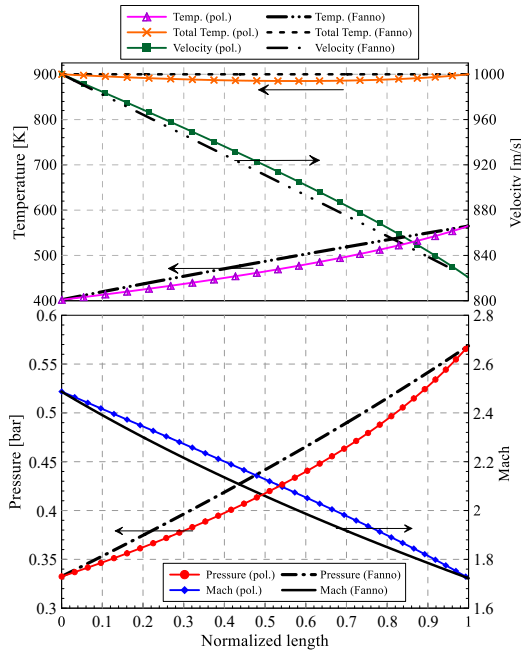


Figure 5.3: The comparison between the polytropic and the classic flows ($p_0 = 5.57$ bar, $T_0 = 900$ K, $u_{in} = 1000$ m/s, $L_{max,Fanno} = 35$ m)

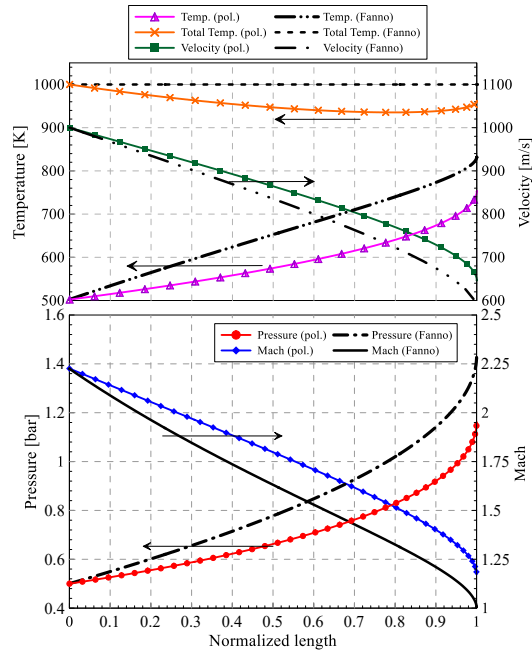


Figure 5.4: The comparison between the polytropic and the classic flows ($p_0 = 5.57$ bar, $T_0 = 1000$ K, $u_{in} = 1000$ m/s, $L_{max,Fanno} = 60.15$ m)

difference in p (the continuous curve with dot symbols and the dashed-dotted curve with narrow space in Fig. 5.4) even arrives at 19.5%, and the other maximum errors are all above 5%. Under the circumstances in terms of Figs. 5.2-5.4, the polytropic flow model is not capable to well simulate the Fanno flow.

5.3 Numerical model

In order to model Fanno flows through the polytropic method with a higher accuracy and without modifying the length of the duct, a numerical model in which the polytropic exponent can be varied piece by piece have been developed.

In this model, the fluid dynamics along the investigated duct is governed by the generalized Euler partial differential equations of mass conservation and momentum balance. The third equation, originally the energy equation, has been replaced by a material derivative of $p\rho^{-m}$ along the pipe since the

polytropic process should be retained. The governing equations write

$$\left\{ \begin{array}{l} \frac{\partial}{\partial t} \begin{bmatrix} \rho \\ \rho u \end{bmatrix} + \frac{\partial}{\partial x} \begin{bmatrix} \rho u \\ \rho u^2 + p \end{bmatrix} = \begin{bmatrix} 0 \\ -4\tau_w/D \end{bmatrix} \\ \frac{\partial p \rho^{-m}}{\partial t} + u \frac{\partial p \rho^{-m}}{\partial x} = 0 \end{array} \right. \quad (5.16)$$

where t is the time and x is the space coordinate along the duct axis, and m is calculated by applying the expression in Eq. (5.15) to the fluid states of two neighbor points along the duct obtained from classic Fanno flow relations. Therefore, along the duct, the value of m varies piece by piece. Furthermore, the well-known perfect gas equation is as well employed to compute the state properties.

Since it is confirmed that all solutions, which are the flow properties, are smooth in the tested flows, treating ρ , u and p as three independent variables, Eq. (5.16) can be manipulated into the non-conservative formulations [101]:

$$\frac{\partial}{\partial t} \begin{bmatrix} \rho \\ u \\ p \end{bmatrix} + \begin{bmatrix} u & \rho & 0 \\ 0 & u & 1/\rho \\ 0 & mp & u \end{bmatrix} \frac{\partial}{\partial x} \begin{bmatrix} \rho \\ u \\ p \end{bmatrix} = \begin{bmatrix} 0 \\ -4\tau_w/D \\ 0 \end{bmatrix} \quad (5.17)$$

The Jacobian matrix of Eq. (5.17) is further rearranged into the form of Eq. (2.9), and the set of equations is reported as

$$\frac{\partial \mathbf{w}}{\partial t} + [\mathbf{C}] \frac{\partial \mathbf{w}}{\partial x} = \mathbf{H} \quad (5.18)$$

where $[\mathbf{C}]$ is the diagonalized Jacobian matrix of the system as a function of u , m , γ and $c_s = \sqrt{\gamma RT}$ (c_s is the isentropic sound speed), where R is the elasticity constant of the perfect gas:

$$[\mathbf{C}] = \begin{bmatrix} u - \sqrt{\frac{m}{\gamma}} c_s & 0 & 0 \\ 0 & u & 0 \\ 0 & 0 & u + \sqrt{\frac{m}{\gamma}} c_s \end{bmatrix} \quad (5.19)$$

Quantity \mathbf{w} is the vector of the characteristic variables

$$\delta \mathbf{w} = \begin{bmatrix} \delta w_1 \\ \delta w_2 \\ \delta w_3 \end{bmatrix} = \begin{bmatrix} -\frac{\rho}{2\sqrt{(m/\gamma)c_s}}\delta u + \frac{1}{(2m/\gamma)c_s^2}\delta p \\ \delta \rho - \frac{1}{(m/\gamma)c_s^2}\delta p \\ \frac{\rho}{2\sqrt{(m/\gamma)c_s}}\delta u + \frac{1}{(2m/\gamma)c_s^2}\delta p \end{bmatrix} \quad (5.20)$$

and \mathbf{H} is the vector of the source terms

$$\mathbf{H} = \begin{bmatrix} H_1 \\ H_2 \\ H_3 \end{bmatrix} = \begin{bmatrix} \frac{\rho}{2\sqrt{(m/\gamma)c_s}} \cdot \frac{4\tau_w}{D} \\ 0 \\ -\frac{\rho}{2\sqrt{(m/\gamma)c_s}} \cdot \frac{4\tau_w}{D} \end{bmatrix} \quad (5.21)$$

It is noteworthy that the eigenvalues in the diagonalized Jacobian matrix is no longer $u - c_s$, u and $u + c_s$ as present in the classic one-dimensional Euler equations [101], which considers mass conservation, momentum balance and energy conservation equations. Therefore, the polytropic method possesses different wave propagation speeds.

A finite-difference upwind numerical scheme has been employed to discretize Eqs. (5.18)-(5.21). It is an explicit, non-conservative one-step method of the first-order accuracy, which is as well referred to the explicit Euler scheme. Since the flow velocity is in line with the positive direction of the space coordinates in all simulations, $u > 0$ and $u + (m/\gamma)c_s > 0$ always hold. The numerical scheme between time instants t_n and t_{n+1} writes

$$\left\{ \begin{array}{l} w_{1,i}^{n+1} = \begin{cases} w_{1,i}^n - \frac{\Delta t}{\Delta x} (u_i^n - \sqrt{\frac{m}{\gamma}} c_{s,i}^n) \cdot (w_{1,i+1}^n - w_{1,i}^n) + \Delta t \cdot H_{1,i}^n \\ \quad \text{(if } u_i^n - \sqrt{m/\gamma} \cdot c_{s,i}^n < 0) \\ w_{1,i}^n - \frac{\Delta t}{\Delta x} (u_i^n - \sqrt{\frac{m}{\gamma}} c_{s,i}^n) \cdot (w_{1,i}^n - w_{1,i-1}^n) + \Delta t \cdot H_{1,i}^n \\ \quad \text{(if } u_i^n - \sqrt{m/\gamma} \cdot c_{s,i}^n \geq 0) \end{cases} \\ w_{2,i}^{n+1} = w_{2,i}^n - \frac{\Delta t}{\Delta x} u_i^n \cdot (w_{2,i}^n - w_{2,i-1}^n) + \Delta t \cdot H_{2,i}^n \\ w_{3,i}^{n+1} = w_{3,i}^n - \frac{\Delta t}{\Delta x} \left(u_i^n + \sqrt{\frac{m}{\gamma}} c_{s,i}^n \right) \cdot (w_{3,i}^n - w_{3,i-1}^n) + \Delta t \cdot H_{3,i}^n \end{array} \right. \quad (5.22)$$

According to Von Neumann stability analysis, the scheme is stable if the Courant-Friedrichs-Lewy condition is fulfilled. The time step length is varied at each instant, and the maximum Courant number is fixed at 0.9. Since the steady state properties are the investigated objects, once the change in all state values over a time step is considered minor, the simulation is terminated. The boundary conditions are assigned on the basis of the number of the characteristics entering each boundary, according to the theory of hyperbolic partial differential equations [101].

The sensitivity analyses of the numerical tests below have been conducted. As the nodes number of a model increases, all fluid properties remain basically unchanged.

5.4 Numerical model results

The same tested cases reported in Figs. 5.1-5.4 have been again investigated by means of the numerical model, and the comparison between the results of the numerical model and of the classic Fanno flow are reported in Figs. 5.5-5.6.

Fig. 5.5 demonstrates the new comparisons when the flows are under subsonic conditions (same tested points as the results exhibited in Figs. 5.1-5.2). In both cases shown in Figs. 5.5a and 5.5b, 201 nodes have been applied to the numerical model. Generally, no matter if the flow is choked or not, all selected fluid properties follow their original results of the Fanno flow. Meanwhile, the accuracy of the polytropic model's interpretation is of great satisfactory: the maximum error of the properties in the model takes place in the p curve (the continuous line with dot symbols) of Fig. 5.5b, and the value is only 0.57%.

The corresponding polytropic exponents of Fig. 5.5 refers to the lower diagram in Fig. 5.7. From the inlet to the outlet of the pipe, they both follow increasing trends, and all values are in the reasonable range, which is between 1 and 1.4 (the value of γ). Moreover, the value of m pertaining to the Point 2 (the continuous curve with cross symbols) at the duct exit approximates 1.4. Under this situation, $\sqrt{m/\gamma}$ approaches 1. The Mach number at the pipe outlet when the polytropic flow is choked turns to be c_s , which is in line with the right endpoint of Ma (the continuous curve with rhombus symbols) displayed in Fig. 5.5b.

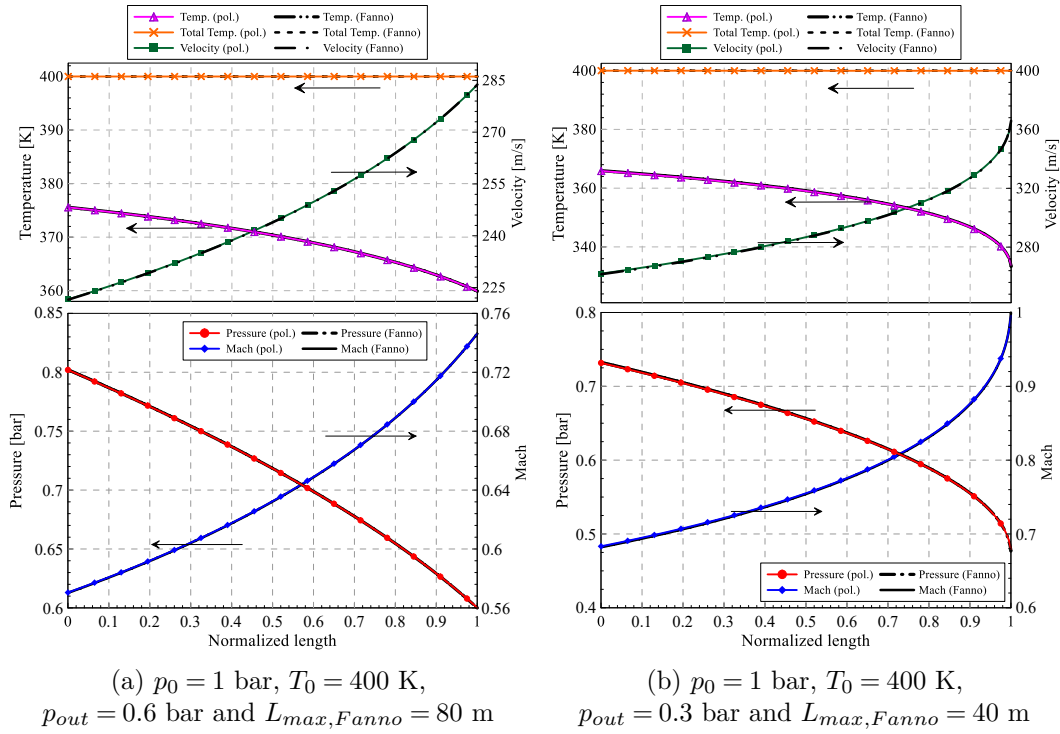


Figure 5.5: The comparison between the numerical results and the Fanno flows under subsonic conditions.

Fig. 5.6 reports the comparison as the flows are under supersonic conditions, and the tested points chosen are the same as those in Figs. 5.3-5.4. The nodes numbers selected are 234 and 402 respectively for Figs. 5.6a and 5.6b. Similar to the comparison shown in Fig. 5.5, all selected flow properties along the duct converge to the corresponding Fanno flow results. Among the properties, the maximum error percentage, which is 0.65%, occurs in p (the continuous curve with dot symbols) of Fig. 5.6b. As are demonstrated in the upper diagram in Fig. 5.7, both the m curves follow reduction trends. Meanwhile, m of Point 4 approaches 1.4 at the right boundary, corresponding to a Mach number (the continuous curve with rhombus symbols) of 1 at the duct exit reported in Fig. 5.6b. This refers to a Mach number threshold, below which a shock can be formed and a sharp transition between the supersonic and the subsonic flow can be present. Whereas, this cannot be simulated through the selected non-conservative numerical model.

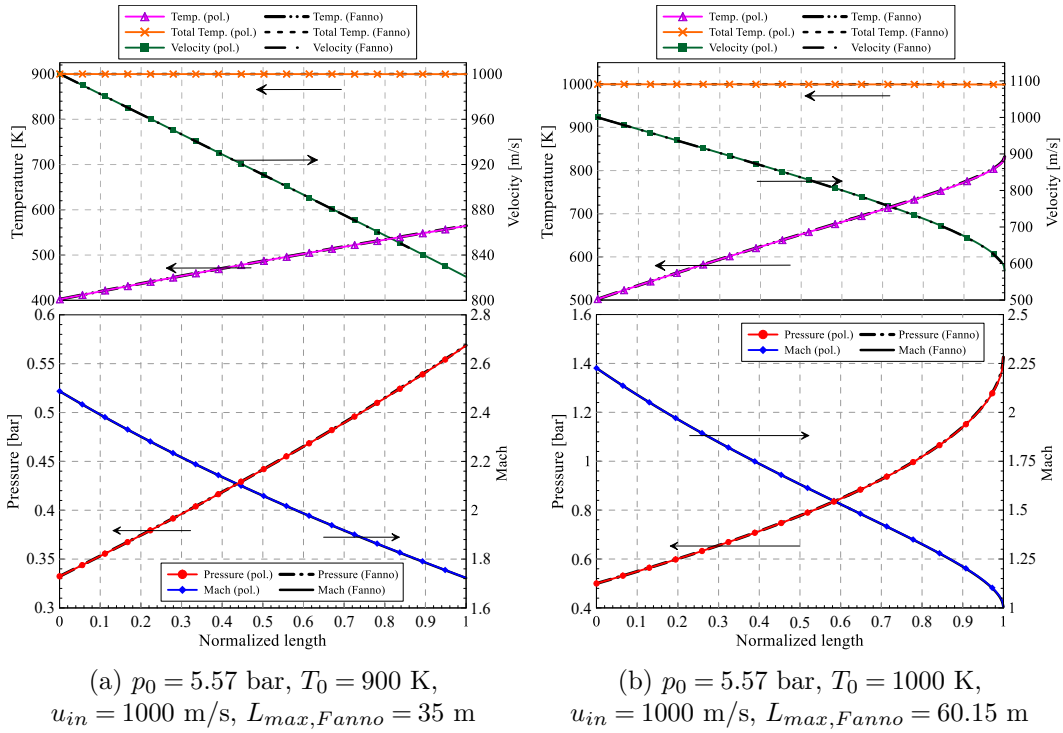


Figure 5.6: The comparison between the numerical results and the Fanno flows under subsonic conditions.

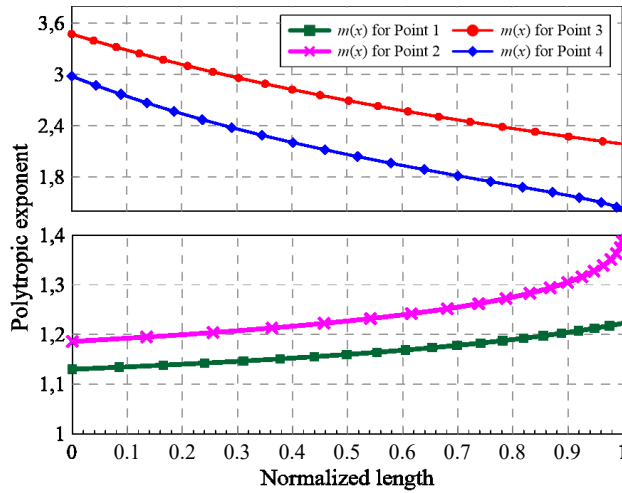


Figure 5.7: The polytropic exponent along the pipe
 (Point 1: $p_0 = 1 \text{ bar}$, $T_0 = 400 \text{ K}$, $p_{out} = 0.6 \text{ bar}$, $L_{max,Fanno} = 80 \text{ m}$;
 Point 2: $p_0 = 1 \text{ bar}$, $T_0 = 400 \text{ K}$, $p_{out} = 0.3 \text{ bar}$, $L_{max,Fanno} = 40 \text{ m}$;
 Point 3: $p_0 = 5.57 \text{ bar}$, $T_0 = 900 \text{ K}$, $u_{in} = 1000 \text{ m/s}$, $L_{max,Fanno} = 35 \text{ m}$;
 Point 4: $p_0 = 5.57 \text{ bar}$, $T_0 = 1000 \text{ K}$, $u_{in} = 1000 \text{ m/s}$, $L_{max,Fanno} = 60.15 \text{ m}$).

Chapter 6

Conclusions

The present work deals with the experimental and the numerical analysis of diesel common rail injection systems as well as the linked flowmeters. Starting from the current industrial instruments, no matter it is a flowmeter or an injection system, improvements in the structure still could be carried out. Furthermore, innovative control strategies, through which the injected mass can be estimated and controlled, have been proposed and experimentally examined. Finally, the viscous adiabatic flow has been interpreted by means of polytropic flows through both analytical and numerical procedures.

In Chap. 2, the injected flow-rates pertaining to one common rail injector has been evaluated by means of both Bosch method and Zeuch method-based flowmeters. Based on the comparison results of the outputs of those two flowmeters, a moving average effect and a shift of the information have been observed in the measured flow-rates of the device that applies Bosch method. A homemade numerical model of the EVI, which exploits Bosch method, has been then developed, in order to examine the causes of those phenomena.

In the Bosch method-based flowmeter, the chamber-like structures are parts of the reasons of the moving average phenomenon and can distort the high-frequency content appearing in the injection rate. Moreover, the damper acts as a restrictor, damping the pressure oscillations, and this is as well one cause of the moving average phenomenon in the injection rate. In addition, it is inferred that the convergent pipe slightly alters the pressure wave, and the thus evaluated flow-rate can be distorted.

Design keys to improve the Bosch method-based flowmeters have been provided. A reduction in all the hydraulic capacitances and the removal of all

the flow restrictions are suggested. Meanwhile, the convergent pipe should be avoided in order to remain the original shape of the effective injection rate.

In Chap. 3, an innovative Common-Feeding prototypal system has been realized for a light-duty commercial vehicle. The reference CR system, the reduced rail volume CR systems and the new CF system then have been experimentally examined. Furthermore, experimental campaign on a state-of-the-art common rail solenoid injector has been performed at the hydraulic rig. Parametrical analyses on the injector setup have been carried out by means of a numerical code, in order to exploit its potential for rate-shaping strategies. Pilot-main injection performance and the measured key dimensions of CRI 2.18 injector and of CRI 2.20 injector have been tested and compared.

With respect to the single injections, as the reduced accumulator is installed, only if the injected mass is sufficiently great, a significant pressure reduction within the high-pressure circuit during the effective injection event occurs. Meanwhile, the fuel pressure in the high-pressure circuit before the injection becomes greater. Such a phenomenon compensates the pressure drop during the injection cycle. Furthermore, the modification of the accumulator shape induces a variation in the free pressure wave frequency within the high-pressure circuit after the effective injection event. Whereas, this wave is not affected by the accumulator volume size. The static leakage of the CR system varies only at high nominal pressure values with the modified size of the accumulator, due to thermal reasons. The cycle-to-cycle dispersion in the injected mass rises as the CR accumulator size reduces. As regards the pilot-main injections, when the gauged orifices are mounted at the outlet of the accumulator, the fluctuation amplitude of the main injected mass versus DT curve declines.

Practical criteria have been proposed for determining the injection fusion threshold in Zeuch method-based flowmeters. In the injection regimes with small DT , the injected mass cycle-to-cycle dispersion is connected to the local slope of the $M_{cum} - DT$ curve. The greater the modulus of the slope, the larger the dispersion is. Furthermore, modifications in the mechanical and electromagnetic parameters of the solenoid injector are capable to vary the injection fusion threshold as well as the range of the interval, in which the injected mass is approximately not affected by DT . The parameters, such as I_{max} , L_{gap} , d_A , d_Z , d_{cp} and d_{ne} , are vital to influence the possibility to realize

rate-shaping strategies. Whereas, the hydraulic variables, which is linked to the flow areas along the injector inlet to nozzles holes, provide ignorable influence.

The CRI 2.20 injector possesses a smaller DT_{cr} value and a more reduced range of $DT_{max} < DT < DT_{cr}$ than those of the CRI 2.18 injector, and those performance prove that the former injector features a better capability in the closely-coupled pilot-main injection regimes. This superior performance can not be ascribed to the presence of the Minirail in the CRI 2.20 injector, but generally to the increase of hole Z diameter.

In Chap. 4, it has been examined that the thermal regime influences the injected quantity by varying the injection temporal length. Furthermore, by measuring the fuel pressure time distributions along the rail-to-injector pipe, the instantaneous mass flow-rate along that tube has been calculated in terms of single injections and pilot-main injections. Two techniques have been proposed.

One method is realized by applying a time frequency analysis technique to the pressure signals, in order to detect the effective injection temporal length of one injection. The correlation between the injected mass and the injection temporal length then translates the information into the injected fuel quantity. The accuracy of this estimation, independent of the thermal regime, is within 2 mg for all single injection working conditions.

The other approach employs physical equations. The computing strategy depends on the injection patterns: if a small single injection is applied, only one pressure transducer is essential; while in other cases of injections, two pressure signals are necessary. The passed fuel mass is obtained by integrating the in-pipe flow-rate over the injection event. A linear correlation of $M_{inj} = f(M_{inj,in})$, independent of the nominal pressure, the thermal regime and the engine speed, is then employed to estimate the injected mass. Finally, a PID controller is applied to correct the error by varying the energizing time of the single injection or of the main injection in the double injections.

This innovative Polito technique is capable to be applied without modification of the injector internal structure. The injection systems equipped with state-of-the-art injectors, have been applied to test the performance of single injections and of pilot-main injections with the new control strategy. The experimental results of steady-state single injection tests have shown that the accuracy of the injected mass, when the Polito closed-loop control strategy is applied, is lowered to approximately 1 mg for the entire working range under

different thermal regimes. Whereas, it is greater than 2 mg for the standard open-loop control strategy is employed. Evident enhancements have as well been found in the dynamic response to steps and ramps in $M_{inj,ref}$ and in p_{nom} . As far as the pilot-main injections are concerned, the M_{inj} accuracy with the Polito strategy can reach the values below 2 mg over the entire operating range. Significant enhancements in the stability of the rate-shaping regimes in $M_{inj} - DT$ curves have been observed.

In Chap. 5, the analytical expressions of a compressible flow in constant-area ducts with friction following a polytropic process have been developed. In the computation, the energy equation has been removed while a polytropic exponent, as a new variable, needs to be determined.

The comparisons between the flow properties calculated by means of the polytropic method and the classic Fanno method have been carried out. In those tests, the fluid properties at the duct inlet are analogous between the two methods, and the fluid states in the polytropic flow can generally follow the trends of the properties in Fanno flow. However, if the flow is choked, the properties at the outlets between the two methods are different, since the Mach numbers at the location, where the flows are choked, are varied. On the other hand, it is observed that the polytropic flow is no longer adiabatic.

In order to further converge the polytropic flow with friction to Fanno flow, a numerical model, based on the decoupling method, has been developed. As far as the results of the numerical model is concerned, the polytropic flow properties along the duct are generally identical to the results found through the classical analysis regardless of the different wave propagation speeds from the classic model. Particularly, with respect to the subsonic flow under choking condition, the fluid properties in the polytropic flow at the duct outlet is as well analogous to the results of Fanno flow, since the polytropic exponent approaches the isentropic exponent at that location.

References

- [1] S. Salam, T. Choudhary, A. Pugazhendhi, T. H. Verma, and A. Shanrma. A review on recent progress in computational and empirical studies of compression ignition internal combustion engine. *Fuel*, 279:118469, 2020.
- [2] J. Liu, P. Sun, H. Huang, J. Meng, and X. Yao. Experimental investigation on performance, combustion and emission characteristics of a common-rail diesel engine fueled with polyoxymethylene dimethyl ethers-diesel blends. *Applied Energy*, 202:527–536, 2017.
- [3] S. Negro, S. Falfari, and G. M. Bianchi. Coefficients for the calculation of thermophysical properties of indolene/ethanol biofuels for transcritical engine simulations. *Combustion and Flame*, 173:325–346, 2016.
- [4] D. Zhou, W. Yang, J. Li, K. L. Tay, S. K. Chou, and M. Kraft. Efficient combustion modelling in rcci engine with detailed chemistry. *Energy Procedia*, 105:1582–1587, 2017. 8th International Conference on Applied Energy, ICAE2016, 8-11 October 2016, Beijing, China.
- [5] R. Verschaeren and S. Verhelst. Increasing exhaust temperature to enable after-treatment operation on a two-stage turbo-charged medium speed marine diesel engine. *Energy*, 147:681–687, 2018.
- [6] D. Le, B. W. Pietrzak, and G. M. Shaver. Stability analysis of a dynamics surface control for piezoelectric fuel injection during rate shaping. In *Proceedings of the ASME 2014 Dynamic Systems and Control Conference*, San Antonio, TX, USA, October 22-24 2014.
- [7] W. Du, J. Lou, Y. Yan, W. Bao, and F. Liu. Effects of injection pressure on diesel sprays in constant injection mass condition. *Applied Thermal Engineering*, 121:234–241, 2017.
- [8] S. d’Ambrosio and A. Ferrari. Potential of multiple injection strategies implementing the after shot and optimized with the design of experiments procedure to improve diesel engine emissions and performance. *Applied Energy*, 155:933–946, 2015.
- [9] Z. Sun, G. Li, C. Chen, Y. Yu, and G. Gao. Numerical investigation on effects of nozzle’s geometric parameters on the flow and the cavitation characteristics within injector’s nozzle for a high-pressure common-rail DI diesel engine. *Energy Conversion and Management*, 89:843–861, 2015.

-
- [10] A. H. Gandhi, M. Meinhart, and S. Ortiz. Summary of flowmetering options for injector characterization. Technical Report 2009-01-0664, SAE Technical Paper, 2009.
- [11] S. Busch and P. C. Miles. Parametric study of injection rates with solenoid injectors in an injection quantity and rate measuring device. *ASME J. Eng. Gas Turbines Power*, 137:101503, 2015.
- [12] S. Ishikawa, Y. Ohmori, S. Fukushima, T. Suzuki, A. Takamura, and T. Kamimoto. Measurement of rate of multiple-injection in CDI diesel engines. Technical Report 2000-01-1257, SAE Technical Paper, 2000.
- [13] C. Arcoumanis and M. S. Baniasad. Analysis of consecutive fuel injection rate signals obtained by the zeuch and bosch methods. Technical Report 930921, SAE Technical Paper, 1993.
- [14] L. Postrioti, G. Buitoni, F. C. Pesce, and C. Ciaravino. Zeuch method-based injection rate analysis of a common-rail system operated with advanced injection strategies. *Fuel*, 128:188–198, 2014.
- [15] T. Yamaguchi, K. Watabe, M. Sano T. Kamako, and S. Ishikawa. Development of highly precise injection-rate detector applicable to piezoelectric injectors having the function of ultra multi-stage injection. Technical Report 2015-01-2001, SAE Technical Paper, 2015.
- [16] W. Bosch. The fuel rate indicator: a new measuring instrument for display of the characteristics of individual injection. Technical Report 660749, SAE Technical Paper, 1966.
- [17] G. B. Bower and D. E. Foster. A comparison of the Bosch and Zuech rate of injection meters. Technical Report 910724, SAE Technical Paper, 1991.
- [18] A. Takamura, T. Ohta, and S. Fukushima. A study on precise measurement of diesel fuel injection rate. Technical Report 920630, SAE Technical Paper, 1992.
- [19] R. Payri, F. J. Salvador, J. Gimeno, and G. Bracho. A new methodology for correcting the signal cumulative phenomenon on injection rate measurements. *Exp. Tech.*, 32(1):46–49, 2008.
- [20] A. E. Catania, A. Ferrari, and A. Mittica. High-pressure rotary pump performance in multi-jet common rail systems. In *Proceedings of 8th Biennial ASME Conference on Engineering Systems Design and Analysis. Volume 4: Fatigue and Fracture, Heat Transfer, Internal Combustion Engines, Manufacturing, and Technology and Society*, 2006.
- [21] W. Naoki, W. Naoki, S. Scott, C. Emre, Y. Koji, and P. Lyle. Ignition and soot formation/oxidation characteristics of compositionally unique international diesel blends. Technical Report 2019-01-0548, SAE Technical Paper, 2019.

- [22] L. Duan, S. Yuan, L. Hu, W. Yang, J. Yu, and X. Xia. Injection performance and cavitation analysis of an advanced 250 MPa common rail diesel injector. *International Journal of Heat and Mass Transfer*, 93:388–397, 2016.
- [23] J. A. Soriano, C. Mata, O. Armas, and C. Ávila. A zero-dimensional model to simulate injection rate from first generation common rail diesel injectors under thermodynamic diagnosis. *Energy*, 158:845–858, 2018.
- [24] K. Vakiti, J. Deussen, C. Pilger, H. K. Nanjundaswamy, T. Szailer, M. Franke, D. Tomazic, K. Thomas, M. Romijn, K. Deppenkemper, and G. Vagnoni. In-use compliance opportunity for diesel powertrains. Technical Report 2018-01-0877, SAE Technical Paper, 2018.
- [25] A. Ferrari, A. Mittica, P. Pizzo, X. Wu, and H. Zhou. New methodology for the identification of the leakage paths and guidelines for the design of common rail injectors with reduced leakage. *ASME J. Eng. Gas Turbines Power*, 140(2):022801, 2018.
- [26] J. Hammer, D. Naber, M. Raff, and D. Zeh. Bosch diesel fuel injection system – with modularity from entry up to high-end segment. In *9. Tagung Diesel- und Benzindirekteinspritzung 2014, Proceedings*, pages 1–15, Wiesbaden, 2015. Springer Vieweg.
- [27] K. Serizawa, D. Ueda, N. Mikami, Y. Tomida, and J. Weber. Realizing robust combustion with high response diesel injector with controlled diffusive spray nozzle and closed loop injection control. Technical Report 2017-01-0845, SAE Technical Paper, 2017.
- [28] K. Zhang, Z. Xie, and M. Zhou. Model-based optimization and pressure fluctuation control of pressure reservoir in electrically controlled fuel injection system for single cylinder diesel engine. In *Proceedings of the ASME 2017 Internal Combustion Engine Division Fall Technical Conference*, Seattle, Washington, USA, October 15-18 2017.
- [29] A. E. Catania and A. Ferrari. Development and performance assessment of the new-generation CF fuel injection system for diesel passenger cars. *Applied Energy*, 91:483–495, 2012.
- [30] A. E. Catania, A. Ferrari, A. Mittica, and E. Spessa. Common rail without accumulator: Development, theoretical-experimental analysis and performance enhancement at DI-HCCI level of a new generation FIS. Technical Report 2007-01-1258, SAE Technical Paper, 2007.
- [31] S. d’Ambrosio and A. Ferrari. Potentialities of boot injection combined with after shot for the optimization of pollutant emissions, fuel consumption and combustion noise in passenger car diesel engines. *SAE International Journal of Engines*, 10(2):144–159, 2017.

-
- [32] F. Sapio, A. Piano, F. Millo, and F. C. Pesce. Digital shaping and optimization of fuel injection pattern for a common rail automotive diesel engine through numerical simulation. Technical Report 2017-24-0025, SAE Technical Paper, 2017.
- [33] D. Needham, D. Mellors, T. Williams, T. Cawkwell, and S. Tullis. Dynamic rate shaping—one diesel common-rail injector for all combustion strategies. In *Heavy-Duty-, On-und Off-Highway-Motoren 2018*, pages 335–357. Springer, 2019.
- [34] J. Hammer, M. Raff, and D. Naber. Advanced diesel fuel injection equipment—a never ending BOSCH story. In *14. Internationales Stuttgarter Symposium*, pages 31–45. Springer, 2014.
- [35] A. Ferrari and A. Mittica. Response of different injector typologies to dwell time variations and a hydraulic analysis of closely-coupled and continuous rate shaping injection schedules. *Applied Energy*, 169:899–911, 2016.
- [36] V. Macian, R. Payri, S. Ruiz, M. Bardi, and A. H. Plazas. Experimental study of the relationship between injection rate shape and diesel ignition using a novel piezo-actuated direct-acting injector. *Applied Energy*, 118:100–113, 2014.
- [37] S. d’Ambrosio and A. Ferrari. Effects of pilot injection parameters on low temperature combustion diesel engines equipped with solenoid injectors featuring conventional and rate-shaped main injection. *Energy Conversion and Management*, 110:457–468, 2016.
- [38] S. d’Ambrosio and A. Ferrari. Boot injection dynamics and parametrical analysis of boot shaped injections in low-temperature combustion diesel engines for the optimization of pollutant emissions and combustion noise. *Energy*, 134:420–437, 2017.
- [39] J. M. Desantes, J. Benajes, S. Molina, and C. A. González. The modification of the fuel injection rate in heavy-duty diesel engines. part 1: Effects on engine performance and emissions. *Applied Thermal Engineering*, 24(17):2701–2714, 2004.
- [40] J. O’Connor and M. Musculus. Post injections for soot reduction in diesel engines: a review of current understanding. *SAE International Journal of Engines*, 6(1):400–421, 2013.
- [41] A. Ferrari, A. Mittica, and E. Spessa. Benefits of hydraulic layout over driving system in piezo-injectors and proposal of a new-concept CR injector with an integrated minirail. *Applied Energy*, 103:243–255, 2013.
- [42] A. Piano, G. Boccardo, F. Millo, A. Cavicchi, L. Postrioti, and F. C. Pesce. Experimental and numerical assessment of multi-event injection

- strategies in a solenoid common-rail injector. *SAE International Journal of Engines*, 10(4):2129–2140, 2017.
- [43] R. Payri, J. De la Morena, V. Pagano, A. Hussain, G. Sammut, and L. Smith. One-dimensional modeling of the interaction between close-coupled injection events for a ballistic solenoid injector. *International Journal of Engine Research*, 20(4):452–469, 2019.
- [44] S. d’Ambrosio and A. Ferrari. Diesel injector coking: optical-chemical analysis of deposits and influence on injected flow-rate, fuel spray and engine performance. *ASME J. Eng. Gas Turbines Power*, 134(6):062801, 2012.
- [45] M. Abdullah, A. Shinobu, K. Tomoki, and T. Aizawa. Effects of inversed-delta injection rate shaping on diesel spray flame liquid length, lift-off length and soot onset. *Fuel*, 258:116–170, 2019.
- [46] D. Zhou, K. L. Tay, Y. Tu, J. Li, W. Yang, and D. Zhao. A numerical investigation on the injection timing of boot injection rate-shapes in a kerosene-diesel engine with a clustered dynamic adaptive chemistry method. *Applied Energy*, 220:117–126, 2018.
- [47] S. d’Ambrosio, R. Finesso, L. Fu, A. Mittica, and E. Spessa. A control-oriented real-time semi-empirical model for the prediction of NOx emissions in diesel engines. *Applied Energy*, 130:265–279, 2014.
- [48] M. Jia, M. Xie, T. Wang, and Z. Peng. The effect of injection timing and intake valve close timing on performance and emissions of diesel PCCI engine with a full engine cycle CFD simulation. *Applied Energy*, 88(9):2967–2975, 2011.
- [49] G. Xu, M. Jia, Y. Li, M. Xie, and W. Su. Multi-objective optimization of the combustion of a heavy-duty diesel engine with low temperature combustion under a wide load range: (i) computational method and optimization results. *Energy*, 126:707–719, 2017.
- [50] A. Jain, A. P. Singh, and A. K. Agarwal. Effect of split fuel injection and EGR on NOx and PM emission reduction in a low temperature combustion (LTC) mode diesel engine. *Energy*, 122:249–264, 2017.
- [51] K. Anand and R. D. Reitz. Exploring the benefits of multiple injections in low temperature combustion using a diesel surrogate model. *Fuel*, 165:341–350, 2016.
- [52] A. K. Agarwal, A. P. Singh, and R. K. Maurya. Evolution, challenges and path forward for low temperature combustion engines. *Progress in Energy and Combustion Science*, 61:1–56, 2017.
- [53] C. Guardiola, B. Pla, P. Bares, and A. Stefanopoulou. Cylinder charge composition observation based on in-cylinder pressure measurement. *Measurement*, 131:559–568, 2019.

- [54] X. Shen, Y. Zhang, and T. Shen. Cylinder pressure resonant frequency cyclic estimation-based knock intensity metric in combustion engines. *Applied Thermal Engineering*, 158:113756, 2019.
- [55] C. Fang, M. Ouyang, and F. Yang. Real-time start of combustion detection based on cylinder pressure signals for compression ignition engines. *Applied Thermal Engineering*, 114:264–270, 2017.
- [56] T. Gao, S. Yu, K. Xie, M. Jeftic, M. Wang, and M. Zheng. The estimation of nitrogen oxides reduction potential through enhanced heat release analysis. In *ASME 2016 Internal Combustion Engine Division Fall Technical Conference*. American Society of Mechanical Engineers Digital Collection, 2016.
- [57] P. Bares, D. Selmanaj, C. Guardiola, and C. Onder. A new knock event definition for knock detection and control optimization. *Applied Thermal Engineering*, 131:80–88, 2018.
- [58] J. Ängeby, A. Johnsson, and K. Hellström. Knock detection using multiple indicators and a classification approach. *IFAC-PapersOnLine*, 51(31):297–302, 2018.
- [59] Z. Yang, X. Han, S. Yu, X. Yu, M. Wang, M. Zheng, and D. Ting. A fuel sensitive ignition delay model for direct injection diesel engine operating under EGR diluted conditions. Technical Report 2018-01-0231, SAE Technical Paper, 2018.
- [60] R. Finesso, O. Mareello, D. Misul, E. Spessa, M. Violante, Y. Yang, G. Hardy, and C. Maier. Development and assessment of pressure-based and model-based techniques for the MFB50 control of a Euro VI 3.0 L diesel engine. *SAE International Journal of Engines*, 10(4):1538–1555, 2017.
- [61] Y. Yang, Z. Peng, W. Zhang, and G. Meng. Parameterised time-frequency analysis methods and their engineering applications: A review of recent advances. *Mechanical Systems and Signal Processing*, 119:182–221, 2019.
- [62] Z. Feng, M. Liang, and F. Chu. Recent advances in time–frequency analysis methods for machinery fault diagnosis: A review with application examples. *Mechanical Systems and Signal Processing*, 38(1):165–205, 2013.
- [63] Z. Feng, W. Zhu, and D. Zhang. Time-frequency demodulation analysis via vold-kalman filter for wind turbine planetary gearbox fault diagnosis under nonstationary speeds. *Mechanical Systems and Signal Processing*, 128:93–109, 2019.
- [64] A. Taghizadeh-Alisaraei, B. Ghobadian, T. Tavakoli-Hashjin, S. S. Mohtasebi, A. Rezaei-asl, and M. Azadbakht. Characterization of engine’s

- combustion-vibration using diesel and biodiesel fuel blends by time-frequency methods: A case study. *Renewable Energy*, 95:422–432, 2016.
- [65] A. Taghizadeh-Alisaraei and A. Mahdavian. Fault detection of injectors in diesel engines using vibration time-frequency analysis. *Applied Acoustics*, 143:48–58, 2019.
- [66] S. Ji, X. Lan, J. Lian, H. Wang, M. Li, Y. Cheng, and W. Yin. Combustion parameter estimation for ICE from surface vibration using frequency spectrum analysis. *Measurement*, 128:485–494, 2018.
- [67] J. M. Luján, C. Guardiola, B. Pla, and P. Bares. Estimation of trapped mass by in-cylinder pressure resonance in HCCI engines. *Mechanical Systems and Signal Processing*, 66:862–874, 2016.
- [68] C. Guardiola, B. Pla, P. Bares, and A. Barbier. An analysis of the in-cylinder pressure resonance excitation in internal combustion engines. *Applied Energy*, 228:1272–1279, 2018.
- [69] V. Dekys, P. Kalman, P. Hanak, P. Novak, and Z. Stankovicova. Determination of vibration sources by using STFT. *Procedia Engineering*, 177:496–501, 2017.
- [70] A. Ferrari and F. Paolicelli. A virtual injection sensor by means of time frequency analysis. *Mechanical Systems and Signal Processing*, 116:832–842, 2019.
- [71] J. V. Pastor, J. M. García-Oliver, A. García, and M. Pinotti. Effect of laser induced plasma ignition timing and location on diesel spray combustion. *Energy Conversion and Management*, 133:41–55, 2017.
- [72] L. Wang, G. Li, C. Xu, X. Xi, X. Wu, and S. Sun. Effect of characteristic parameters on the magnetic properties of solenoid valve for high-pressure common rail diesel engine. *Energy Conversion and Management*, 127:656–666, 2016.
- [73] F. J. Salvador, P. Marti-Aldaravi, M. Carreres, and D. Jaramillo. An investigation on the dynamic behaviour at different temperatures of a solenoid operated common-rail ballistic injector by means of a one-dimensional model. Technical Report 2014-01-1089, SAE Technical Paper, 2014.
- [74] R. Finesso, E. Spessa, and Y. Yang. Fast estimation of combustion metrics in DI diesel engines for control-oriented applications. *Energy Conversion and Management*, 112:254–273, 2016.
- [75] C. A. MacCarley, W. D. Clark, and K. T. Nakae. An indirect sensing technique for closed-loop diesel fuel quantity control. *SAE transactions*, pages 188–196, 1990.

- [76] F. Yan and J. Wang. Common rail injection system iterative learning control based parameter calibration for accurate fuel injection quantity control. *International Journal of Automotive Technology*, 12(2):149–157, 2011.
- [77] U. Schmid, G. Krötz, and D. Schmitt-Landsiedel. A volumetric flow sensor for automotive injection systems. *Journal of Micromechanics and Microengineering*, 18(4):045006, 2008.
- [78] K. Ishiduka, K. Uchiyama, K. Higuchi, N. Yamada, K. Takeuchi, and O. E. Herrmann. Further innovations for diesel fuel injection systems: Close-loop control of fuel quantity by i-Art & ultra high injection pressure. In *19th Aachen colloquium*, Aachen, 2010.
- [79] T. Miyaura, A. Morikawa, Y. Ito, K. Ishizuka, and T. Tsuiki. Development of diesel engine using new fuel injection system—direct monitoring of fuel injection pressure using injector with built-in sensor, and its applications. Technical Report 2013-01-1739, SAE Technical Paper, 2013.
- [80] P. Voigt, H. Schiffgens, C. Daveau, J. Ogé, J. Béduneau, G. Meissonier, C. Tapin, and X. Lalé. Delphi injector closed loop control strategy using the “Switch” technology for diesel passenger cars—injector hardware. In *10. Tagung Diesel-und Benzindirekteinspritzung 2016*, pages 41–66. Springer, 2017.
- [81] J. Anderson. *Modern Compressible Flow with Historical Perspective*, 3rd ed. McGraw-Hill, Boston, 2003.
- [82] E. Urata. A flow rate equation for subsonic Fanno flow. *Proceedings of the Institution of Mechanical Engineers, Part C: Journal of Mechanical Engineering Science*, 227(12):2724–2729, 2013.
- [83] D. C. Rennels and H. M. Hudson. *Pipe flow: A practical and comprehensive guide*. John Wiley & Sons, New York, 2012.
- [84] A. H. Shapiro. *The dynamics and thermodynamics of compressible fluid flow. Vol. 1*. John Wiley & Sons, New York, 1953.
- [85] W. M. Kirkland. A polytropic approximation of compressible flow in pipes with friction. *ASME J. Fluids Eng.*, 141(12), 2019.
- [86] E. E. Michaelides and S. Parikh. The prediction of critical mass flux by the use of Fanno lines. *Nuclear Engineering and Design*, 75(1):117–124, 1983.
- [87] M. Cavazzuti and M. A. Corticelli. Numerical modelling of fanno flows in micro channels: a quasi-static application to air vents for plastic moulding. *Thermal Science and Engineering Progress*, 2:43–56, 2017.

- [88] N. Agrawal and S. Bhattacharyya. Adiabatic capillary tube flow of carbon dioxide in a transcritical heat pump cycle. *International journal of Energy Research*, 31(11):1016–1030, 2007.
- [89] S. D. Deodhar, H. B. Kothadia, K. N. Iyer, and S. V. Prabhu. Experimental and numerical studies of choked flow through adiabatic and diabatic capillary tubes. *Applied Thermal Engineering*, 90:879–894, 2015.
- [90] N. S. Kumar and K. T. Ooi. One dimensional model of an ejector with special attention to fanno flow within the mixing chamber. *Applied Thermal Engineering*, 65(1-2):226–235, 2014.
- [91] D. Kawashima and Y. Asako. Data reduction of friction factor of compressible flow in micro-channels. *International Journal of Heat and Mass Transfer*, 77:257–261, 2014.
- [92] M. Cavazzuti, M. A. Corticelli, and T. G. Karayiannis. Compressible fanno flows in micro-channels: An enhanced quasi-2d numerical model for laminar flows. *Thermal Science and Engineering Progress*, 10:10–26, 2019.
- [93] M. Cavazzuti, M. A. Corticelli, and T. G. Karayiannis. Compressible fanno flows in micro-channels: An enhanced quasi-2d numerical model for turbulent flows. *International Communications in Heat and Mass Transfer*, 111:104448, 2020.
- [94] Crane Co. Engineering Division. *Flow of fluids through valves, fittings, and pipe*. Crane Company, 1957.
- [95] A. Ferrari and T. Zhang. Benchmark between Bosch and Zeuch method-based flowmeters for the measurement of the fuel injection rate. *International Journal of Engine Research*, in press, 2019.
- [96] A. Ferrari, Z. Jin, A. Mittica, O. Vento, and T. Zhang. Application of the Common-Feeding injection system layout to light duty commercial vehicle diesel engines. In *Proceedings of the ASME 2019 Internal Combustion Engine Division Fall Technical Conference*, Chicago, Illinois, USA, October 20-23 2019.
- [97] A. Ferrari and T. Zhang. Influence of the injector setup on digital and continuous injection rate-shaping performance in diesel engine passenger cars. *Energy Conversion and Management*, 205:112259, 2020.
- [98] A. Ferrari, C. Novara, E. Paolucci, O. Vento, M. Violante, and T. Zhang. Design and rapid prototyping of a closed-loop control strategy of the injected mass for the reduction of CO₂, combustion noise and pollutant emissions in diesel engines. *Applied Energy*, 232:358–367, 2018.

- [99] A. Ferrari, C. Novara, E. Paolucci, O. Vento, M. Violante, and T. Zhang. A new closed-loop control of the injected mass for a full exploitation of digital and continuous injection-rate shaping. *Energy Conversion and Management*, 177:629–639, 2018.
- [100] A. E. Catania, A. Ferrari, and E. Spessa. Temperature variations in the simulation of high-pressure injection-system transient flows under cavitation. *International Journal of Heat and Mass Transfer*, 51:2090–2107, 2008.
- [101] E. F. Toro. *Riemann solvers and numerical methods for fluid dynamics: a practical introduction, 3rd ed.* Springer Verlag, Heidelberg, 2009.
- [102] N. S. Cheng. Formulas for friction factor in transitional regions. *ASCE J. Hydraul. Eng.*, 134(9):1357–1362, 2008.
- [103] W. Zielke. Frequency-dependent friction in transient pipe flow. *ASME J. Basic Eng.*, 90(1):109–115, 1968.
- [104] T. Kagawa, I. Y. Lee, A. Kitagawa, and T. Taakenaka. High speed and accurate computing method of frequency-dependent friction in laminar pipe flow for characteristics methods. *Trans. Jpn. Soc. Mech. Eng. Ser. B*, 49(447):2638–2644, 1983.
- [105] A. Ferrari and F. Paolicelli. An indirect method for the real-time evaluation of the fuel mass injected in small injections in common rail diesel engine. *Fuel*, 191:322–329, 2017.
- [106] J. C. Tannehill, D. A. Anderson, and R. H. Pletcher. *Computational fluid mechanics and heat transfer.* Taylor & Francis, Philadelphia, 1997.
- [107] C. Hirsch. *Numerical computation of internal and external flows – vol. I.* Butterworth-Heinemann, Elsevier Press, Oxford, 2007.
- [108] A. Ferrari, A. Mittica, P. Pizzo, and Z. Jin. PID controller modelling and optimization in CR system with standard and reduced accumulators. *International Journal of Automotive Technology*, 19(5):771–781, 2018.
- [109] A. Ferrari, A. Mittica, F. Paolicelli, and P. Pizzo. Hydraulic characterization of solenoid-actuated injectors for diesel engine common rail system. *Energy Procedia*, 101:878–885, 2016.
- [110] M. Baratta, A. Catania, and A. Ferrari. Hydraulic circuit design rules to remove the dependence of the injected fuel amount on dwell time in multijet CR systems. *ASME J. Eng. Gas Turbines Power*, 130:121104, 2008.
- [111] A. Ferrari, F. Paolicelli, and P. Pizzo. The new-generation of solenoid injectors equipped with pressure-balanced pilot valves for energy saving and dynamic response improvement. *Applied Energy*, 151:367–376, 2015.

-
- [112] A. E. Catania, A. Ferrari, and M. Manno. Development and application of a complete multijet common-rail injection-system mathematical model for hydrodynamic analysis and diagnostics. *ASME J. Eng. Gas Turbines Power*, 130(6):062809, 2008.
- [113] F. J. Salvador, J. Gimeno, M. Carreres, and M. Crialesi-Esposito. Fuel temperature influence on the performance of a last generation common-rail diesel ballistic injector. part i: Experimental mass flow rate measurements and discussion. *Energy Conversion and Management*, 114:364–375, 2016.
- [114] A. Ferrari and P. Pizzo. Optimization of an algorithm for the measurement of unsteady flow-rates in high-pressure pipelines and application of a newly designed flowmeter to volumetric pump analysis. *ASME J. Eng. Gas Turbines Power*, 138(3):031604, 2016.
- [115] A. Ferrari. Injection system, apparatus and method for controlling the quantity of fuel injected. *Patent Application N. IB2017/050370*, 2017.
- [116] S. Busch, K. Zha, P. C. Miles, A. Warey, F. Pesce, R. Peterson, and A. Vassallo. Experimental and numerical investigations of close-coupled pilot injections to reduce combustion noise in a small-bore diesel engine. *SAE International Journal of Engines*, 8(2):660–678, 2015.
- [117] A. Ferrari. *Fondamenti di Termofluidodinamica per le Macchine, Vol. I*. CittàStudi, Biella, 2018.